Extraction of Fragmentation Functions from Charged Kaon and Pion Production at COMPASS

Dissertation

zur

Erlangung des Doktorgrades (Dr. rer. nat.)

der

Mathematisch-Naturwissenschaftlichen Fakultät

der

Rheinischen Friedrich-Wilhelms-Universität

Bonn

vorgelegt von

Regine Antje Panknin

aus

Suhl

Bonn, October 2012

Abstract

Quark helicity distributions can be accessed by measuring spin asymmetries in polarised deep-inelastic scattering, but for a full flavour separation the precise knowledge of quark fragmentation functions is essential. Those can only be inferred from experimental data, and are still poorly determined today. The few existing parametrisations of fragmentation functions are derived from world data (mainly on electron-positron annihilation), and often differ considerably, most notably for strange quarks.

This thesis presents an independent evaluation of fragmentation functions from deep-inelastic scattering data recorded at the COMPASS experiment. A method of extraction was developed, based on the relation between hadron multiplicities, $r^h(x, z)$, unpolarised parton distribution functions, $q(x)$, and quark fragmentation functions into hadrons, $D_d^h(z)$. (In this work x stands for the Bjorken scaling variable, and z for the fraction of the quark momentum that is transferred to the produced hadron.) Multiplicities for charged kaons and pions from 2004 data extracted by the COMPASS collaboration and two sets of unpolarised parton distribution functions from global parametrisations (CTEQ6 and MSTW) were used as input for a system of equations, and five different fragmentation functions (D_{fav}, D_{unf} for pions and D_{str}, D_{fav}, D_{unf} for kaons) were extracted in four z bins. To evaluate the stability of the results a number of tests was performed, among them limiting the x range of the multiplicities and unpolarised parton distribution functions used for the analysis, and comparing them to results derived with a set of artificial multiplicities generated with the particle physics event generator PYTHIA.

Four of the five extracted fragmentation functions - D_{fav} and D_{unf} for both pions and kaons - are quite stable with regard to the parton distribution used as well as to the x range in which the analysis was performed, and agree with an earlier evaluation by the EMC collaboration. The fifth fragmentation function, D_{str} for charged kaons, shows incompatible results for the different x intervals of the multiplicities used in the analysis, and also differs considerably for the two parametrisations of unpolarised parton distribution functions. The extracted values for D_{str} are often negative - and therefore physically impossible, and do not agree with predictions from parametrisations.

Zusammenfassung

Helizitätverteilungen von Quarks im Nukleon lassen sich durch die Messung von Spin-Asymmetrien in polarisierter tiefinelastischer Streuung erforschen, doch für eine komplette Flavourzerlegung ist die genaue Kenntnis von Quark-Fragmentationsfunktionen unerlässlich. Diese können nur aus experimentellen Daten erschlossen werden, und sind noch immer schlecht bestimmt. Die extistierenden Parametrisierungen von Fragmentationsfunktionen beruhen größtenteils auf Elektron-Positron-Annihilations-Daten, und unterscheiden sich zum Teil stark voneinander, insbesondere für Strange-Quarks.

In der vorliegenden Arbeit wird eine unabhängige Bestimmung von Fragmentationsfunktionen präsentiert, die auf Daten über tiefinelastische Streuung des COMPASS-Experiments beruht. Es wurde eine Extraktionsmethode entwickelt, die die Beziehung zwischen Hadronmultiplizitäten, $r^h(x,z)$, unpolarisierten Partondistributionsfunktionen, $q(x)$, und Fragmentationsfunktionen $D_q^h(z)$, ausnutzt. (Hierbei steht x für die Bjorken Skalenvariable, und z für den Impulsbruchteil, der vom Quark auf das produzierte Hadron übertragen wird.) Ein Gleichungssystem wurde entwickelt, in dem von der COMPASS-Kollaboration aus 2004er Daten extrahierte Multiplizitäten für geladene Kaonen und Pionen, sowie zwei Parametrisierungen unpolarisierter Partondistributionsfunktionen (CTEQ6 und MSTW) als Eingabedaten verwendet wurden. Es konnten fünf verschiedene Fragmentationsfunktionen (D_{fav}, D_{unf} für Pionen und D_{str}, D_{fav}, D_{unf} für Kaonen) in vier z-Intervallen extrahiert werden. Die Stabilität der Ergebnisse wurde überprüft, unter anderem durch Einschränkung des x-Bereichs der in der Analyse verwendeten Multiplizitäten und Partondistributionsfunktionen. Als weiterer Test wurden die experimentellen Multiplizitäten durch künstliche ersetzt, die mit Hilfe des Elementarteilchen-Physik-Generators PYTHIA erstellt wurden, und die Ergebnisse der beiden Extraktionen verglichen.

Die Ergebnisse für vier der fünf extrahierten Fragmentationsfunktionen - D_{fav} and D_{unf} für sowohl Pionen als auch Kaonen - sind stabil in Hinsicht auf die verwendeten Partondistributionsfunktionen, und ebenso für die unterschiedlichen x-Bereiche, in denen die Analyse durchgeführt wurde. Sie stimmen überein mit den Ergebnissen einer früheren Extraktion, die von der EMC-Kollaboration durchgeführt wurde. Die extrahierten Werte für die fünfte Fragmentationsfunktion, D_{str} für geladene Kaonen, sind stark von der verwendeten Parametrisierung der Partondistributionsfunktionen abhängig, und die Ergebnisse für verschiedene x-Intervalle sind nicht miteinander vereinbar. Die Werte für D_{str} sind in mehreren Fällen negativ - und damit physikalisch unmöglich, und widersprechen den vorhandenen Parametrisierungen.

Contents

Chapter 1

Introduction and Outline

Understanding the fundamental structure of matter, its constituents and their interactions, is one of the central goals of physics. To our present knowledge matter is composed of two types of elementary particles: leptons and quarks. In addition to those there are the gauge bosons of the four fundamental interactions (electromagnetic, strong and weak interaction, and gravitation).

The static quark model describes the constituents of the atomic nucleus - the nucleons - as composed of three quarks, called valence quarks, with fractional electric charge values (either $1/3$ or $2/3$ of the elementary charge) and a spin of $1/2\,\hbar$. According to the theory of quantum chromodynamics the valence quarks are held together by gluons, the gauge bosons of the strong interaction, and are surrounded by a 'sea' of quark-antiquark pairs, which are produced and annihilated via the exchange of gluons.

It was assumed for a long time that the nucleon spin was composed of the spin of the three valence quarks, just like the electric charge of the nucleon is composed of the fractional charges of the valence quarks. Experiments with deep-inelastic scattering (DIS) in the late 1980s (notably by the European Muon Collaboration at CERN) however indicated that the spin carried by the valence quarks was not sufficient to account for the total nucleon spin. These findings were so astonishing that for a time the problem of the missing spin was referred to as 'spin crisis'.

It is known by now that the spin structure of the nucleon is more complex. Not only the spin carried by the valence quarks contributes to the nucleon spin. Part of its angular momentum must be carried by the sea quarks and gluons, and by gluon and quark orbital angular momentum.

This is expressed in the relation

$$\frac{1}{2} = \frac{1}{2}\Delta\Sigma + \Delta G + L_q + L_g, \tag{1.1}$$

where $\Delta\Sigma$ - normalised to 1 - is the contribution of the quark spins, ΔG the contribution of the spins of the gluons, and L_q and L_g the respective contributions of the quark and gluon orbital angular momentum. The quark spin contribution can be further broken down into the helicity distributions of the different quark and antiquark flavours; $\Delta\Sigma = \Delta u + \Delta d + \Delta s + \Delta\bar{u} + \Delta\bar{d} + \Delta\bar{s}$. The contributions of charm or heavier quarks are anticipated to be very small and are therefore neglected.

Deep-inelastic scattering has proved to be an effective method to investigate the nucleon spin structure. The contribution of the quark spins to the total spin of the nucleon can be accessed by measuring *spin asymmetries* in polarised deep-inelastic scattering of muons off nucleons. Semi-inclusive DIS cross section asymmetries, where in addition to the scattered lepton hadrons, i.e. pions and kaons, are detected are sensitive to the individual quark and antiquark flavours.

While evaluations of the parton helicity distributions do exist, their uncertainties are still significant, particularly for low values of the Bjorken scaling variable x. New analyses of data with improved precision, covering a large region of x, should help to clarify some of the challenging observations made in the last few years. One of these observations regards discrepancies in measurements of Δs, the contribution of the strange quarks to the nucleon spin. Although inclusive DIS data indicate a large and negative strange quark contribution, semi-inclusive measurements of Δs as a function of x appear to be compatible with zero, or even slightly positive, at least in the measured x range.

A possible explanation for this incongruity may be found in the dependency of the results on the precise knowledge of two basic quantities: the unpolarised parton distribution functions (PDFs) describing the distribution of the nucleon momentum among its constituents, and the fragmentation functions (FFs), which describe the distribution of the parton momentum among the hadrons produced in the fragmentation of the partons (and thus provide a probability estimate for a quark of a particular flavour fragmenting into a hadron of a particular type). The significance of fragmentation functions has only become evident in the last few years, since semi-inclusive DIS has become available as a tool to explore the parton spin distributions. Neither the unpolarised PDFs nor the fragmentation functions can be described by perturbation theory; they can only be inferred from experimental data. While the unpolarised PDFs are quite well determined today, the fragmentation functions are still poorly known. Only few parametrisations of FFs are available, sometimes differing significantly from each other, in particular for strange quarks.

The method for determining fragmentation functions was to fit experimental data, using various leading order or non-leading order ansätze, both for the cross section of the considered process and for the FFs. The data used in these analyses are mainly electron-positron annihilation into charged hadrons. Some parametrisations use complementary information from proton-proton collisions, and deep-inelastic lepton-nucleon scattering.

The work presented here introduces a method for the extraction of fragmentation functions from semi-inclusive scattering data collected by the COMPASS collaboration at CERN, in particular charged pion and kaon multiplicities extracted from data recorded in 2004.

The thesis is organised as follows:

The next chapter gives an introduction to the formalism of deep-inelastic lepton-nucleon scattering, including the special cases of inclusive and semi-inclusive cross sections. The factorisation of polarised parton distributions is discussed and a method of their extraction via spin asymmetries is introduced. Finally the concept of fragmentation functions is explained, as well as their influence on the extracted helicity distributions.

Chapter 3 introduces the experimental set-up of the COMPASS experiment. Here the focus is on the description of the detector elements relevant for the analysis of the data.

The next chapter reports on a previous evaluation of quark helicity distributions by the COMPASS collaboration, demonstrating that precise knowledge of fragmentation functions is a crucial factor in the investigation of the nucleon spin structure.

Chapter 5 covers the extraction of fragmentation functions from COMPASS data. The method of extraction is derived and explained, the hadron multiplicities extracted from COMPASS data are introduced and discussed, as well as the parametrisations for the unpolarised PDFs used in the analysis.

In Chapter 6 the results for the fragmentation functions are presented and discussed.

The summary and outlook in Chapter 7 complete this thesis.

Chapter 2

Formalism of Deep-Inelastic Scattering

The spin structure of the nucleon, in particular the contributions of the quarks, can be studied through polarised deep-inelastic lepton-nucleon scattering.

This chapter will give an introduction to deep-inelastic scattering, its formalism, and its interpretation in the quark parton model (QPM). The special cases of *inclusive* and *semi-inclusive* cross sections will be explained, with emphasis on polarised semi-inclusive DIS. Following this, it will be discussed how polarised parton distribution functions can be extracted via the measuring of *spin asymmetries*. Finally, these definitions and quantities will be used to explain the concept and structure of quark *fragmentation functions*, with special weight given to their influence on the extracted helicity distributions.

2.1   Deep-Inelastic Lepton-Nucleon Scattering

The scattering of a high energy lepton (l) off a nucleon (N) is represented by the following process:

$$l + N \rightarrow l' + X, \tag{2.1}$$

where l' is the scattered lepton and X the unidentified remains. This process is defined as deep-inelastic if the mass of the final state M_X is much larger than the masses of nucleon resonances. In the final state either only the scattered lepton (inclusive process), or the scattered lepton as well as part of the hadronic final state X (semi-inclusive process) are observed.

2.1.1   Inclusive Lepton-Nucleon Scattering

Figure 2.1 illustrates the concept and kinematic of the deep-inelastic scattering process. The variables in parentheses denote the four-vectors of each particle.
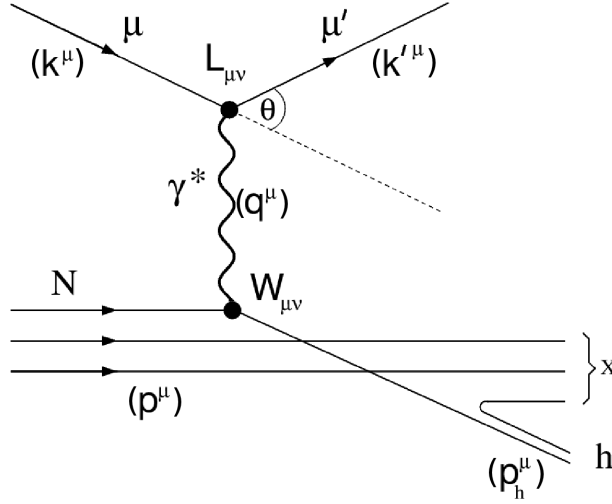
Figure 2.1: Concept and kinematic of deep-inelastic lepton-nucleon scattering. μ (μ') denotes the ingoing (outgoing) muon, γ^* the virtual photon, N the incoming nucleon, h the produced hadron, and x the unidentified remains. The variables in parenthesis denote the four-vectors of each particle.

The salient variables of deep-inelastic scattering are Q^2, the squared four-momentum transfer, and x, the Bjorken scaling variable; all variables used in the following are listed in Table 2.1.

In the kinematic range of the COMPASS experiment the exchange of a single virtual photon is most likely [1], the contribution of weak interaction is neglectable. The cross section for this process can be written as a combination of a leptonic and a hadronic tensor [2]:

$$\frac{d^2\sigma}{dxdy} \sim \underbrace{L_{\mu\nu}(k,k',s)}_{\text{lep. tensor}} \cdot \overbrace{W_{\mu\nu}(P,q,S)}^{\text{had. tensor}} \frac{\alpha^2}{Q^4}, \tag{2.2}$$

where α denotes the fine structure constant[1]. For the unpolarised process the leptonic tensor is given by:

$$L^{\mu\nu} = \frac{1}{2}\sum_{s,s'} <k'|j^\mu(0)|k><k'|j^\nu(0)|k>, \tag{2.3}$$

---

[1]Fine structure constant: The current value of $\alpha = 7.2973525698(24) \times 10^3 = 1/137.035999074(44)$

with j^μ as the operator for the electromagnetic lepton flux. The sum here runs over all the possible spin states. For a point-like particle with mass m and spin $\frac{1}{2}$ the tensor is:

$$L^{\mu\nu} = 2(k'^\mu k^\nu + k^\mu k'^\nu + (k \cdot k' - m^2)g^{\mu\nu}). \tag{2.4}$$

The corresponding hadronic tensor is:

$$W_{\mu\nu} = \frac{1}{4\pi} \sum_{X,S} < p, S|J_\mu(0)|X >< X|J_\nu(0)|p, S > (2\pi)^4 \delta^4(p + q - p_x), \tag{2.5}$$

with the sum running over all possible hadronic final states and spin states of the nucleon. J_μ is the hadronic electromagnetic flux operator.

The nucleon is not a point-like particle, it has an inner structure. On account of this the hadronic tensor cannot be boiled down to a simpler form like the leptonic one. For the parity conserving electromagnetic interaction the $W_{\mu\nu}$ can be parametrised by means of two structure functions:

$$W_{\mu\nu} = \mathbf{W_1} \left(-g_{\mu\nu} + \frac{q_\mu q_\nu}{q^2} \right) + \frac{\mathbf{W_2}}{M^2} T_\mu T_\nu, \tag{2.6}$$

$$\text{with} \quad T_\mu := p_\mu - \frac{p \cdot q}{q^2} q_\mu. \tag{2.7}$$

The structure functions W_1 and W_2 depend on invariants formed by the participating four-vectors, which in this case are:

$$p^2, q^2, p \cdot q.$$

In the target rest frame $p^2 \equiv M^2$ applies, so that p^2 is a constant. The structure functions depend on any combination of the scalars q^2 and $p \cdot q$. For the next step the squared four-momentum Q^2 and the scaling variable x are chosen as their new argument.

Contraction of the leptonic and hadronic tensors yields for the cross section:

$$\frac{d\sigma^{lN \to l'X}}{dxdy} = \frac{8\pi ME\alpha^2}{Q^4} [xy^2 \mathbf{F_1}(x, Q^2) + (1 - y - \frac{y^2\gamma^2}{4})\mathbf{F_2}(x, Q)], \tag{2.8}$$

with $\gamma^2 = (2Mx)/(Ey) = Q^2/\nu$. The lepton mass is neglected here. The new structure functions F_1 and F_2 are given by:

$$\mathbf{F_1}(x, Q^2) = M\mathbf{W_1}(x, Q^2) \tag{2.9}$$

$$\mathbf{F_2}(x, Q^2) = \nu\mathbf{W_2}(x, Q^2). \tag{2.10}$$

Variable	Meaning
Deep-inelastic lepton-nucleon scattering, inclusive case	
m	Lepton mass
M	Nucleon mass
M_X	Mass of the hadronic final state
k (k')	Four-vector of incident (scattered) lepton
s (s')	Spin four-vector of incident (scattered) lepton
p	Four-vector of nucleon in initial state
S	Spin four-vector of nucleon in initial state
p_X	Four-vector of hadronic final state
θ_l	Scatter angle of lepton in rest frame
θ_γ	Scatter angle of photon relative to the lepton in rest frame
$E = \frac{p \cdot k}{M}$	Energy of incident lepton in rest frame
$E' = \frac{p \cdot k'}{M}$	Energy of scattered lepton in rest frame
$q = k - k'$	Four-momentum transfer
$Q^2 = -q^2$	Four-momentum squared
$\nu = E - E' = \frac{p \cdot q}{M}$	Energy transfer in rest frame
$W^2 = (p + q)^2$	Mass of the hadronic final state squared
$x = \frac{Q^2}{2p \cdot q} \overset{(lab)}{=} \frac{Q^2}{2M\nu}$	Bjorken scaling variable ($0 \leq x \leq 1$)
$y = \frac{p \cdot q}{p \cdot k} = \frac{\nu}{E}$	Energy transfer from photon to quark
$\gamma^2 = \frac{2Mx}{Ey} = \frac{Q^2}{\nu^2}$	
Deep-inelastic lepton nucleon scattering, semi-inclusive case	
m_h	Mass of the observed hadron
p_h	Four-momentum of the observed hadron
$z = \frac{p \cdot p_h}{p \cdot q} = \frac{E_h}{\nu}$	Energy fraction of the observed hadron (lab system)
$p_{h\parallel} = \frac{\vec{p_h}\vec{q}}{\lvert\vec{q}\rvert}$	Longitudinal momentum component of the observed hadron, relative to the photon
$p_{h\perp} = \sqrt{\vec{p_h^2} - \vec{p_{h\parallel}^2}}$	Transverse momentum component of the observed hadron, relative to the photon
θ_h	Angle between observed hadron and virtual photon
ϕ_h	Azimuthal angle of the observed hadron (lab system)
$\vec{q*}$	Three-momentum of the virtual photon
$\vec{p*}_h$	Three-momentum of the observed hadron
$p*_{h\parallel}$	Momentum fraction of the observed hadron parallel to the momentum of the virtual photon (photon-nucleon rest frame)

Table 2.1: Variables used in deep-inelastic scattering

2.1.2   Semi-Inclusive Lepton-Nucleon Scattering

In semi-inclusive measurements a final state hadron is observed in addition to the scattered lepton. The kinematic variables relevant to the process are introduced in Fig. 2.2 and Table 2.1. The most important one for semi-inclusive lepton-nucleon-scattering is another scaling variable:

$$z = \frac{p \cdot p_h}{p \cdot q} = \frac{E_h}{\nu}. \tag{2.11}$$

It is equal to the energy fraction of the virtual photon transferred to the produced hadron in the lab frame (equivalent to the target rest frame) of reference. Additional to the inclusive variables another independent four-vector is introduced here, the hadron momentum p_h. The six invariants composed of the variables p, q and p_h are:

$$p^2, \quad q^2, \quad p_h^2, \quad p \cdot q, \quad p \cdot p_h, \quad q \cdot p_h.$$

Two of these are constants, $p^2 \equiv M^2$ and $p_h^2 \equiv m_h^2$, which leaves the following variables for the description of the semi-inclusive scattering process. Already known from the inclusive process are $Q^2 = -q^2$ and $\nu = (p \cdot q)/M$. For the additional variables one finds in the lab frame of reference:

$$
\begin{aligned}
p \cdot p_h &= M E_h = M \nu z\,, && (2.12) \\
q \cdot p_h &= \nu E_h - \vec{q} \cdot \vec{p}_h \\
&= \nu E_h - |\vec{q}||\vec{p}_h| cos(\theta_h) \\
&= \nu^2 z - |\vec{q}| p_{h\parallel} \\
&= \nu^2 z - |\vec{q}| \sqrt{(z\nu)^2 - m_h^2 - p_{h\perp}^2}\,. && (2.13)
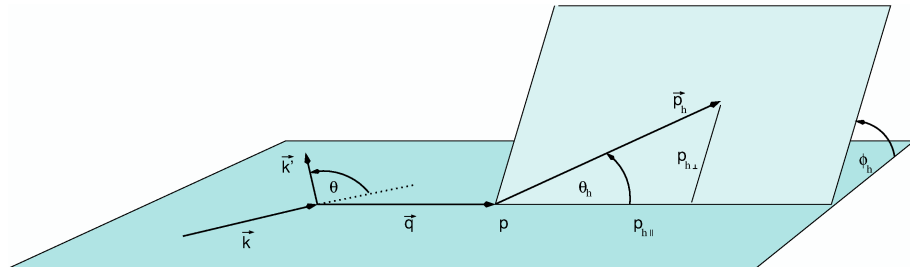\end{aligned}
$$

Figure 2.2: Kinematic of semi-inclusive deep-inelastic lepton-nucleon-scattering in the lab system.

The cross section for semi-inclusive processes can be parametrised with four structure functions, H_1 - H_4 [3]. As arguments for the four structure functions are chosen x, Q^2, the energy fraction of the virtual photon carried by the produced hadron, z, and the transverse momentum of the produced hadron in the lab frame, $p_{h\perp}$. As shown in Eq.s 2.12 and 2.13 these arguments can be expressed by the four remaining invariables q^2, $p \cdot q$, $p \cdot p_h$, $q \cdot p_h$.

$$
\begin{aligned}
\frac{d\sigma^{lN \to l'X}}{dxdzdyp_{h\perp}^2 d\phi_h} = {} & \frac{4\pi M E \alpha^2}{Q^4} \frac{E_h}{p_{h\perp}} \left[xy^2 \mathbf{H_1} + (1 - y - \frac{y^2\gamma^2}{4})\mathbf{H_2} \right] \\
& + \frac{|p_{h\perp}|}{Q}(2 - y)\sqrt{\frac{1 - y - \frac{y^2\gamma^2}{4}}{1 + \gamma^2}} \cos(\phi_h)\mathbf{H_3} \\
& + \frac{|p_{h\perp}|^2}{Q^2} \frac{(1 - y - \frac{y^2\gamma^2}{4})}{1 + \gamma^2} \cos(2\phi_h)\mathbf{H_4},
\end{aligned}
\tag{2.14}
$$

with $H_i = H_i(x, z, y, Q^2)$. As before (cf. Eq. 2.8) the lepton mass is neglected.

Since the structure functions are not dependent on the azimuthal angle ϕ_h one can integrate over ϕ_h, thus obtaining a cross section with only two of the structure functions, H_1 and H_2, contributing. A second integration, over $p_{h\perp}$, yields for the cross section:

$$
\frac{d\sigma^{lN \to l'hX}}{dxdydz} = \frac{8\pi M E \alpha^2}{Q^4} \left[xy^2 \mathbf{F_1^h} + (1 - y + \frac{y^2\gamma^2}{4})\mathbf{F_2^h} \right],
\tag{2.15}
$$

with the structure functions F_1^h and F_2^h:

$$
\begin{aligned}
\mathbf{F_i^h}(x, Q^2, z) :={} & \frac{1}{2} \int \int d\phi_{h\perp}^2 \mathbf{H_i}(x, Q^2, z, p_{h\perp}) \\
={} & \pi \int d\phi_{h\perp}^2 \mathbf{H_i}(x, Q^2, z, p_{h\perp}), \quad i = 1, 2.
\end{aligned}
\tag{2.16}
$$

The kinematic prefactors before F_1^h and F_2^h are the same as the ones before F_1 and F_2 in the inclusive cross section (cf. Eq. 2.8). The relation between the structure functions F_1^h, F_2^h and F_1, F_2 is:

$$
n^h(x, Q^2)\mathbf{F_i}(x, Q^2) = \int dz \mathbf{F_i^h}(x, z, Q^2), \quad i = 1, 2,
\tag{2.17}
$$

where $n^h(x, Q^2)$ is the multiplicity of a hadron h:

$$
n^h(x, Q^2) = \frac{1}{\frac{dN^l(x,Q^2)}{dxdQ^2}} \int_0^1 \frac{dN^h(x, Q^2, z)}{dxdQ^2dz} dz,
\tag{2.18}
$$

with N^l and N^h the numbers of scattered leptons and produced hadrons, respectively.

2.2 The Quark Parton Model
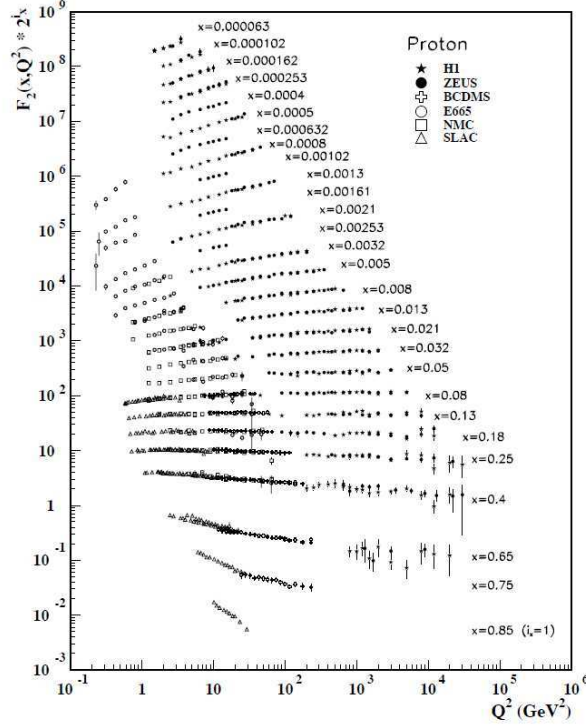
Figure 2.3: The proton structure function F_2 as a function of Q^2 for different values of x [4].

The measurement of the structure functions F_1 and F_2 in the range of $0.1 \lesssim x \lesssim 0.3$ shows only a very weak dependence on Q^2 for $Q^2 > 1\,(\text{GeV/c})^2$. Figure 2.3 shows F_2 as a function of Q^2 for different values of x. James Bjorken predicted this kind of scaling [5] for the limit $Q^2, \nu \to \infty$, with $\frac{Q^2}{2M\nu} = const$. This phenomenon can be explained with the quark parton model (QPM).

2.2.1 Inclusive Processes in the QPM

In the QPM the deep-inelastic scattering process is regarded as an incoherent superposition of elastic scattering processes, not on the nucleon itself, but on its constituents, the partons (see Fig. 2.4). This perspective is only valid, however, if the momentum transfer Q^2 is large enough to resolve the partons within the nucleon.

In a fast moving frame of reference the nucleon can be regarded as a parallel beam of partons without transverse momentum. In this system each parton carries a fraction ϵ of the nucleon momentum. For electromagnetic scattering on a free parton with the mass m_p and the momentum $p_p = \epsilon_p$ the following condition applies:

$$(p_p + q) = p'_p \tag{2.19}$$

$$\Rightarrow m_p^2 + 2\epsilon pq - Q^2 = m_p^2$$
$$\Rightarrow \epsilon = \frac{Q^2}{2pq} = x. \tag{2.20}$$

This means that the Bjorken scaling variable x is actually the fraction of the nucleon momentum carried by the parton before the scattering process. If the partons are quarks and therefore point-like spin $\frac{1}{2}$ particles, the corresponding structure functions F_1^Q and F_2^Q are given (cf. cross section for point-like spin $\frac{1}{2}$ particles in Eq. 2.8) by:

$$\mathbf{F_1^Q} = e_q^2 \frac{1}{2} \frac{Q^2}{2m_p \nu x} \cdot \delta \left(1 - \frac{Q^2}{2m_p \nu} \right) \quad \text{and}$$
$$\mathbf{F_2^Q} = e_q^2 \delta \left(1 - \frac{Q^2}{2m_p \nu} \right), \tag{2.21}$$

with e_q and m_p representing charge and mass of the quark. Using the relation $m_p = xM$ reveals that F_1^Q and F_2^Q only depend on the ratio $\frac{Q^2}{2M\nu} = x$.

Figure 2.4: Kinematic of deep-inelastic lepton-nucleon scattering in the quark parton model

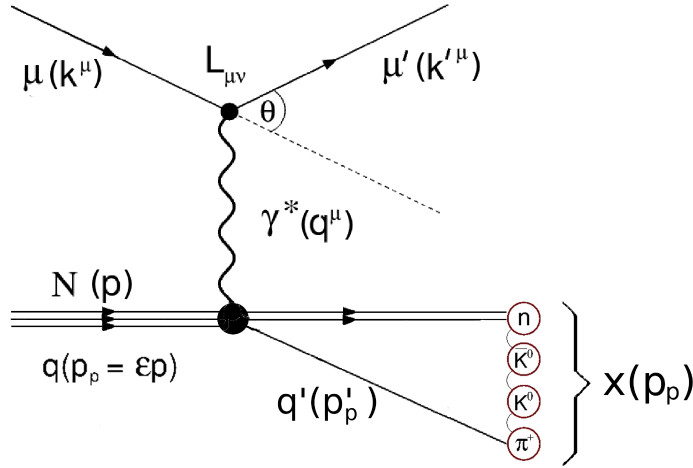The scattering process can be considered as incoherent superposition of scattering processes on the quarks in the QPM. Therefore, the next step is to introduce the quark

distributions $q(x)$. Integrated over x, they yield the number of quarks of the flavour q carrying a fraction of the nucleon momentum in the interval $[x, x+dx]$. Using these definitions, the quark structure functions can now be written as:

$$\mathbf{F_1}(x) = \frac{1}{2} \sum_q e_q^2 q(x) \quad \text{and}$$

$$\mathbf{F_2}(x) = x \sum_q e_q^2 q(x), \tag{2.22}$$

with the sum running over the six light quarks u, d, s, $\bar{u}$, $\bar{d}$ and $\bar{s}$. For typical COMPASS energies ($E \approx 160\,\text{GeV}$) the contributions of the heavier quarks can be neglected. Equation 2.22 leads to the Callan-Gross relation:

$$2x\mathbf{F_1}(x) = \mathbf{F_2}(x), \tag{2.23}$$

which origins from the assumption that quarks are spin $\frac{1}{2}$ particles [6]. The structure function ratio R helps to understand this. It is given by the ratio of cross sections for the absorption on longitudinally[2] (σ_L) and transversally (σ_T) polarised virtual photons:

$$R = \frac{\sigma_L}{\sigma_T} = \frac{\mathbf{F_2}(1 + \gamma^2) - 2x\mathbf{F_1}}{2x\mathbf{F_1}} \approx \frac{\mathbf{F_2} - 2x\mathbf{F_1}}{2x\mathbf{F_1}}. \tag{2.24}$$

Due to the preservation of angular momentum a longitudinally polarised virtual photon cannot be absorbed by a quark, if the quark is considered massless. Therefore the assumptions $\sigma_L = 0$, and consequently $R = 0$, are valid. For charged partons which are spin 0 particles, $\sigma_T = 0$ and, accordingly, $R = \infty$ would be expected [7].

Measurements of R as a function of x (cf. Fig. 2.5) show that the constituents of the nucleon are spin $\frac{1}{2}$ particles and as such can be identified as quarks.

The QPM explains why the structure functions do not depend on the momentum transfer Q^2 as well as the validity of the Callan-Gross relation. The cross section in the QPM adopts now the following form:

$$\frac{d\sigma^{lN \to l'N}}{dxdy} = \frac{8\pi\alpha^2 ME}{Q^2} \left[\frac{1}{2}y^2 + (1 - y - \frac{y^2\gamma^2}{4}) \right] \mathbf{F_2}(x)$$

$$= \frac{8\pi\alpha^2 ME}{Q^2} \left[\frac{1}{2}y^2 + (1 - y - \frac{y^2\gamma^2}{4}) \right] x \sum_i e_q^2 q(x). \tag{2.25}$$

---

[2]Longitudinal polarisation is signified by lepton and nucleon spin orientation parallel (↑↑) or antiparallel (↑↓) to the lepton momentum vector.
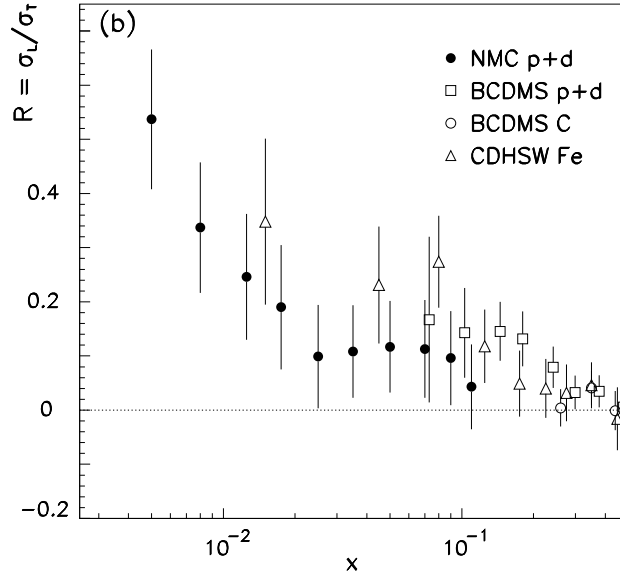
Figure 2.5: Measurements of R. The cross section ratio $R = \sigma_L/\sigma_T = (F_2(1+\gamma^2)-2xF_1)/(2xF_1)$ as a function of x. The mean value of Q^2 varies from $1.3\,(\text{GeV/c})^2$ in the first x bin to $20.6\,(\text{GeV/c})^2$ in the last x bin [8].

2.2.2   Semi-Inclusive Processes in the QPM

To apply the QPM to semi-inclusive processes, a description of the *hadronisation* of the struck quark is needed. Just as a nucleon can be regarded as a beam of partons, a fast moving quark can be regarded as a source of hadrons with negligible transverse momentum in the final state. Each hadron is carrying a fraction ξ of the quark momentum p'_q:

$$p_h = \xi p'_p = \xi(xp + q). \tag{2.26}$$

Analogous to the quark distributions, fragmentation functions $D_q^h(\xi)$ are introduced, with the integral over $d\xi$ being the number of hadrons of the type h produced from the quark in the momentum window $[\xi, \xi + d\xi]$. Multiplying Eq. 2.26 with p yields:

$$\begin{aligned}
p \cdot p_h &= \xi p(xp + q) \\
&= \xi(xp^2 + p \cdot q) \\
&\approx \xi p \cdot q
\end{aligned} \tag{2.27}$$

$$\Rightarrow \xi = \frac{p \cdot p_h}{p \cdot q} = z. \tag{2.28}$$

Consequently ξ is identical to the scaling variable z, revealing z as the momentum fraction of the struck quark carried by the hadron. Considering the parallels between the quark distributions $q(x)$ and the fragmentation functions $D_q^h(z)$:

- $q(x)$: number of quarks q with momentum fraction x in hadron h,

- $D_q^h(z)$: number of hadrons h with momentum fraction z in quark q.

This leads to the assumption that the fragmentation of a quark into hadrons does not depend on the quark's origin. The creation of hadrons in deep-inelastic scattering is consequently described by a product of two independent processes:

- absorption of a virtual photon γ^* by a quark q,

- fragmentation of a quark q into a hadron h.

The probability of the first process is proportional to $e_q^2 q(x)$, whereas the second one depends on $D_q^h(z)$. This justifies a factorisation ansatz for the structure functions F_1^h and F_2^h:

$$
\begin{aligned}
\mathbf{F_1^h}(x, z) &= \frac{1}{2} \sum_q e_q^2 q(x) D_q^h(z) \\
\mathbf{F_2^h}(x, z) &= x \sum_q e_q^2 q(x) D_q^h(z) \quad \text{with } q = u, d, s, \bar{u}, \bar{d}, \bar{s},.
\end{aligned}
\tag{2.29}
$$

The corresponding cross section is:

$$
\begin{aligned}
\frac{d\sigma^{lN \to l'hX}}{dx\,dy\,dz} &= \frac{8\pi\alpha^2 ME}{Q^4} \left[\frac{1}{2} y^2 + (1 - y - \frac{y^2\gamma^2}{4}) \right] \mathbf{F_2^h}(x, z) \\
&= \frac{8\pi\alpha^2 ME}{Q^4} \left[\frac{1}{2} y^2 + (1 - y - \frac{y^2\gamma^2}{4}) \right] x \sum_q e_q^2 q(x) D_q^h(z).
\end{aligned}
\tag{2.30}
$$

Dividing Eq.s 2.25 and 2.30 yields:

$$
\frac{1}{d\sigma^{lN \to l'N}} \frac{d\sigma^{lN \to l'hX}}{dz} = \frac{\sum_q e_q^2 q(x) D_q^h(z)}{\sum_q e_q^2 q(x)}.
\tag{2.31}
$$

An experimental proof of the ansatz in Eq. 2.29 is shown in Fig. 2.6. Fragmentation functions derived from e^+e^--annihilation and deep-inelastic lepton-nucleon scattering are shown to be in good agreement, regardless of origin of the fragmenting quarks [8].

Is the struck quark the origin of the produced hadrons, we speak of *current fragmentation*. However, the spectator quarks, which are not involved in the scattering process, fragment into hadrons as well; this is called *target fragmentation*.
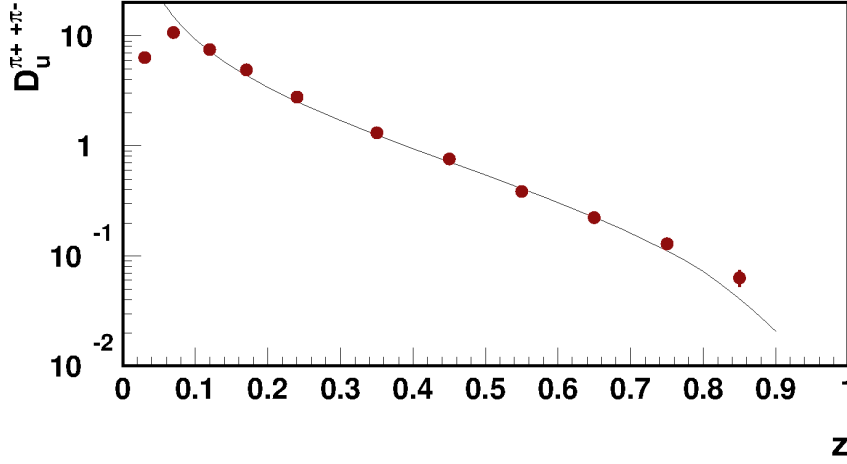
Figure 2.6: Comparison of fragmentation functions $D_u^{\pi^++\pi^-}$, extracted from data from e^+e^--production (curve, from [9]) and deep-inelastic scattering (dots, from [10]). Corrections due to the production of heavy quarks in the e^+e^--production are negligible [8].

2.2.2.1   The LUND model

The process of current and target fragmentation can be described with the aid of the LUND model [11], [12]. Figure 2.7 shows the process pictured in the photon nucleon rest frame, and follows the fragmentation process step by step. The photon is absorbed by a u quark. The u quark and the ud quark pair move away from each other, back to back. This is where the LUND model description starts. The energy of the QCD colour field between the quark and the quark pair increases with increasing distance ($\approx 1\,\mathrm{GeV}/10^{-15}\,\mathrm{m}$). At a sufficient distance and corresponding energy a new $q\bar{q}$ pair is produced. The u and $\bar{d}$ quarks form a charged pion, π^+, which carries a fraction z of the available energy. The fragmentation process continues with the remaining d quark and the ud quark pair in the same manner. Another $q\bar{q}$ pair is created, another hadron, K^0, forms, which again carries off a fraction of the remaining energy of the system. This process is repeated until all the remaining energy is exhausted.

Starting with only one quark flavour and one hadron type, a fragmentation function can be parametrised as follows [13]:

$$D(z) = \frac{1}{z}(1+c)(1-z)^c, \tag{2.32}$$

where c is a constant corresponding to experimental data.
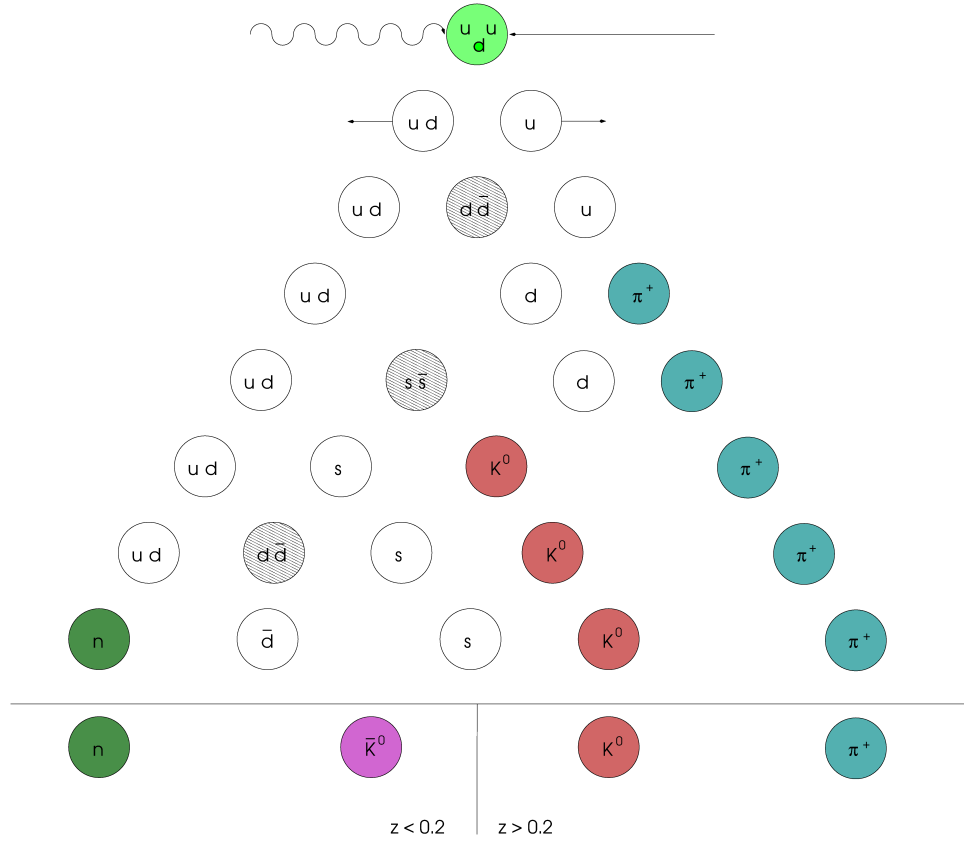
Figure 2.7: The fragmentation process in the LUND model

To expand the model to include more quark flavours and hadron types, further factors have to be included. The salient parameters and their values (taken from [13]) are:

- the probability to find a quark-antiquark pair of a particular flavour:
    - $P(u\bar{u}) : P(d\bar{d}) : P(s\bar{s}) = 1 : 1 : 0.3$,

- the probability for a produced meson having spin 1:
    - for mesons with only u- or d quarks: $P(u) = P(\bar{u}) = P(d) = P(\bar{d}) = 0.5$
    - for mesons with s quarks: $P(s) = P(\bar{s}) = 0.6$,

- the probability of creating quark pairs to produce baryons:
    - $P(u\bar{u}) : P(ud\bar{u}\bar{d}) = 1 : 0.1$.

Equation 2.32, the above listed probabilities, and further considerations detailed in [8] allow an approximation of a threshold value of z for current fragmentation in deep-inelastic scattering: $z < 0.2$ implies target fragmentation; for $z > 0.2$ current fragmentation is assumed.

2.3   Polarisation in Deep-Inelastic Lepton-Nucleon Scattering

We now examine the case of deep-inelastic scattering with both lepton and nucleon polarised before the scattering process. The polarisation in the final state is not observed.

2.3.1   Inclusive Processes

For a polarised lepton in the intial state, the leptonic tensor breaks up into two parts:

$$L^{\mu\nu} = \underbrace{L^{\mu\nu(S)}(k, k', s)}_{\text{symmetric}} + \overbrace{iL^{\mu\nu(A)}(k, k', s)}^{\text{antisymmetric}}. \tag{2.33}$$

The symmetric part $L^{\mu\nu(S)}$ is equal to the leptonic tensor in unpolarised scattering (Eq. 2.3). The antisymmetric part $iL^{\mu\nu(A)}$ is:

$$L^{\mu\nu(A)} = 2im\epsilon^{\mu\nu\alpha\beta}s_\alpha q_\beta. \tag{2.34}$$

The hadronic tensor also breaks up into two parts, symmetric and antisymmetric:

$$W_{\mu\nu} = \underbrace{W_{\mu\nu}^{(S)}(P, q, S)}_{\text{symmetric}} + \overbrace{iW_{\mu\nu}^{(A)}(P, q, S)}^{\text{antisymmetric}} \quad \text{with} \tag{2.35}$$

$$W_{\mu\nu}^{(A)} = \epsilon_{\mu\nu\alpha\beta}q^\alpha \left(\frac{S^\beta}{(p \cdot q)}\mathbf{g_1} + \frac{1}{(p \cdot q)^2}\left((p \cdot q)S^\beta - (S \cdot q)p^\beta\right)\mathbf{g_2} \right). \tag{2.36}$$

The symmetric part is again equal to the hadronic tensor in unpolarised scattering (cf. Eq. 2.5). The antisymmetric part adds two structure functions which carry information about the nucleon spin structure.

The cross section can be expressed by the contraction of the leptonic and hadronic tensors:

$$d\sigma \sim L^{\mu\nu}W_{\mu\nu}\frac{\alpha^2}{Q^4}$$
$$= \left(L^{\mu\nu(S)}W_{\mu\nu}^{(S)} + L^{\mu\nu(A)}W_{\mu\nu}^{(A)}\right)\frac{\alpha^2}{Q^4}. \tag{2.37}$$

The mixed terms $L^{\mu\nu(S)}W_{\mu\nu}^{(A)}$ and $L^{\mu\nu(A)}W_{\mu\nu}^{(S)}$ do not contribute. The symmetric parts of the tensors do not depend on the spins. Consequently only the structure functions g_1 and g_2 appear in the difference of the cross sections for parallel ($\uparrow\uparrow$) and antiparallel ($\uparrow\downarrow$) spin orientation of lepton and nucleon. In this thesis only the longitudinal polarisation (cf. Eq. 2.24 in Section 2.2.1) is of interest. Longitudinal polarisation is signified by lepton and nucleon spin orientation parallel or antiparallel to the lepton momentum vector. The cross section difference for parallel and antiparallel spin orientation is:

$$
\begin{aligned}
&\frac{d^2\sigma^{(\uparrow\downarrow)}}{dxdy} - \frac{d^2\sigma^{(\uparrow\uparrow)}}{dxdy} \\
&= \frac{32\pi ME\alpha^2 xy}{Q^4}\left[\left(1 - \frac{y}{2} - \frac{y^2\gamma^2}{4}\right)\mathbf{g_1}(x,Q^2) - \frac{y}{2}\gamma^2\mathbf{g_2}(x,Q^2)\right].
\end{aligned}
\tag{2.38}
$$

The measured quantity in the COMPASS experiment is the lepton-nucleon cross section spin asymmetry $A^{lN} = (d\sigma^{\uparrow\downarrow} - d\sigma^{\uparrow\downarrow})/(d\sigma^{\uparrow\downarrow} + d\sigma^{\uparrow\downarrow})$. It can be expressed as:

$$
A^{lN} = D\left[\frac{\mathbf{g_1} - \gamma^2\mathbf{g_2}}{\mathbf{F_1}} + \eta\gamma\frac{\mathbf{g_1} + \mathbf{g_2}}{\mathbf{F_2}}\right],
\tag{2.39}
$$

with:

$$
D = \frac{y(2-y)(1 + \frac{\gamma^2 y^2}{2})}{(1+\gamma^2)y^2 + 2(1-y-\frac{\gamma^2 y^2}{4})(1+R)},
\tag{2.40}
$$

and:

$$
\eta = \gamma\frac{1 - y - \frac{\gamma^2 y^2}{4}}{(1-\frac{y}{2})(1+\frac{\gamma^2 y}{2})}.
\tag{2.41}
$$

Only the lepton mass was neglected here. By neglecting the nucleon mass as well (by assuming $M \ll E$) Eq. 2.39 simplifies to:

$$
A^{lN} = D\frac{\mathbf{g_1}}{\mathbf{F_1}}.
\tag{2.42}
$$

For the next step it is helpful to examine the asymmetry for the process $\gamma^* + N \to X$:

$$
A^{\gamma N} = \frac{\mathbf{g_1}}{\mathbf{F_1}}.
\tag{2.43}
$$

The photon-nucleon asymmetry $A^{\gamma N}$ only depends on the structure functions g_1 and F_1, not on the prefactor D. The correlation between the lepton-nucleon asymmetry and the photon-nucleon asymmetry is consequently as follows:

$$A^{lN} = D A^{\gamma N}. \tag{2.44}$$

The factor D is therefore identified as depolarisation factor, which specifies the fraction of polarisation which is transferred from lepton to photon.

2.3.1.1   Interpretation of g_1 in the QPM

To interpret the structure function g_1 in the QPM it is again useful to regard the deep-inelastic scattering process as a superposition of elastic scattering processes on the partons.
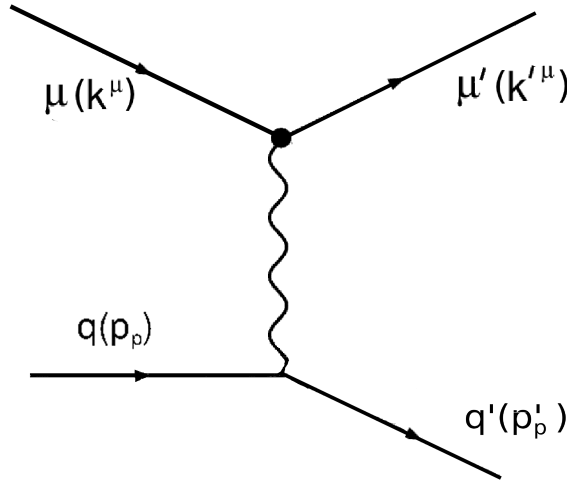
Figure 2.8: Kinematic of lepton-quark scattering

The cross section for scattering of point-like polarised spin $\frac{1}{2}$ particles (here: quarks and leptons) is proportional to:

$$
\begin{aligned}
\sigma_{lq}^{\uparrow\downarrow} &\sim (k + p_q)^4 \approx (2k \cdot p_q)^2 = (2xk \cdot p)^2 = (2xME)^2 \\
\sigma_{lq}^{\uparrow\uparrow} &\sim (k' - p_q)^4 \approx (-2k' \cdot p_q)^2 = (-2xk' \cdot p)^2 = (2xME')^2.
\end{aligned}
\tag{2.45}
$$

Assuming lepton and nucleon with antiparallel spin orientation (Fig. 2.9, left), and $q^\uparrow$ ($q^\downarrow$) the number of quarks with parallel (antiparallel) spin orientation relative to the nucleon spin, the lepton-nucleon cross section in the QPM (for one quark flavour) is then given by:
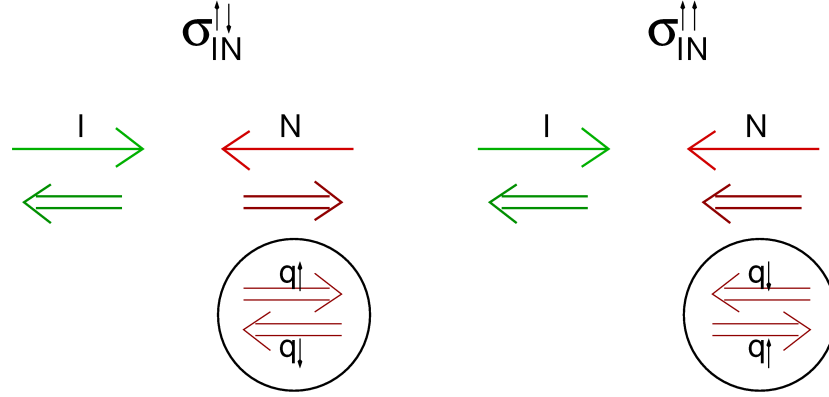
Figure 2.9: Polarised lepton-nucleon scattering in the QPM. The arrows indicate the direction of the particle momentum, double arrows the orientation of the particle spin. $q^{\downarrow}(q^{\uparrow})$ is the number of quarks with spin parallel (antiparallel) to the nucleon spin.

$$
\begin{aligned}
\sigma_{lN}^{\uparrow\downarrow} &\sim \sigma_{lq}^{\uparrow\downarrow} q^{\uparrow} + \sigma_{lq}^{\uparrow\uparrow} q^{\downarrow} \\
&\sim E^2 q^{\uparrow} + E'^2 q^{\downarrow}.
\end{aligned}
\tag{2.46}
$$

The lepton-nucleon cross section for parallel spin orientation is accordingly:

$$
\begin{aligned}
\sigma_{lN}^{\uparrow\uparrow} &\sim \sigma_{lq}^{\uparrow\uparrow} q^{\uparrow} + \sigma_{lq}^{\uparrow\downarrow} q^{\downarrow} \\
&\sim E'^2 q^{\uparrow} + E^2 q^{\downarrow}.
\end{aligned}
\tag{2.47}
$$

Applied to the asymmetry A^{lN} this yields:

$$
A^{lN} = \frac{\sigma_{lN}^{\uparrow\downarrow} - \sigma_{lN}^{\uparrow\uparrow}}{\sigma_{lN}^{\uparrow\downarrow} + \sigma_{lN}^{\uparrow\uparrow}} = \frac{E^2 - E'^2}{E^2 + E'^2} \frac{q^{\uparrow} - q^{\uparrow}}{q^{\uparrow} + q^{\uparrow}} = \frac{2y - y^2}{2 - 2y + y^2} \frac{\Delta q}{q},
\tag{2.48}
$$

with $\Delta q := q^{\uparrow} - q^{\downarrow}$ and $q := q^{\uparrow} + q^{\downarrow}$.

The last step included:

$$
\frac{E^2 - E'^2}{E^2 + E'^2} = \frac{2y - y^2}{2 - 2y + y^2} \quad \text{with} \quad y = 1 - \frac{E'}{E}.
\tag{2.49}
$$

For all quark flavours A^{lN} is as follows:

$$A^{lN}(x,y) = \frac{2y - y^2}{2 - 2y + y^2} \frac{\sum_q e_q^2 \Delta q(x)}{\sum_q e_q^2 q(x)} \quad \text{with} \quad q = u, d, s, \bar{u}, \bar{d}, \bar{s}. \tag{2.50}$$

The prefactor $(2y - y^2)/(2 - 2y + y^2)$ is equal to the depolarisation factor D in Eq. 2.44, assuming that $R \approx 0$ and $M \ll E$. In the QPM $R = 0$ approximately applies, as well as $F_1 = \frac{1}{2} \sum_q e_q^2 q(x)$. This yields for g_1:

$$\mathbf{g_1} = \frac{1}{2} \sum_q e_q^2 \Delta q(x). \tag{2.51}$$

Therefore in the QPM the structure function g_1 contains information about the helicity contribution of the quarks to the nucleon spin. The QPM term for photon-nucleon spin asymmetry does not contain any kinematic prefactors at all, the asymmetry only depends on the scaling variable x:

$$A^{\gamma N}(x) = \frac{\sum_q e_q^2 \Delta q(x)}{\sum_q e_q^2 q(x)}. \tag{2.52}$$

2.3.2   Semi-Inclusive Processes

By observing a hadron additionally to the scattered lepton, the number of the structure functions in the cross section increases to 18. As shown in Section 2.1.2, the cross section depends on four structure functions in the unpolarised case. An additional structure function contributes in case of a polarised lepton and an unpolarised nucleon. If both lepton and nucleon are polarised, 13 more structure functions are added. The complete term for this cross section can be found e.g. in [14]. As in the unpolarised case, one integrates over the azimuthal angle ϕ_h and the transverse momentum $p_{h\perp}$ of the hadron. If the hadron spin is not observed, no additional structure functions contribute to the semi-inclusive cross section, and Eq. 2.52 can be expanded to:

$$A^{\gamma N}(x, z) = \frac{\mathbf{g_1^h}}{\mathbf{F_1^h}} = \frac{\sum_q e_q^2 \Delta q(x) D_q^h(z)}{\sum_q e_q^2 q(x) D_q^h(z)} \quad \text{with} \quad q = u, d, s, \bar{u}, \bar{d}, \bar{s}. \tag{2.53}$$

For this it was assumed that fragmentation functions are not spin dependent ($D_{q\uparrow}^h = D_{q\downarrow}^h$), which is a valid assumption for a parity conserving fragmentation process if the hadron spin is not observed.

If the quark distributions $q(x)$ and the fragmentation functions $D_q^h(z)$ are known from experiments with unpolarised targets, the polarised quark distribution $\Delta q(x)$ can be determined by measuring the asymmetry $A_h^{\gamma N}(x, z)$. To quantify the additional information

that can be obtained from semi-inclusive asymmetries Eq.s 2.52 and 2.53 are broken down into contributions from q and $\bar{q}$:

$$A^{\gamma N}(x) = \frac{\sum_q e_q^2 \Big(\Delta q(x) + \Delta \bar{q}(x) \Big)}{\sum_q e_q^2 \Big(q(x) + \bar{q}(x) \Big)}, \tag{2.54}$$

$$A_h^{\gamma N}(x) = \frac{\sum_q e_q^2 \Big(\Delta q(x) D_q^h(z) + \Delta \bar{q}(x) D_{\bar{q}}^h(z) \Big)}{\sum_q e_q^2 \Big(q(x) D_q^h(z) + \bar{q}(x) D_{\bar{q}}^h(z) \Big)}, \tag{2.55}$$

with $q = u, d, s$. Equation 2.54 only yields information about helicity contributions of the sum of quarks and antiquarks $\Delta q + \Delta \bar{q}$. Equation 2.55, on the other hand, allows for a separate observation of quark and antiquark helicity contributions, since generally fragmentation functions for quarks and antiquarks are not the same ($D_q^h \neq D_{\bar{q}}^h$).

There is also not enough information in the inclusive asymmetry $A^{\gamma N}(x)$ to extract polarised quark distributions for all the quark flavours. Only two independent measurements, $A_p^{\gamma N}(x,z)$ and $A_d^{\gamma N}(x,z)$ (for a proton and a deuteron target), are possible. Scattering on a deuteron target is again regarded as an incoherent superposition of proton and neutron scattering.

Like the unpolarised quark distributions the polarised ones are given, via isospin symmetry, by the proton-quark distributions. However, semi-inclusive asymmetries also contain information about the observed hadron. So by measuring semi-inclusive asymmetries for hadrons like $h = \pi^+, \pi^-, K^+, K^-, ...$ it is possible to obtain equations for the helicity contributions of the quark flavours contained in the observed hadrons: $\Delta u(x)$, $\Delta \bar{u}(x)$, $\Delta d(x)$, $\Delta \bar{d}(x)$, $\Delta s(x)$, $\Delta \bar{s}(x)$.

2.4   Quantum Chromodynamic Effects in DIS

The last chapters described the deep-inelastic scattering in the (naïve) quark parton model only. However, the 'spin crisis' (cf. Chapter 1) led to the realisation that this simplified model failed to explain the experimental results.

The missing part of the nucleon spin was an indication that some contributions had been neglected. One of those possible contributions is the spin of the gluons. Gluons do not interact directly with the exchanged virtual photon, but they mediate the strong interaction as the exchanged gauge bosons in the field theory of Quantum Chromodynamics [15] (QCD) and lead therefore to corrections to the QPM. With these corrections the parton distributions depend on Q^2 in a way that is calculable in QCD. The formalism of the QPM remains in principle unchanged, apart from replacing $q(x)$ with $q(x, Q^2)$, which, in turn, leads to a Q^2 dependence of the structure functions F_1 and g_1 as well.

2.4.1 Q^2 Dependence of Quark Distributions and Fragmentation Functions

The interpretation of this dependence on Q^2 can be found in the interaction between quarks and gluons. The gluons as gauge bosons are radiated and re-absorbed by the quarks, but can also produce quark-antiquark pairs by themselves or radiate further gluons. These dynamics create a 'cloud' of gluons and virtual $q\bar{q}$ pairs, the so-called 'sea'.
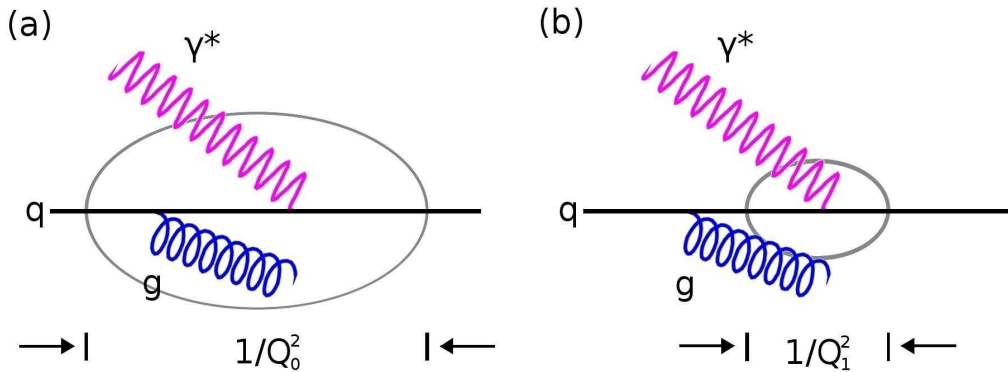
Figure 2.10: Q^2 dependence of structure functions. In Fig. (a) the photon 'sees' only the composite of quark and gluon, while in Fig. (b) the momentum transfer is large enough to resolve the quark itself.

How the outside world observes a quark therefore depends on the resolution power of the virtual photon, and can be described with the following image: A photon with the momentum transfer Q_0^2 can resolve a dimension of the scale $1/Q_0^2$. In Fig. 2.10(a) the photon therefore only 'sees' the composite of quark and emitted gluon. Is Q^2 larger, $Q_1^2 \gg Q_0^2$, the photon 'sees' only the quark (Fig. 2.10(b)). This explains, qualitatively, the increase

of the structure function F_2 for small x with increasing Q^2 (cf. Fig. 2.3), and its decrease with Q^2 for larger x. For a large Q^2 the probability of scattering on a quark carrying a small momentum fraction x increases. The Q^2 dependence of the structure functions is also known as scale breaking; the structure functions depend not only on x anymore, but also on Q^2. This has been verified by various experiments (cf. Fig. 2.11).
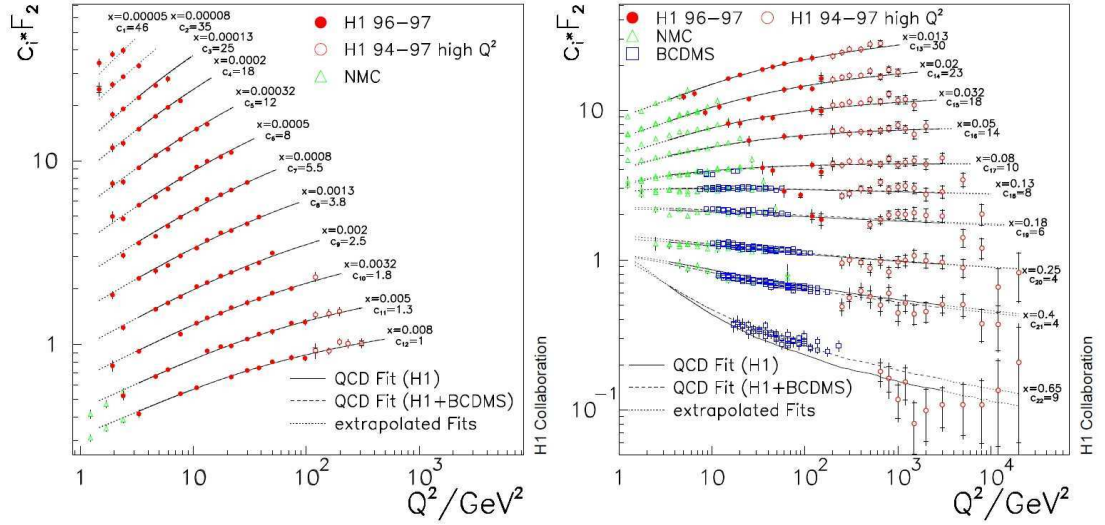
Figure 2.11: Scaling violation of the proton structure function F_2. Left: For small x the F_2 increases with increasing Q^2. Right: For $x \gtrsim 0.25$ the structure function decreases with increasing Q^2 [16].

The Q^2 evolution of the parton distributions can be calculated by using a system of linked equations, the so-called DGLAP[3] equations [18, 19, 17]. Those describe the fact that a quark with a momentum fraction x can come from a parent quark with a larger momentum which had radiated a gluon before, or from a parent gluon which had created a $q\bar{q}$ pair. If the parton distribution functions are known at a certain scale of Q^2, they can be calculated at any other scale.

Using DGLAP equations, the structure functions F_1 and F_2 in Eq. 2.22 can be expressed by exchanging the x dependent quark distributions by distributions dependent on both x and Q^2:

---

[3]DGLAP (Dokshitzer, Gribov, Lipatov, Altarelli and Parisi) were the authors who first developed the equation of the QCD evolution. DGLAP was first published outside Russia by Altarelli and Parisi in 1977 (see [17]), therefore DGLAP and its various derivations are often still called Altarelli-Parisi equations. It became known only later in the Western world that an equivalent had been published in St. Petersburg by Gribov and Lipatov already in 1972, and also by Dokshitzer in 1977.

$$\mathbf{F_1}(x, Q^2) = \frac{1}{2} \sum_q e_q^2 q(x, Q^2) \quad \text{and}$$

$$\mathbf{F_2}(x, Q^2) = x \sum_q e_q^2 q(x, Q^2). \tag{2.56}$$

The interactions between gluons and quarks also result in a Q^2 dependence of the fragmentation functions [20]. The corresponding DGLAP equations account for the possibility that the fragmentation of a parton may happen via the radiation of a second parton which fragments into a hadron.

Figure 2.12 shows a parametrisation of the fragmentation function $D_u^{\pi^+ + \pi^-}(z)$, evaluated via a fit to $e^+ e^-$-annihilation data [9]. The number of produced hadrons with a small energy fraction z increases with increasing Q^2, while the production of hadrons with a large z becomes less probable.
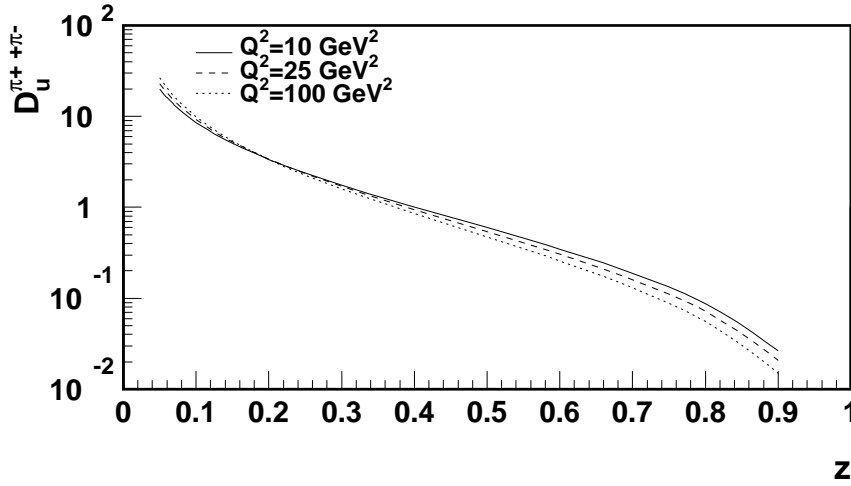

Figure 2.12: Parametrisation of the fragmentation function $D_u^{\pi^+ + \pi^-}(z)$, evaluated via a fit to $e^+ e^-$-annihilation data [9] for different values of Q^2 [8].

For semi-inclusive processes the structure functions F_1^h and F_2^h can be written as product of Q^2 dependent quark distributions and fragmentation functions [21, 22]:

$$\mathbf{F_1^h}(x, z, Q^2) = \frac{1}{2} \sum_q e_q^2 q(x, Q^2) D_q^h(z, Q^2) \quad \text{and}$$

$$\mathbf{F_2^h}(x, z, Q^2) = x \sum_q e_q^2 q(x, Q^2) D_q^h(z, Q^2). \tag{2.57}$$

The Q^2 dependence of the polarised quark distributions is determined by the fraction of the helicity transferred from the 'mother' parton to the 'daughter' parton, and can also be described by DGLAP equations. The polarised structure functions are given by:

$$\mathbf{g_1}(x, Q^2) = \frac{1}{2} \sum_q e_q^2 \Delta q(x, Q^2), \tag{2.58}$$

$$\mathbf{g_1^h}(x, z, Q^2) = \frac{1}{2} \sum_q e_q^2 \Delta q(x, Q^2) D_q^h(z, Q^2). \tag{2.59}$$

The expected effect of the Q^2 dependence of fragmentation functions is quite small (cf. Fig. 2.12). In actual measurements of inclusive and semi-inclusive asymmetries no significant dependency on Q^2 is observed, it is therefore neglected in the extraction of helicity distributions (cf. Sections 2.5 and 4.3), and all measurements are assumed to be valid at a fixed Q_0^2. The method of extraction of fragmentation functions developed in this thesis (cf. Section 5.1) also disregards the Q^2 dependence of FFs and parton distribution functions.

2.5   Fragmentation Functions

The first sections of this work presented an introduction to the concept and structure of fragmentation functions. This section will serve as an illustration of the significance of FFs regarding extracted values of Δq, and in particular for the values extracted for Δs. Results of a recent analysis [23] by the COMPASS collaboration demonstrate that a precise knowledge of fragmentation functions is not only important, but crucial for the further exploration of the spin structure of the nucleon.

In this analysis inclusive $(A_{1,d})$ and semi-inclusive asymmetries $(A_{1,d}^{\pi^+}, A_{1,d}^{\pi^-}, A_{1,d}^{K^+}, A_{1,d}^{K^-}$, see Fig. 2.13) measured in deep-inelastic muon-deuteron scattering were used to determine the polarised PDFs for valence quarks $(\Delta u_v + \Delta d_v)$, non-strange sea quarks $(\Delta \bar{u} + \Delta \bar{d})$, and strange quarks $(\Delta s$, assumed to be equal to $\Delta \bar{s})$.
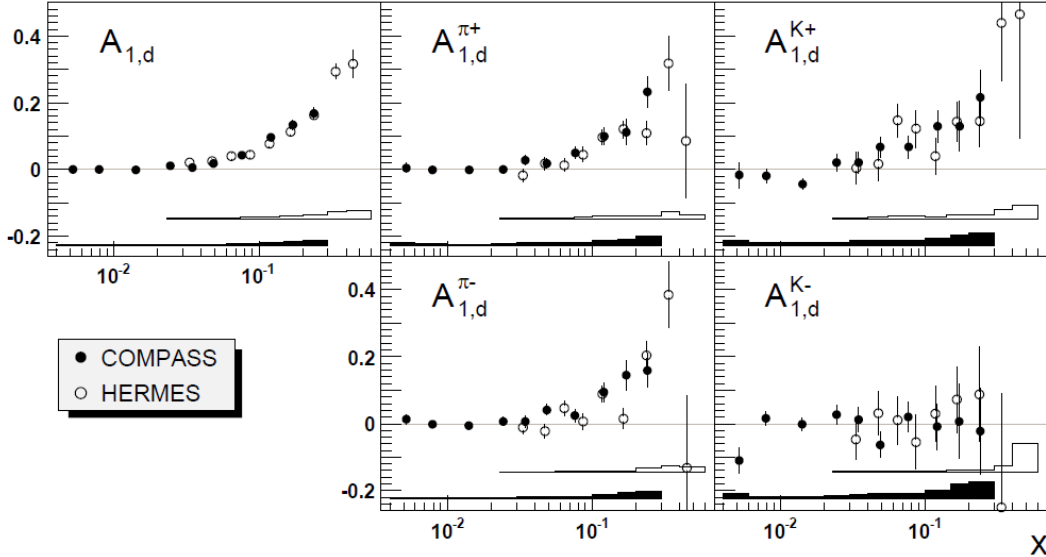
Figure 2.13: Comparison of final asymmetries of COMPASS as a function of x with results of HERMES [24]. Bands at bottom of graphs represent systematic uncertainties. Solid markers and bands correspond to COMPASS data. Open markers and bands are taken from the HERMES publication.

Assuming that hadrons in the current fragmentation region (cf. Section 2.2.2) are produced in independent quark fragmentation, their spin asymmetries can be written in terms of the parton distribution functions, $q(x, Q^2)$ and $\Delta q(x, Q^2)$, and fragmentation functions, $D_q^h(z, Q^2)$ (cf. Eq. 2.53 and Section 2.4.1). The analysis used unpolarised PDFs from MRST[4] [25], and the DSS[5] parametrisation of FFs which was obtained from a combined analysis of inclusive pion and kaon production data from e^+e^--annihilation, semi-inclusive

---

[4]MRST: A.D. Martin, R.G. Roberts, W.J. Stirling and R.S Thorne
[5]DSS: D. de Florian, R. Sassot and M. Stratmann

data from the HERMES collaboration, and proton-proton collider data [26]. To test the dependence of the polarised PDFs on the fragmentation functions, a second set of FFs was used as well, this one using data from the European Muon Collaboration (EMC) [10]. While the MRST and DSS values were derived from global fits, the EMC ones were extracted from EMC data only. The asymmetries were assumed to be independent of Q^2; therefore all PDFs were obtained at a common Q^2 fixed to $3\,(\mathrm{GeV/c})^2$.
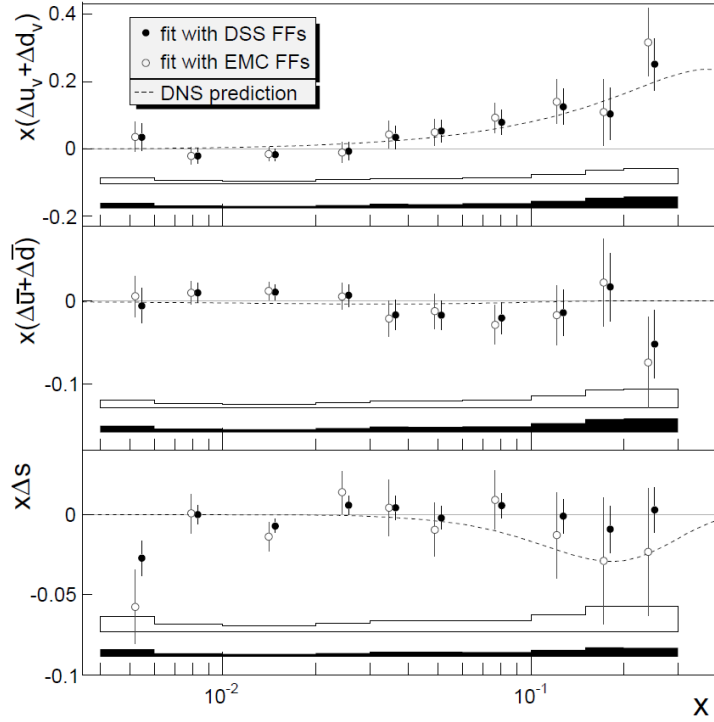
Figure 2.14: The quark helicity distributions evaluated at common value $Q^2 = 3\,(\mathrm{GeV/c})^2$ as a function of x for two sets of fragmentation functions (DSS and EMC). Bands at bottom of graphs represent systematic uncertainties. Solid markers and bands correspond to PDFs obtained with DSS parameterisation of FFs. Open markers and bands are obtained with EMC parameterisation of FFs. The curves represent the leading order DNS (D. de Florian, G.A. Navarro, R. Sassot) parameterisation of polarised PDFs [27].

The results of the fit obtained with the two sets of FFs are shown in Fig. 2.14. While the valence quark and non-strange sea quark helicity distributions show no significant dependence on the fragmentation functions used in the analysis, this is not the case for Δs. The main difference of DSS with respect to EMC is the augmented s $(\bar{s})$ quark contribution to the production of K^+ (K^-). The values extracted for Δs differ by up to a factor of two for the different parametrisations, as does their respective statistical error.

The dependence of $\Delta s(x)$ on the FFs can be further explored in relation with the charged kaon asymmetry $A_{1,d}^{K^++K^-}$. This asymmetry is the weighted average of $A_{1,d}^{K^+}$ and $A_{1,d}^{K^-}$ with weights given by the spin-averaged K^+ and K^- cross sections.

$$A_{1,d}^{K^++K^-} = \frac{\sigma^{K^+} A_{1,d}^{K^+} + \sigma^{K^-} A_{1,d}^{K^-}}{\sigma^{K^+} + \sigma^{K^-}}. \tag{2.60}$$

It has been found to be very stable with respect to the ratio $\sigma^{K^+}/\sigma^{K^-}$. A change of this ratio by $\pm 10\%$ does not alter $A_{1,d}^{K^++K}$ by more than 10% of its statistical error.

At leading order, the cross section depends only on the unpolarised PDFs and two ratios; R_{UF} and R_{SF}, which are the ratios of unfavoured to favoured and strange to favoured[6] FFs respectively:

$$R_{UF} = \frac{\int D_d^{K^+}(z)dz}{\int D_u^{K^+}(z)dz}, \quad R_{SF} = \frac{\int D_{\bar{s}}^{K^+}(z)dz}{\int D_u^{K^+}(z)dz}, \tag{2.61}$$

Both have distinct values for the used sets of fragmentation functions:

$$\begin{aligned} \text{for EMC:} \quad & R_{UF} = 0.35, R_{SF} = 3.4 \\ \text{and for DSS:} \quad & R_{UF} = 0.13, R_{SF} = 6.6. \end{aligned}$$

For an isoscalar target, the charged kaon asymmetry and the inclusive asymmetry can be written as:

$$A_{1,d}^{K^++K} = \epsilon \frac{\Delta Q + \alpha \Delta s}{Q + \alpha s}, \quad A_{1,d} = \epsilon \frac{\Delta Q + \frac{4}{5}\Delta s}{Q + \frac{4}{5}s}, \tag{2.62}$$

where $Q = u + d + \bar{u} + \bar{d}$ is the non-strange quark density, and ΔQ the corresponding helicity density, and $\alpha = (2R_{UF} + 2R_{SF})/(2 + 3R_{UF})$. The similarity between the two asymmetries can be used to write the strange quark polarisation as:

$$\frac{\Delta s}{s} = \frac{1}{\epsilon}\left[A_{1,d} + (A_{1,d}^{K^++K} - A_{1,d})\frac{Q/s + \alpha}{\alpha - 0.8}\right]. \tag{2.63}$$

The use of this formula leads to values of Δs that are nearly equal to those derived from the semi-inclusive asymmetries, with just a slightly larger statistical error.
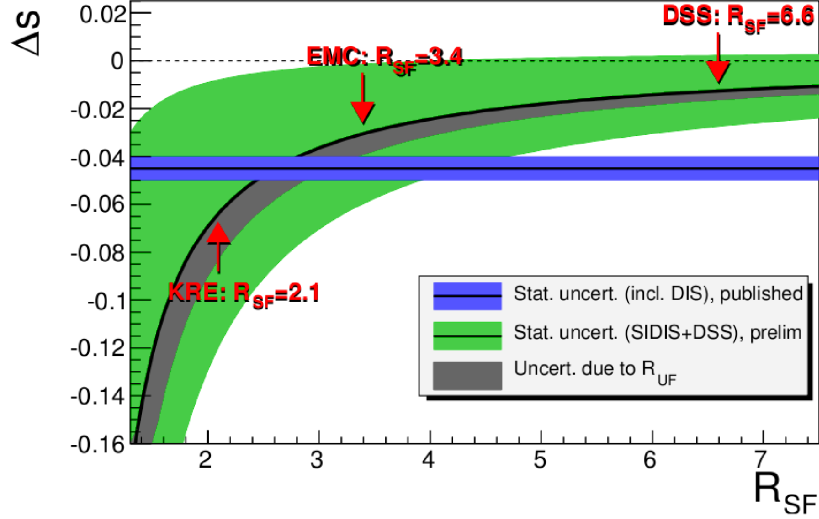
Figure 2.15: Integral of Δs over the measured range of x $(0.004 \leq x \leq 0.3)$, as a function of the ratio R_{SF} for R_{UF} fixed at the DSS value of 0.13 (black curve). The green area shows the statistical uncertainty and the grey band inside of it shows the effect of increasing R_{UF} to 0.35 (EMC value). The blue horizontal band represents the full moment of Δs derived from the COMPASS value of the first moment of $g_1^d(x)$ [23]. The values of R_{SF} corresponding to DSS [26], EMC [10] and KRE [28] parameterisations of FFs are indicated by arrows.

Figure 2.15 shows the variation of the first moment of Δs, truncated to the measured range of x, as a function of the fragmentation function ratio R_{SF}.

The integral of Δs over the measured range of x, $\int_{0.004}^{0.3} dz \Delta s$, takes on the value of -0.01 for the DSS FFs, and -0.03 for the EMC ones, although also with a much larger error. For $R_{SF} > 5$, the values of Δs are close to zero and larger than the full moment derived from the inclusive analysis by the COMPASS collaboration [29].

It is evident that the first moment and its error are very sensitive to the value of R_{SF} (and, to a lesser extent, to the value of R_{UF}), and with this to the version of fragmentation functions used in the analysis. Clearly the precise knowledge of fragmentation functions is essential for the evaluation of helicity distributions, in particular for the extracted values of Δs.

---

[6] A fragmentation function D_q^h is called favoured if the quark q is one of the valence quarks of the produced hadron h. So is, for example, $D_u^{K^+}$ a favoured FF, since $K \equiv \bar{s}u$. Correspondingly, a fragmentation function is called unfavoured if the quark q is not one of the valence quarks of h. Favoured strange quark fragmentation functions, e.g. $D_{\bar{s}}^{K^+}$ are expected to be larger in magnitude than non-strange favoured fragmentation functions. Here they are simply called strange fragmentation functions.

Chapter 3

The COMPASS Experiment

The *COmmon Muon and Proton Apparatus for Structure and Spectroscopy*, abbreviated COMPASS, is a fixed target spectrometer located at the end of the M2 beamline of the Super-Proton-Synchrotron (SPS) at CERN[1] in Geneva. The physics programme of COMPASS breaks down into two components: The *muon programme* is dedicated to the detailed study of the nucleon spin structure via deep-inelastic scattering of polarised muons off polarised nucleons. The main objectives of the COMPASS *hadron programme* are the spectroscopy of charmed hadrons and the investigation of the hadron structure by means of various hadron beams (proton, pion, kaon) colliding with a nuclear target. This chapter will give a brief overview of the COMPASS spectrometer. For a detailed description consult [1].
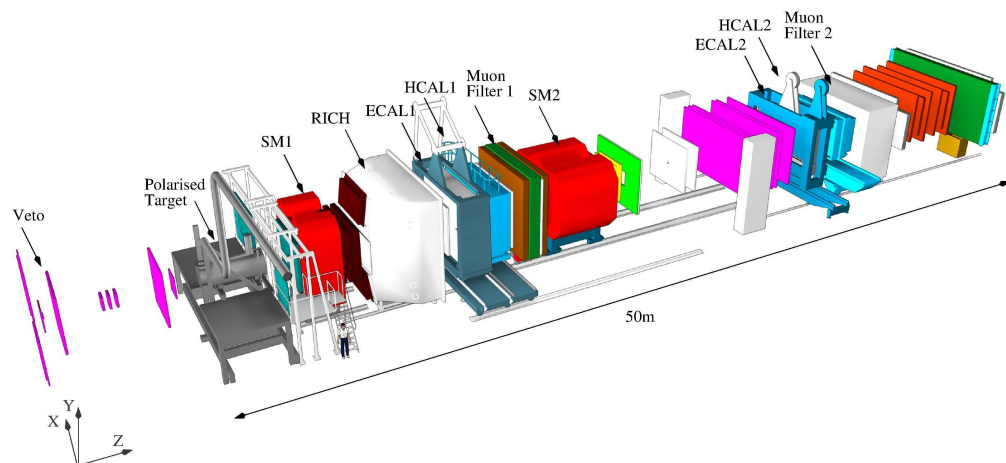

Figure 3.1: Artistic view of the COMPASS spectrometer [30]

---

[1]CERN: Conseil Européen pour la Recherche Nucléaire, European Organization for Nuclear Research

Figure 3.1 shows a schematic view of the COMPASS detector in the muon beam set-up. The beam enters from bottom left. A small fraction of the beam particles interact in the nucleon target, which can be polarised either longitudinally or transversely with respect to the beam direction. The scattered muons and the produced hadrons are detected in a 50 m long spectrometer built downstream of the target.

To ensure the detection of potentially interesting physics events, the spectrometer has to fulfill a number of specific requirements. A large interval of Q^2 has to be covered, which requires the detection of muons in a wide range of scattering angles. In order to cope with the particle rate, the spectrometer components must have a good time resolution. The rate of particles also necessitates a fast and efficient trigger system for the event selection, and a data acquisition system capable of recording a high flux of data. Track reconstruction and particle identification are essential for the identification of physics events.

In order to fulfill all of these requirements as best as possible COMPASS uses a two-stage spectrometer. The first stage is located downstream of the first spectrometer magnet (SM1). It is used to detect particles with large polar angle and small momenta. In the second stage, downstream of the second spectrometer magnet SM2, particles with small polar angles and large momenta are detected. The two stages are accordingly named large angle spectrometer (LAS) and small angle spectrometer (SAS), respectively. This setup provides a total polar acceptance of ± 180 mrad and allows measurements in a wide kinematic range. Each stage contains two calorimeters, one electromagnetic and one hadronic, and a muon filter for particle identification of electrons, hadrons and muons. In the LAS a *Ring Imaging Cherenkov* (RICH) detector provides additional particle identification of pions, kaons, protons and low energy electrons. A large variety of tracking detectors, each serving different requirements for spatial resolution, particle rate or covered solid angle, is distributed over the whole spectrometer. A system of trigger detectors allows to select events according to energy loss of the beam muons and their interaction in the target.

The COMPASS set-up is changed and improved constantly; new detectors are employed, older spectrometer components are upgraded. Additionally, the parameters of the polarised muon beam vary, depending on the demand by the various experiments provided with particles by the SPS. In order to provide an accurate description of the data used in the analysis (which is the main topic of this thesis), the following sections will give a more detailed description of the 2004 COMPASS set-up, and only occasionally include notes on later upgrades of the spectrometer. Also, a large section of this chapter is dedicated to the COMPASS trigger system. The author worked on the installation of various detectors for this system, and was responsible for its maintenance during data taking periods; it will therefore be described in more detail.

3.1   The Muon Beam

One of the distinctive features of the COMPASS experiment is the high energy polarised muon beam. The production and properties of the beam will be described in the following subsections. Fig. 3.2 shows the mechanisms and accelerators involved.

3.1.1 The Production of the Muon Beam

In the Proton Synchrotron (PS) protons are accelerated to a momentum of $14\,\text{GeV/c}$ and then injected into the Super Proton Synchrotron. The SPS accelerates the proton beam to a momentum of up to $450\,\text{GeV/c}$, which is then extracted with an intensity of approximately 2×10^{13} protons within the time of a *spill* (lasting $4.8\,\text{s}$) in each cycle. An SPS cycle includes the injection, acceleration and extraction of the protons and lasts in total $16.8\,\text{s}$.
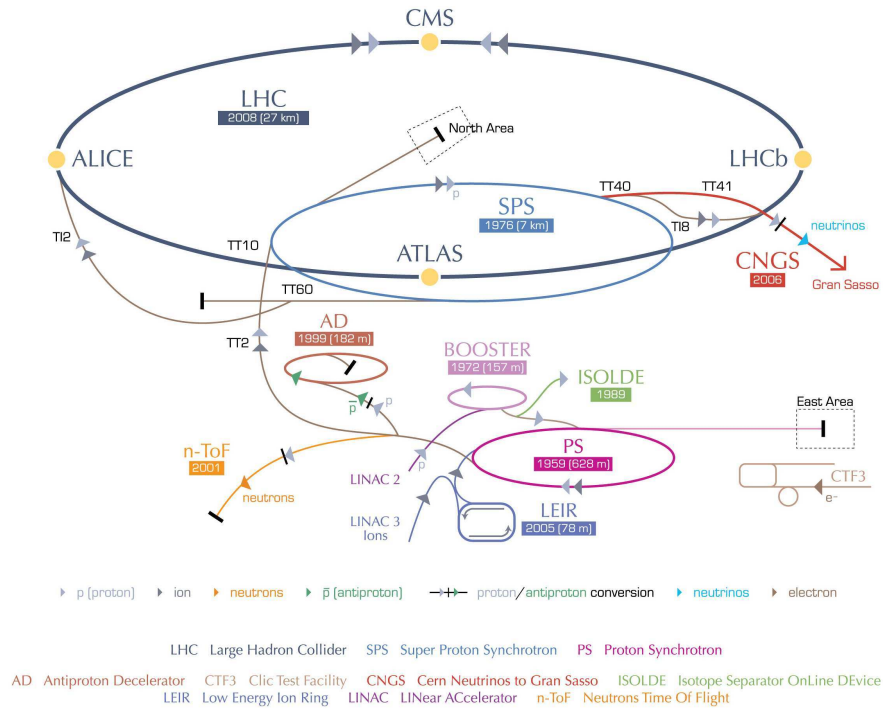

Figure 3.2: The CERN accelerator complex. COMPASS is located in the North Area (figure taken from [31]).

The protons extracted from the SPS then collide with the Beryllium production target *T6*. The thickness of this target can be varied between $40\,\text{mm}$ and $500\,\text{mm}$, and determines the intensity of the resulting secondary beam, which consists mainly of pions, with just a small (amounting to a few percent) contamination of kaons and protons. The produced hadrons, now travelling along the M2 beam line are selected by their momentum via a number of bending magnets and collimators and sent through a $600\,\text{m}$ long beam tunnel, where approximately $10\,\%$ of the pions and kaons decay via weak interaction into positive muons and muon neutrinos. Subsequently the produced muons are focused and the remaining hadrons are filtered out with Beryllium absorbers. The muon beam is then momentum selected by magnets and directed to the surface level. Muon momenta up to $280\,\text{GeV}$ can be chosen; COMPASS runs with $160\,\text{GeV}$ μ^+ beam with a momentum

spread of approximately 5%. Before entering the COMPASS experimental hall the momentum of every beam muon is measured with the Beam Momentum Station (BMS), a set of scintillator hodoscopes placed before and behind the last vertical bending magnet. Approximately 2×10^8 muons per spill cross the target area, resulting in about 6×10^4 recorded interactions per spill.

3.1.2   Beam Properties

The properties of the muon beam are determined by the production mechanism described above. Especially interesting for the COMPAS experiment are the polarisation and the phase space properties of the beam.

Due to the parity violating weak decay $\pi^+ \rightarrow \mu^+ \nu_\mu$ the muons are naturally polarised along the direction of their momentum. In the pion center-of-mass frame the muons are polarised completely. In the lab frame their polarisation depends on the fraction of pion momentum transferred to the muon. In 2004 it was found to be in average $P_B = 0.80 \pm 0.04$ [32].

Compared to primary particle beams the phase space volume of a muon beam is very large. The reasons for this lie in its tertiary nature and the penetration capability of the muons, which make beam collimation difficult.
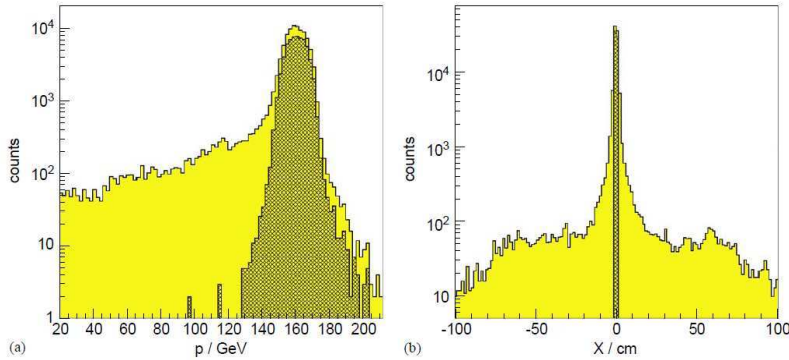

Figure 3.3: (a) Momentum distribution and (b) horizontal profile at the target centre for incoming particles obtained with a random trigger. The shaded areas correspond to particles passing through both target cells [33].

The beam is focussed at the target to a sigma of $7\,\mathrm{mm}$ for the Gaussian core with a momentum spread of $\sigma_p/p \approx 5\%$. Figure 3.3 (a) shows the momentum distribution for incoming muons for a sample of events; Fig. 3.3 (b) shows the spatial distribution at the target centre for the same events. The non-Gaussian tail outside the core is called 'near halo' and amounts to approximately 30% of the core intensity. At larger distances from the beam lower energy muons contribute as well; this is called 'outer halo' [33].

3.2 The Polarised Target

Measuring double spin asymmetries requires a polarised muon beam and a polarised target, as well as the relative spin orientation of both to be invertible. Since the orientation of the muon beam polarisation is fixed, the COMPASS experiment uses a target with a variable polarisation.
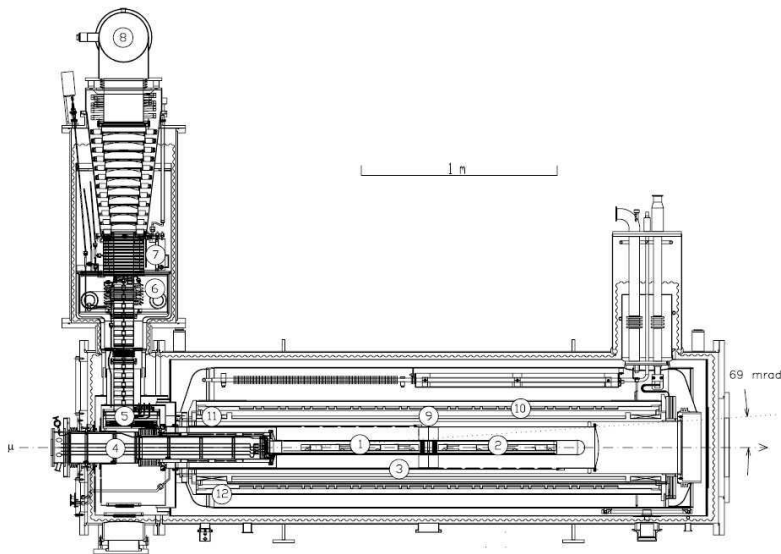

Figure 3.4: Technical drawing of the polarised target. Upstream (1) and downstream (2) target cell, microwave cavity (3), target holder (4), ^{3}He/^{4}He refrigerator (5-8), solenoid coil (9), compensation coil (10-11), dipole coil (12).

The COMPASS target system includes three main components: target cells, magnets (solenoid and dipole), and cryostat.

The centre of the target system consists of two cylindrical cells containing the target material, either lithium deuterit (^{6}LiD, deuteron target) or ammonium (NH$_3$, proton target). The use of a massive target allows for higher luminosities. Each target cell is 60 cm long and has a diameter of 4 cm. The target material in the cells is polarised in opposite direction. This allows a simultaneous measurement of both spin states and, together with a periodic polarisation reversal, is aimed to significantly reduce systematic effects.

The target cells reside in a homogenous, longitudinal magnetic field, generated by a super conductive solenoid. Cells and solenoid are enclosed in a ^{3}He/^{4}He dilution refrigerator which allows the cooling of the target material down to 60 mK. The low temperature and the strong solenoid field provide the means to polarise the target material, to increase the relaxation time and therefore to maintain its polarisation as long as possible.

The polarisation itself is achieved by dynamic nuclear polarisation, transferring polarisation from the electrons to the nucleons [34].

At a temperature of $60\,\text{mK}$ and a magnetic field of $2.5\,\text{T}$ almost $100\,\%$ of the electrons are polarised, but only about $0.5\,\%$ of the protons. Using microwaves of a suitable frequency, the polarisation of the electrons can be transferred to the protons of the target material. Once the proton spins are aligned the temperature is kept at $60\,\text{mK}$ to maintain the polarisation. Solenoid and dipole magnetic fields allow to adjust the spins in a longitudinal or transversal direction. Each target cell contains five NMR coils used for the local monitoring of the polarisation. To compensate for possible differences in acceptance and amount of target material in the cells the magnetic field, and consequently the spin orientation, is rotated every 24 hours.

The COMPASS target was upgraded for the 2006 run. The two target cells were replaced by three. Additionally a new solenoid was used, with a larger opening angle, and consequently a larger acceptance for hadrons.

3.3   Tracking Detectors

The COMPASS spectrometer with its large overall acceptance uses a variety of tracking detectors to measure the projections of the particle tracks on the bending (X) or the non-bending (Y) plane of the spectrometer magnets. The requirements for a particular detector are dictated by its proximity to the beam. Tracking stations near the beam axis are exposed to a higher particle flux, which makes a good time and spatial resolution a main requirement. Stations which are farther away from the beam core are exposed to a lower particle rate, which allows for a lower resolution. The main requirement for those detectors is the ability to detect particles scattered with large angles, demanding the coverage of a large area.

3.3.1   Small Area Trackers

Scintillating Fibre Detectors (SciFis): Particle tracks in the primary beam are identified by scintillating fibres (SciFis) [35] [36]. The COMPASS spectrometer contains eight SciFi stations. Each consists of two to three different layers of scintillating wires rotated with respect to each other to measure more than one projection. The individual layers themselves are composed of a number of parallel fibres with a diameter between 0.5 and $1\,\text{mm}$, resulting in a spatial resolution of 130 to $250\,\mu\text{m}$. The SciFi detectors cover areas from $40\,\text{mm} \times 40\,\text{mm}$ (in front of the target) up to $123\,\text{mm} \times 123\,\text{mm}$ (farther downstream), their time resolution ranges between 350 and $500\,\text{ps}$. They are read out via optical fibres and photomultiplier tubes. The hodoscopes cover approximately $90\,\%$ of the beam.

Silicon Microstrip Detectors: The COMPASS silicon detectors are semiconductor strip detectors with pn junctions. Each covers an active area of $5 \times 7\,\text{cm}^2$, with a pitch of $50\,\mu\text{m}$. Two nearly orthogonal readout structures are used to obtain two projections simultaneously. Two detectors make up one silicon station. They are mounted back-to-back such

that one detector measures the horizontal and vertical coordinates of a particle trajectory, while the other is rotated around the beam axis by 5°, providing two additional projections. The silicons are only 280 μm thick, due to the high average energy loss of typically 390 eV/μm, and also to minimise Coulomb scattering, which would reduce the resolution. An advantage over gas detectors is the low energy threshold of 3.6 eV for the generation of an electron/hole pair. The silicon detectors have an average spatial resolution of about 11 μm due to their small pitch, and a time resolution of 2.5 ns. They are positioned in front of the target; together with the first two scintillating fibre stations they provide a precise beam definition.

Microstrip Gas Detectors: Two different types of microstrip gas detectors cover the zone outside the beam core up to a distance of the beam axis of approximately 45 mm; a region with a high rate of halo muons and hadrons produced in the interactions in the target. Micromesh gas chambers, short **Micromegas**, are used as small area trackers between the target and the first spectrometer magnet SM1. The special feature of this detector is the presence of a metallic micromesh which separates the gaseous volume into two regions; one for conversion and one for amplification. The field configuration near the mesh provides a barrier that ensures that most of the ions from the avalanche are captured by the mesh and do not drift back in the conversation gap. The fast evacuation of the positively charged ions in combination with reduced transverse diffusion of the electrons enable a high rate capability of the micromegas. The detector has an active area of 40 × 40 cm^2 and a central dead zone of 2.5 cm radius. The strip pitch is 360 μm for the central part of the detector and 420 μm for the outer part. The Micromegas have a time resolution of 9 ns and spatial resolution of 90 μm [1].

A **GEM** detector consists of a 50 μm thin Polyamide foil with copper cladding on both sides, into which a large number of micro-holes (about 10^4/cm^2, 35 μm radius) has been chemically etched. The foil is inserted between parallel plate electrodes of a chamber filled with a mixture of argon and carbon dioxide. Avalanche multiplication of primary electrons drifting into the holes is achieved by applying a voltage of several 100 V across the foil. Electric fields extract the electrons from the holes on the other side of the foil and guide them to the next amplification stage or to the readout module. The detector is read out in two layers simultaneously. Two of these planes form a station giving four projections in total. Each of the seven GEM stations located throughout the length of the spectrometer has an active area of 32 cm × 32 cm. A central disc with a 2.5 cm radius is independently powered in order to enable a switching off of the region during high intensity runs. The spatial resolution for minimal ionising particles is on average 46 μm, the time resolution amounts to 12 ns.

3.3.2 Large Area Trackers

Drift Chambers: Three identical drift chambers are in operation at COMPASS. One is installed upstream of the spectrometer magnet SM1, the other two downstream of it. All three drift chambers have an active area of 180 cm × 127 cm. Each chamber consists of eight layers of wires with four different inclinations: vertical, horizontal, and tilted with

respect to the vertical direction, by $\pm 20°$ [1]. Each layer consists of approximately 350 wires, half of them sensitive, half of them potential, alternating. Each layer is enclosed by two Mylar cathode foils, defining a gas gap of 8 mm. The chambers are segmented into small drift cells of 8 mm $\times$ 7 mm, giving the advantage of decreasing the incident flux per cell and reducing the electron drift time (thus allowing for a short time window and minimising the number of uncorrelated particles). The $Ar/C_2H_6/CF_4$ gas mixture ensures a high primary electron rate as well as a high drift velocity (77 mm/μs). The resolution of the drift chambers is 110 μm for the horizontal coordinate (bending direction of the dipole spectrometer magnet) and 170 μm for the vertical coordinate.

Straw Tube Chambers: Straw drift tube chambers are used to track charged particles at large scattering angles downstream of the first spectrometer magnet SM1. The 30 μm diameter anode wires are encased in tubes consisting of two thin layers of Kapton foil. The straws are arranged in double layers, which are displaced by half a diameter with respect to each other to resolve left-right ambiguities. The length of the straw tubes increases with humidity, which can result in increased tension on the frame or even in a bending of the straws. To avoid these problems, each straw station is surrounded by a protective gas volume of N_2 gas, enclosed in aluminised Mylar foil. The COMPASS spectrometer is equipped with 15 straw detectors, consisting of more than 12,000 straw tubes in total. Each detector has an active area of about 9 m^2. The counting gas mixture is $Ar/C_2H_6/CF_4$. To allow for the measuring of three projections of the particle trajectory, each station consists of three detectors, with horizontal, vertical, and inclined layers of straw tubes. The average spatial resolution of the straw detectors is 190 μm.

Multi-wire Proportional Chambers: Multi-wire proportional chambers (MWPCs) are wire chambers with a large number of readout wires. They are used throughout the whole spectrometer; the tracking of particles at large distances from the beam axis is based mainly on these detectors. Three chambers are positioned between the spectrometer magnets SM1 and SM2, four behind SM2, and another four behind the second muon wall, MW2. A total of 34 layers of wire, corresponding to about 25,000 detector channels is in operation at COMPASS. All layers are equipped with wires of about 1 m in length, 20 μm in diameter, with a pitch of 2 mm and an anode/cathode gap of 8 mm. A fast gas mixture $(Ar/C_2/CF_4/Co_2)$ results in a drift velocity of approximately 100 μm/ns. Three different types of MWPCs are in use, each with an active area of up to 178 cm $\times$ 120 cm, and two to four layers of wires, allowing for a spatial resolution of 1.6 mm. All MWPCs have a central dead zone of 16 to 22 mm diameter, depending on the position of the detector along the beam axis. All wire layers are enclosed by graphite coated Mylar cathode foils, which provide field symmetry and encase the detector gas.

3.4   Particle Identification

Both stages of the COMPASS spectrometer include various detectors to ensure an efficient particle identification. A RICH detector in the LAS separates outgoing hadrons into pions,

kaons and protons. Two hadron calorimeters (HCAL1 and HCAL2) measure the energy of hadrons and provide also a corresponding trigger signal. The electromagnetic calorimeter in the SAS (ECAL2) determines the energies of photons and electrons. Muons are detected in two muon wall systems MW1 and MW2, which consist of medium resolution tracking detectors combined with a hadron absorber.

3.4.1 The Ring Imaging Cherenkov Detector (RICH)

The COMPASS RICH (see Fig. 3.5) plays a crucial role in the identification of pions, kaons and protons within a momentum range of 5 and $43\,\mathrm{GeV/c}$. The large-size Ring Imaging Cherenkov detector covers the whole angular acceptance of the COMPASS LAS ($\pm 250\,\mathrm{mrad}$ in the horizontal plane and $\pm 180\,\mathrm{mrad}$ in the vertical plane), has a high-rate capability and introduces a minimum of material in the region of acceptance.
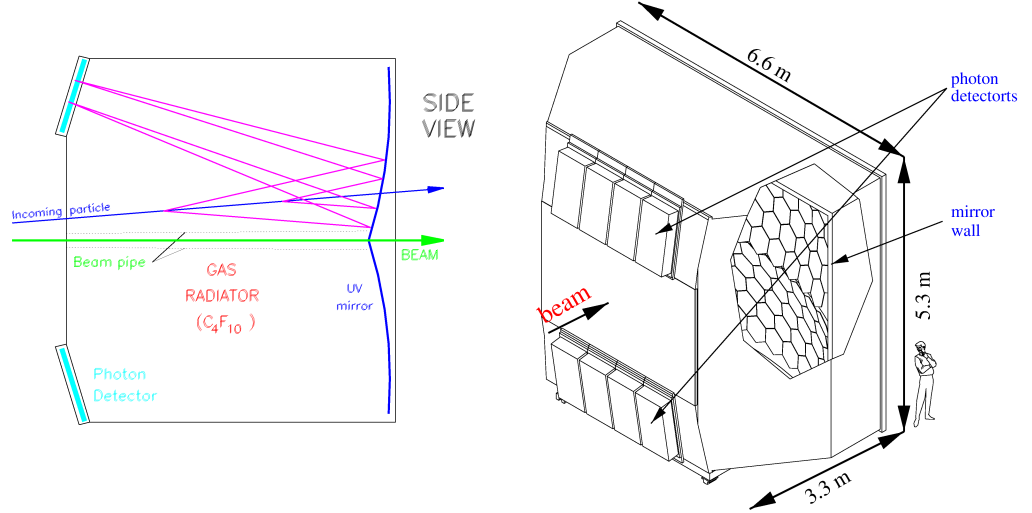

Figure 3.5: Schematic view of the COMPASS RICH [37]

The RICH detector makes use of the phenomenon that charged particles emit Cherenkov radiation if their velocity is larger than the speed of light in the medium in which they advance. The photons are emitted with a characteristic angle θ_{ch} relative to the direction of the travelling particle:

$$\cos\theta_{ch} = \frac{1}{n\beta} = \frac{1}{n}\frac{1}{\sqrt{1 + \frac{m^2}{p^2}}}. \tag{3.1}$$

Therefore, by measuring θ_{ch} with the RICH and the momentum of the particle with the spectrometer, the mass of the particle, and consequently its type, can be determined. The threshold momentum p_{thr} for which Cerenkov photons are emitted follows from Eq. 3.1:

$$p_{thr} = \frac{m}{\sqrt{n^2 - 1}} \tag{3.2}$$

For β approaching 1 the angle θ_{ch} reaches its maximum. Consequently, each particle type can be distinguished from lighter particles only up to a certain momentum. For example pions with momenta larger than $8\,\mathrm{GeV/c}$ cannot be distinguished from electrons anymore (which emit Cherenkov photons always with the maximum angle).

The radiator gas used in the RICH is C_4F_{10}. It is characterised by a low chromaticity despite its high refractive index of $n \approx 1.0015$ in the UV domain [38], which allows for a separation between pions and kaons up to a momentum of $43\,\mathrm{GeV/c}$. Water vapour and oxygen contaminations of the C_4F_{10} radiator gas impair the light transmission in the UV range due to their large UV light absorption cross section. To combat this problem the gas is continuously circulated in a closed loop circuit in order to remove the traces of water vapour and oxygen. The Cherenkov thresholds for different particles are listed in Table 3.1.

Particle	Threshold in GeV/c
e	0
μ	1.9
π	2.5
K	8.9
p	16.9

Table 3.1: Cherenkov thresholds for different particle types of the COMPASS RICH [39]

The optical system consists of two spherical focal surfaces with a radius of $6.6\,\mathrm{m}$, each composed of 58 spherical mirror units in different sizes, in the form of hexagons and pentagons. The focal surfaces cover an area of $21\,\mathrm{m}^2$. They are placed outside the spectrometer acceptance to minimise the material in the detection region. The mirror substrate is a glass of $7\,\mathrm{mm}$ thickness covered by an $80\,\mathrm{nm}$ reflective layer of aluminium and $30\,\mathrm{nm}$ protective layer of $\mathrm{MgF_2}$. The reflectance of the optical system was measured in the wavelength range $[165\,\mathrm{nm},\,200\,\mathrm{nm}]$ and found to be in the range 83-87%. The photon detection is ensured by eight multiwire proportionl chambers (MWPC) (cf. Section 3.3.2), which are read out by front-end boards coupled with amplifier chips.

The RICH operated with this system until 2004. For the 2006 data taking, an important upgrade has been implemented in order to improve its performance. In the very central region of the RICH, the MWPC chambers were replaced by a new photon detection system based on Multi-Anode Photo Multiplier Tubes (MAPMT), increasing thereby the number of detected Cherenkov photons which, in turn, increased the momentum range of identified particles. The separation of pions and kaon is possible up to $50\,\mathrm{GeV/c}$ with the new system compared to $43\,\mathrm{GeV/C}$ for the old one.

3.4.2 Electromagnetic and Hadronic Calorimeters

Both stages of the spectrometer contain calorimeters at the downstream end. The purpose of the electromagnetic calorimeter is to detect neutral particles, e.g the two photons from a π^0 decay, and to identify electrons. The hadronic calorimeters measure hadron energies and can also be used to identify muons, which deposit a characteristic small amount of energy. The hadronic calorimeters are included in the trigger (cf. Section 3.5.2), allowing to trigger on events with hadrons in the final state.

3.4.2.1 The Electromagnetic Calorimeters

The COMPASS spectrometer features an electromagnetic calorimeter (ECAL2) in the SAS. A second one (ECAL1) was put in operation in the LAS in 2006.

The ECAL2 is a homogenous calorimeter and consists of 2972 lead glass modules in a matrix of 64×48, measuring $38 \times 38 \times 450\,\text{mm}^3$ each, corresponding to 16 radiation lengths. A high energy photon or electron generates an electromagnetic shower in the lead glass; the produced electrons and positrons emit Cherenkov light on their way through the glass. The amount of light is proportional to the energy deposited in the counter. Every lead glass unit is read out at one end via a photomultiplier tube which measures the intensity of the light emitted.

The modules are installed inside a movable frame which can be shifted horizontally and vertically to the beam axis. Additionally the ECAL2 frame is mounted on a platform which can be moved on rails along the beam axis. An opening of 10×10 modules in the centre of the calorimeter allows the passage of the beam particles. Two different kinds of lead glass are used for the ECAL2 modules, TF1 and TF101 (radiation hardened by the addition of 0,2% Cerium). The radiation hard modules are arranged around the beam opening in the centre of the calorimeter.

3.4.2.2 The Hadron Calorimeters

The COMPASS spectrometer contains two hadron calorimeters, HCAL1 (in the LAS) and HCAL2 (in the SAS).

HCAL1 has a modular structure. Each module consists of 40 layers of iron and plastic scintillator plates, 20 mm and 5 mm thick, respectively, amounting to 4.8 nuclear interaction lengths. The incoming hadrons generate a shower in the iron layer; the produced shower particles generate light in the subsequent scintillator layer. The sum of the light signals from the scintillator layers is proportional to the energy deposited in the module. The light from the scintillators is collected by a single flat wavelength shifting light guide placed on the open sides of the scintillators. The amount of light emitted and collected from the scintillator layers is read out via PMT. The 480 calorimeter modules are assembled within a frame in form of a matrix of 28×20 (horizontal $\times$ vertical). A window of 8×4 modules

in the centre of the calorimeter allows the passage of the beam and scattered muons. The active area of the HCAL1 amounts to $10.8\,\mathrm{m}^2$. The calorimeter frame is mounted on a platform that can be moved across the beam axis.

The HCAL2 calorimeter has the form of a 22×20 matrix. Similar to the HCAL1 set-up the modules are arranged on a mobile platform. The calorimeter has a hole with the dimensions of 2×2 modules to pass the high intensity beam. Two different types of modules are used for the detector. The majority of them consist of 36 layers of steel ($25\,\mathrm{mm}$) and scintillator ($5\,\mathrm{mm}$) plates. The overall thickness of the counters corresponds to 5.0 nuclear interaction lengths for pions and seven for protons. The 8×6 cells in the centre (around the beam window) are filled with thicker modules consisting of 40 layers. The principle of light collection is similar to the one used for the HCAL1 modules. Instead of flat light guides placed on the sides of the modules the HCAL2 modules contain wavelength shifting fibres of $1\,\mathrm{mm}$ diameter placed in a circular groove in each scintillator sheet. The bundle of fibres from all sheets of one module collects the light onto the photocathode of a PMT.

Table 3.2 contains a summary of the technical data of both COMPASS HCALs.

	HCAL1	HCAL2
module size	$15\,\mathrm{cm} \times 15\,\mathrm{cm}$	$20\,\mathrm{cm} \times 20\,\mathrm{cm}$
number of modules	480	216
calorimeter size	$429\,\mathrm{cm} \times 306\,\mathrm{cm}$	$440\,\mathrm{cm} \times 200\,\mathrm{cm}$
layers per modul	40	36
thickness of iron/scintillator	$20\,\mathrm{mm}/5\,\mathrm{mm}$	$25\,\mathrm{mm}/3\,\mathrm{mm}$
radiation length	$46\ X_0$	$51\ X_0$
interaction length	$4.8\ \lambda_i$	$5.4\ \lambda_i$
maximum hadron energy	$80\,\mathrm{GeV}$	$230\,\mathrm{GeV}$
read-out	WLS light guides	WLS fibres
energy resolution	$\frac{60\%}{\sqrt{E[GeV]}} + 7,6\%$	$\frac{65\%}{\sqrt{E[GeV]}} + 5\%$

Table 3.2: Summary of the technical data of HCAL1 and HCAL2. Maximum hadron energy stands here for the energy limit above which 95% of the shower length is larger than the length of the calorimeter modules. [40] [41]

3.4.3   Muon Filters

At the very end of the LAS and of the SAS (behind the hadronic calorimeters) absorbers are placed, consisting of iron and concrete, respectively (μF_1 and μF_2). These absorbers serve to filter out all non-muon particles, such as high energetic pions which are not stopped in the hadronic calorimeter. The absorber at the end of the LAS has an opening around the beam axis to allow particles produced under small angles to enter the SAS.

Large area trackers are installed upstream and downstream of both absorbers, permitting reliable muon identification, in particular of the scattered muon, which is essential for the reconstruction of the DIS variables.

3.5 The Trigger System

The muon beam has an intensity of approximately 2×10^8 muons per spill (cf. Section 3.1) and a considerable halo component. The rate of useful scattering events is about 10^4 per spill. The purpose of the trigger system is to identify these events with a decision time below 500 ns and a minimum deadtime, in order to start the detector readout system and to provide a time reference for other detectors. The system is based on fast hodoscope signals, energy deposits in the calorimeters, and a veto system. Depending on the incident beam - muons or hadrons - and on the kinematics of the reactions, different elements are combined to form the trigger signal. In the following the muon triggers are described in detail; for the hadron triggers consult [1].
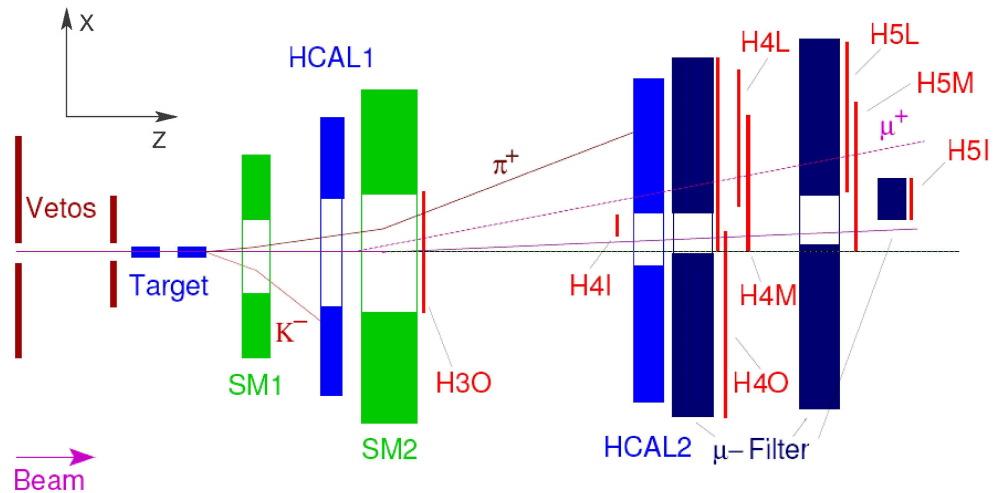
Figure 3.6: Position of the trigger components in the COMPASS spectrometer, pictured for the bending plane of the spectrometer magnets. There are in total four trigger hodoscope subsystems: H4I & H5I, H4M & H5M, H4L & H5L and H3O & H4O. The veto detectors (dark red) are positioned in front of the target. The electromagnetic and hadron calorimeters are pictured in blue, the spectrometer magnets SM1 and SM2 in green [40]

.

For the COMPASS muon programme two types of processes are of interest: quasi-real photoproduction and deep-inelastic scattering. Both have a muon in the final state in common. Therefore it is reasonable to base the trigger decision on the detection of the scattered muon, in particular because muons can be easily identified by hits in detectors

located behind the hadron absorber. At COMPASS pairs of scintillator hodoscopes are used, with at least one of the two hodoscopes placed behind the hadron absorber to identify the scattered muon.

There are four different hodoscope subsystems in total: H4I & H5I ('Inner'), H4M & H5M ('Middle'), H4L & H5L ('Ladder') and H3O & H4O ('Outer')[2]. Each of these systems possesses a granularity allowing to select muons pointing back to the target region in the non-bending plane of the spectrometer magnets, or to select muons with an energy loss beyond a certain minimum in the bending plane.

The trigger decision cannot be based on the scattered muon alone. Due to the large amount of halo muons surrounding the beam core trigger signals are generated in the hodoscope pairs even if the muons have not traversed the target cells or have not interacted with the target nucleons. These unwanted signals can be eliminated by placing additional veto hodoscopes in front of the target and demanding that no signal was present. A second possibility for reducing the contribution from trigger signals caused by halo events is to demand, in addition to the hodoscope signal, a signal above a certain threshold in the hadron calorimeters.

The location of these three main components of the COMPASS trigger system - hodoscope subsystems, veto detectors, calorimeters - are shown in a schematical view in Fig. 3.6.

3.5.1 The Muon Trigger

As already mentioned in the introduction, two kinematic regimes are of interest for the COMPASS muon programme:

- deep-inelastic scattering ($Q^2 \gtrsim 0.5 \, \text{GeV}^2/\text{c}^2$)
  for the measurement of spin asymmetries (cf. Chapters 2 and 4) and the hadron multiplicities (cf. Chapter 5) used in this thesis

- quasi-real photoproduction ($Q^2 \lesssim 0.5 \, \text{GeV}^2/\text{c}^2$)
  for the determination of the helicity contribution of the gluons, ΔG

The DIS events can be identified by detecting muon tracks pointing back to the target. The small four-momentum transfer in quasi-real photoproduction though results in scattering angles that are too small to allow this kind of 'target pointing'. In this case the energy loss of the scattered muon is used to select the relevant events. The muon triggers identifying these signatures are the trigger for $Q^2 \gtrsim 0.5 \, \text{GeV}^2/\text{c}^2$ and the energy-loss trigger. They will be described in detail in the following sections.

---

[2]The numbers assigned to the hodoscope subsystems (and other detectors) have historical reasons. They used to mark the distance from the target along the beam axis. The lower-numbered detectors closer to the target area were not part of the COMPASS apparatus anymore in 2004.

3.5.1.1 The Energy-Loss Trigger

Quasi-real photoproduction is characterised by a very small four-momentum transfer ($Q^2 \approx 0$), which corresponds to a small muon scattering angle. At the same time a large energy transfer y is necessary to ensure a sufficient photon polarisation. As a consequence only events with an energy transfer y above a certain minimum - and in turn, an energy-loss of the scattered muon beyond a certain limit - are of interest.
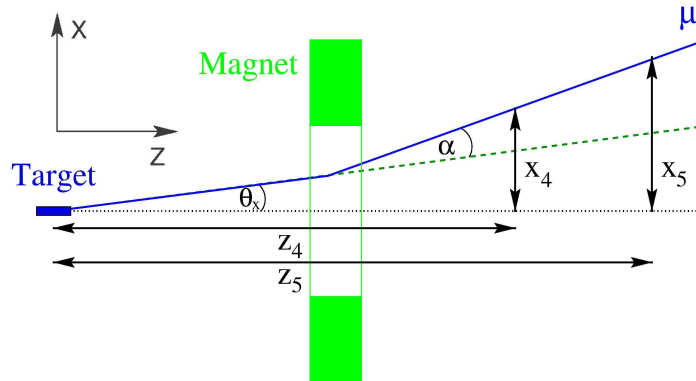

Figure 3.7: The muon energy is determined by measuring the deflection of the particles in two different places (x_4 and x_5) along the beam axis. The two spectrometer magnets are represented by one 'effective magnet' in this drawing [1].

The muon energy is determined by the deflection in the field of the spectrometer magnets (cf. Fig. 3.7). Because the muons already enter the field at an angle θ due to their interaction with the target nucleons a simple measurement of their distance to the beam axis in the bending plane (X-coordinate) is not sufficient. The solution is the combination of two measurements. The X-coordinate of the muon track is determined twice along the beam axis (Z-coordinate).
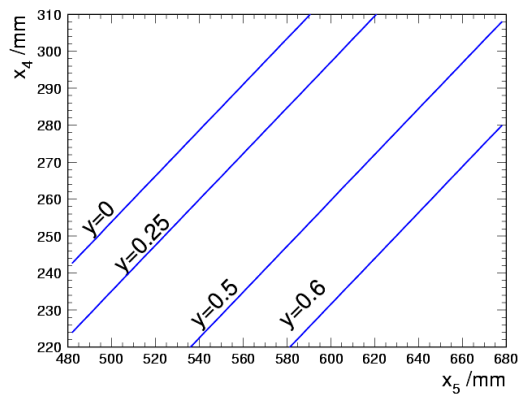
Figure 3.8: Lines of constant energy-loss in the x_4-x_5 plane (cf. Fig. 3.7) [40].

This method allows the determination of the muon scattering angle θ, projected on the

bending plane, as well as the deflection due to the field of the spectrometer magnets (α) [40]. Figure 3.8 shows lines of constant energy-loss in the x_4-x_5 plane.

A trigger decision within 500 ns necessitates the use of detectors with a fast response. Additionally the short time frame only allows for basic signal processing. The COMPASS trigger system uses a coincidence measurement. Two X-coordinates and their respective times are measured. Plastic scintillators offer a good time resolution and are used for this reason in this part of the trigger. The scintillators are read-out via photomultiplier tubes. The response time of such a scintillator detector is determined by its respective components and usually amounts to 30 ns. The time resolution of these detectors is approximately 1 ns.

The energy-loss trigger is based on pairs of scintillators in two different hodoscopes of a hodoscope subsystem. The subsystems used for the energy-loss trigger are 'Inner', 'Middle' and 'Ladder'. Each of the hodoscopes consists of up to 32 scintillators, placed perpendicular to the bending plane of the beam. Each pair of scintillators (x_4, x_5) in the two hodoscopes corresponds to a combination of scattering angle projection (θ_x) and energy-loss (y).
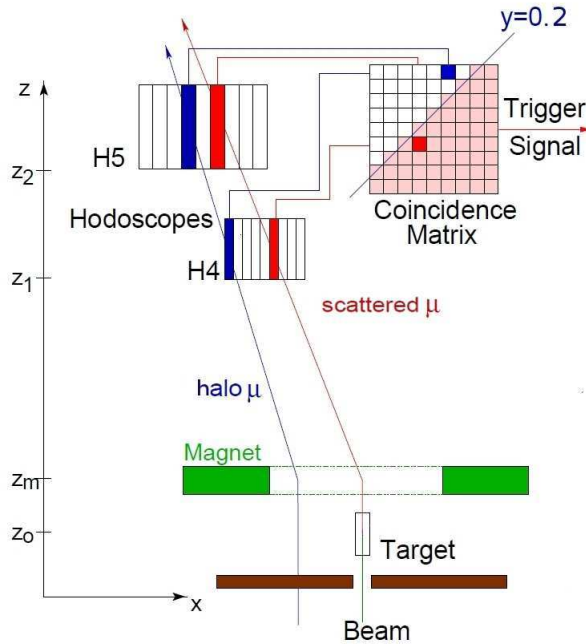
Figure 3.9: Principle of the energy-loss trigger. A muon scattered at a small angle is deflected in the magnetic field of the spectrometer magnets according to its energy-loss y. It triggers a coincidence in the active area of the matrix (and in turn a trigger signal), while coincidences triggered by halo muons are ignored [33].

The two scintillator signals of a pair are linked by a coincidence logic; for all combinations (x_4, x_5) satisfying the condition $y(x_4, x_5) \geq y_{min}$, and therefore indicating an energy-loss of the muon larger than y_{min}, a trigger signal is generated.

The so-called coincidence matrix constitutes the salient part of this electronic system. The matrix consists of 32 rows and columns, corresponding to the number of scintillators in the hodoscopes H4 and H5, and allows to select the coincidence of every possible combination of scintillator signals. Each of those coincidences (up to $32 \times 32 = 1024$) can be activated and deactivated independently.

Figure 3.9 shows the principle of the energy-loss trigger. Two different muon tracks are indicated; both muons generate signals in the hodoscopes and coincidences in the matrix. The scattered muon, due to its larger energy-loss, is deflected more strongly in the magnetic field than a beam or halo muon. Both generate signals in different areas of the coincidence matrix. Areas indicating an energy-loss of less than 20% are deactivated. The borderline between activated and deactivated areas of the matrix is the line of the constant energy-loss $y = 0.2$. The active area (lower right) corresponds to larger energy-losses, the inactive area (upper left) to smaller energy-losses. Therefore, only muons with an energy-loss of at least $y = 0.2$ generate a trigger signal.

3.5.1.2 The Trigger for $Q^2 \gtrsim 0.5 \text{ GeV}^2/\text{c}^2$

This part of the trigger system selects deep-inelastic scattering events with a momentum transfer of $Q^2_{min} \approx 0.5 \text{ GeV}^2/\text{c}^2$ up to $Q^2 \approx 50 \text{ GeV}^2/\text{c}^2$ and covers energy-losses of $0.1 \leq y \leq 0.9$. The hodoscope system distinguishes scattered muons and halo muons by ensuring that the muon passed through the target. This trigger is designed for large scattering angles and determines the position of the scattered muon in the plane perpendicular to the deflection plane of the spectrometer magnets (*Y*-plane). Due to its principle of operation it is also called the geometrical trigger.
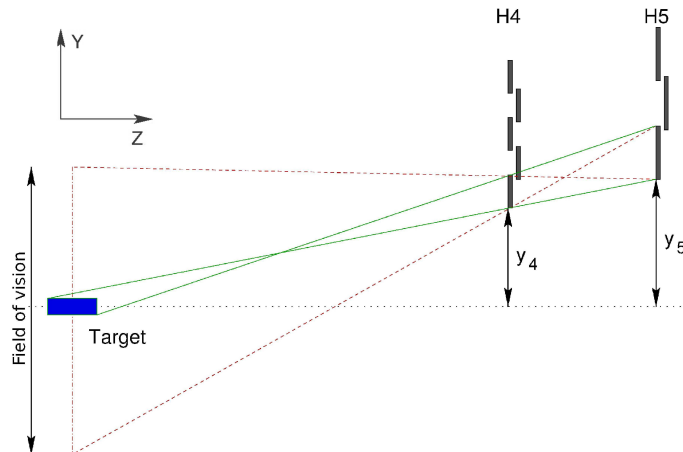
Figure 3.10: Principle of the geometrical trigger. The place of origin of the muon is determined via selection of scintillator pairs [1]. The dotted lines mark the 'visual field' of the trigger, the volume the trigger cannot discern from the target volume.

Basis of this trigger are again pairs of scintillators in two hodoscope subsystems; the 'Middle' and 'Outer' systems. The scintillators are arranged horizontally in this case, parallel to the deflection plane of the spectrometer magnets. A coincidence logic similar to the one used for the energy-loss trigger ensures that only muons pointing back to the target generate a trigger signal.

Figure 3.10 shows the lateral view of the layout. The dotted lines mark the 'visual field' of the trigger, the volume the trigger cannot discern from the target volume. The extent of this volume depends strongly on the width of the scintillator strips.

3.5.2   The Calorimeter Trigger

Basing the trigger decision on the scattered muon alone in the whole kinematic range allows for contamination with certain background processes. A pure energy-loss trigger does not discern between low-energy muons from processes relevant for the determination of ΔG and low-energy muons from other processes. Resulting in an energy-loss of the same magnitude are:

- Low-energy beam particles
  The beam momentum spectrum is normally distributed around its nominal value. The 1σ-width of this distribution is $7\,\mathrm{GeV}$ or 4.4%. Accordingly, a large number of beam muons are misidentified, especially for a small energy-loss y. This number decreases strongly with increasing energy-loss.

- Elastic muon-electron scattering: $\mu + e^- \to \mu' + e^-$
  The cross section for this process increases for small y with $1/y^2$.

- Radiative events: $\mu + N \to \mu' + N + \gamma$
  The cross section for internal bremsstrahlung depends strongly on the atomic number Z of a particular material and increases for small energy-loss.

The background sources listed above have one similarity; they result in an energy-loss for the muon, but - unlike DIS events - do not produce a hadron. Therefore, an additional hadron detection allows the suppression of these processes in the trigger.

This hadron trigger is based on the hadronic calorimeters HCAL1 and HCAL2. The trigger system uses their approximately 700 calorimeter modules to generate a signal for every hadron with a minimum energy.

The high-energy hadron showers usually extend a single calorimeter module. As a consequence the signals of several adjacent cells have to be added up to determine the deposited energy of a single hadron. 4×4 calorimeter modules are combined to one block. Hadrons hitting the edge of one of those blocks distribute their energy among two or four blocks, which necessitates four different layers of summation to guarantee that at least 85% of the hadron's energy is deposited in one block.

The summation of the signals is achieved in two steps (cf. Fig. 3.11). In a first step the PMT signal is split to supply both the calorimeter read-out and the trigger logic. The signal copies for the trigger logic are combined in groups of 2×2, and fed into the second summation step. They are again duplicated and combined to blocks of 4×4. Each of these signals is evaluated by a constant fraction discriminator, and a logical OR of the discriminator outputs is computed. Every signal above a certain threshold is included in the trigger coincidence.
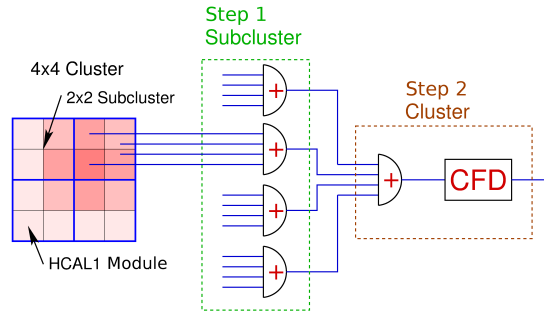
Figure 3.11: Sketch of the summation logic of the calorimeter trigger. 16 calorimeter modules are grouped into four blocks. In a second step the signals are added up into blocks of 16. The different colours indicate the amount of deposited energy per block [40].

The beam halo exposes the hadron calorimeters to a high muon flux. HCAL2 with its relatively small beam opening is especially vulnerable; it is traversed by several million muons per spill. Sufficiently suppressing the muon signals is therefore essential for an efficient use of the trigger. This is achieved via reasonable energy thresholds for the hadrons.
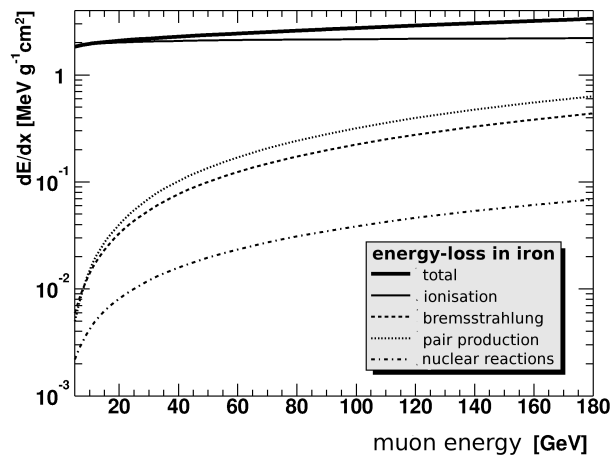
Figure 3.12: Average energy-loss for muons in iron as a function of the muon energy [40].

Figure 3.12 shows the average energy-loss of muons in iron [42]. The most important energy-loss process is ionisation; for muons with an energy of less that 160 GeV it amounts to 66%. Other significant processes are pair production, bremsstrahlung and nuclear reactions.

The typical energy-loss of a 160 GeV muon traversing iron amounts to approximately $3.2 \, \mathrm{MeV}/(\mathrm{g/cm}^2)$, which corresponds to a probable energy deposition of 2 GeV for HCAL1 and 2.3 GeV for HCAL2.
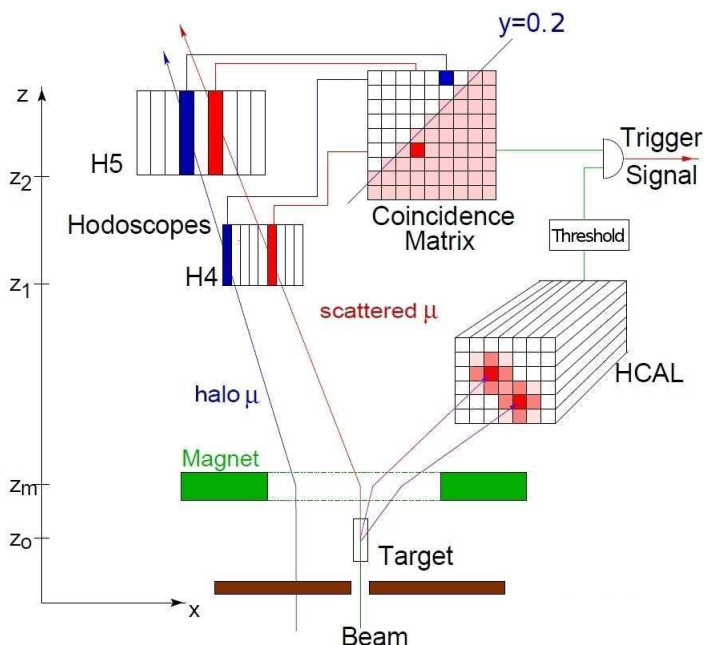
Figure 3.13: Principle of the energy-loss trigger (cf. Fig. 3.9) with the calorimeter trigger included [1].

To successfully suppress the muon signal the energy threshold has to be well above the typical energy-loss of a 160 GeV muon. An energy threshold of twice the value of the average muon energy-loss cuts the muon signal down to approximately 10%, a threshold at three times of that value down to 4%. On the other hand a high energy threshold reduces the efficiency of the calorimeter trigger because low-energy hadrons are disregarded. The COMPASS hadron calorimeter thresholds are typically set between twice and three times of the value of the average muon energy deposition.

Figure 3.13 depicts the principle of the energy-loss trigger, with additional hadron detection from the calorimeters.

3.5.3 The Veto System

The disadvantage of the calorimeter trigger is that it introduces some bias in the selection of inclusive events. The hadron calorimeters for example do have different detection probabilities for positive, negative and neutral hadrons [33]. For the measurement of inclusive asymmetries and hadron multiplicities it is therefore preferable to avoid using the calorimeter trigger information.

On the other hand, a trigger based on a coincidence between two hodoscope planes alone would result in rates of the order of 10^6 per spill, much too high for the data acquisition system to handle. The reason for this is that a considerable fraction of the halo muons cause a trigger signal as well, without interacting in the target. These unwanted coincidences can be rejected by a veto system. It consists of scintillator hodoscopes upstream of the target. Their task is the tagging of all particle tracks within the visual field of the trigger that did not pass through the target. By demanding the absence of a signal in the veto system together with a coincidence in two hodoscope planes an adequate trigger purity can be achieved.
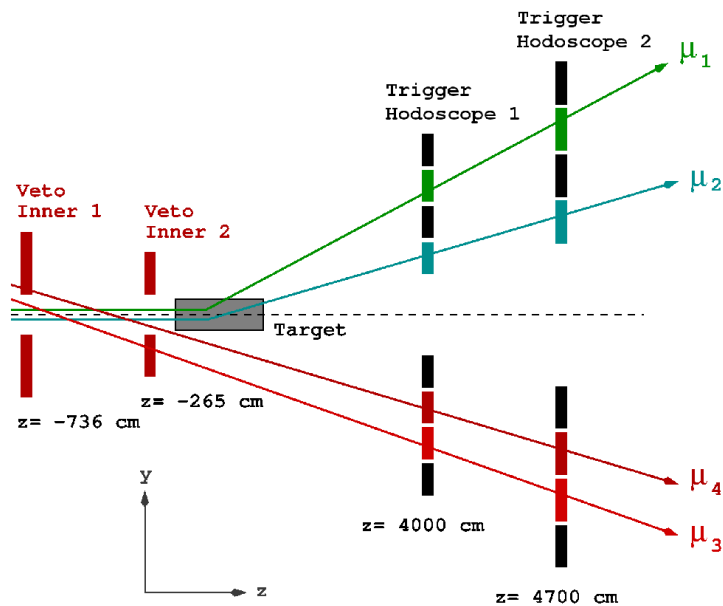
Figure 3.14: Layout of the veto detectors and principle of the veto system. Beam muons traversing the target are marked in blue and green (μ_1 and μ_2). Muons entering the spectrometer at an angle (μ_3 and μ_4 in red) are detected in the trigger hodoscopes even though there was no interaction with the target. These tracks are registered in either one or both of the veto detectors 'Inner 1' and 'Inner 2', and the generation of a trigger signal is suppressed.

Figure 3.14 shows the principle of the veto system and the layout of the detectors used. The system is based on the two veto detectors 'Inner 1' and 'Inner 2', which are located approximately $8\,\mathrm{m}$ and $3\,\mathrm{m}$ in front of the target. The veto counters form a wall of plastic

scintillators with a circular beam window in the centre. The diameter of the window is chosen to ensure exclusively the detection of halo muons missing the target.

The use of two veto detectors allows for the detection of muons entering the spectrometer at an angle to the beam axis. With a hole diameter of approximately 4 cm the system is able to detect all halo particles with an angle larger than 8.5 mrad.

A disadvantage of a veto system like this is the dead time associated with it. A halo muon hitting one of the veto detectors, even if it does not cause an allowed coincidence in the trigger hodoscopes, will prohibit a trigger signal for typically 15 ns. The total rate seen by the veto system in 2004 was approximately 15 MHz, resulting in a dead time of the order of 15 ns × 15 MHz ≈ 23% [32].

3.5.4 The Trigger Hodoscopes

The four different hodoscope subsystems consist of a total of 14 scintillator hodoscopes and nearly 400 scintillators. Each of the hodoscope pairs covers a different range of Q^2 and y. This kind of subdividing also allows for customising the respective detectors to fit the necessary requirements, like selectivity and particle rate.

System name	hodoscope name	# elements	Z-position	covered area ($X \times Y$)
Inner	H4I (up)	32	32.00 m	17.34 cm×32.00 cm
	H4I (down)	32	32.00 m	
	H5I (up)	32	51.00 m	35.30 cm×51.00 cm
	H5I (down)	32	51.00 m	
Ladder	H4LV	32	40.65 m	128.20 cm×40.00 cm
	H5LV	32	48.05 m	168.20 cm×47.50 cm
Middle	H4MV (up)	20	40.30 m	120.00 cm×102.00 cm
	H4MV (down)	20	40.30 m	
	H4MH	32	40.40 m	
	H5MV (up)	20	47.70 m	150.00 cm×120.00 cm
	H5MV (down)	20	47.70 m	
	H5MH	32	47.80 m	
Outer	H3OH	16	23.00 m	200.00 cm×100.00 cm
	H4OH (up)	32	40.00 m	480.00 cm×225.00 cm

Table 3.3: Hodoscope systems of the COMPASS trigger [40]. The letters 'H' and 'V' at the end of a hodoscope name indicate horizontally and vertically arranged scintillator slabs.

Table 3.3 lists all trigger hodoscopes and their most important properties. Hodoscopes whose names only differ by a number are regarded as two parts of a pair (cf. Section 3.5.1.1)

by the coincidence logic. Systems with more than one pair, like the 'Inner' or 'Middle' system, use the logical OR of all pairs as trigger signal.

Figure 3.15 depicts the covered kinematic regions of the respective trigger systems in the $y - Q^2$ plane. The 'Inner' and 'Ladder' systems (and part of the 'Middle' system) cover the region of small Q^2; they form the energy-loss trigger (spatial resolution in both the X and Y planes). 'Outer' and 'Middle' are parts of the deep-inelastic trigger (spatial resolution only in the X plane).
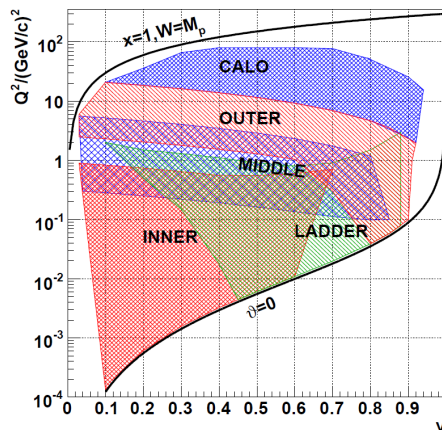
Figure 3.15: Simplified representation of the kinematic regions (momentum transfer Q^2 and energy transfer y) covered by the respective hodoscope systems [8].

3.6 Data Acquisition and Reconstruction

There are two ways to measure the analog signals of the detectors in COMPASS. Either they are measured with analog to digital converters (ADC), which yield the amplitude of the signal; or they are first discriminated and the resulting signals are measured with time to digital converters, which provide a time information of the hit. This information, combined with a unique number for every channel of every detector, is read out with each trigger, then first written to disk and finally transferred to and stored on the CERN Advanced STORage manager (CASTOR).

These data files, so-called *raw data* files, contain all available information about the recorded events. Before they can be used for a physics analysis they have to be reconstructed to extract the essential information of the physical event. In practical terms this means the reconstruction of particle tracks and vertices, energy clusters in the calorimeters, and identification of particle types from RICH data. Used for this is the official COMPASS reconstruction programme CORAL[3], a software package implemented in C++.

---

[3]CORAL: COmpass Reconstruction and AnaLysis programme

Decoding is the first step; for this the actual positions of detector channels are taken into account, as well as specific properties of the detectors, like timing and energy calibration. Completed, this results in a list of hits. The second step is *clustering*; hits in neighboring channels are grouped into clusters.

Using a Kalman filter[4] tracks and vertices are reconstructed, based on the produced list of clusters. The output of this process contains e.g. interaction vertices, track parameters and RICH likelihoods. These are written to mini Data Summary Tapes (mDST), which contain the collected and reconstructed information in root trees [43]. The actual physics analysis is performed on these mDSTs. For this PHAST (Physics Analysis Software Tools) is used. The software package provides an interface for the user to access the features of the reconstructed events, as well as a set of algorithms to compute the relevant physical values of each event, which are then stored in a user defined root subsample tree. These are then used for the final physics analyses.

---

[4]The Kalman filter is an algorithm which operates recursively on streams of noisy input data to produce a statistically optimal estimate of the underlying system state.

Chapter 4

The Extraction of Δq from COMPASS Data

In the following a brief report is given on a previous evaluation of quark helicity distributions from COMPASS data. For an in-depth description of the analysis, see [44]. The chapter is structured as follows: After a short introduction summarising the results from earlier publications, Section 4.2 specifies the data used to determine the double spin cross section asymmetries. Then the method of extraction for the polarised PDFs is explained and the results are discussed. Finally the influence of fragmentation functions on the extracted polarised distributions is examined, with special emphasis on the strange quark fragmentation functions.

4.1 Introduction

As discussed in Chapter 2 the measurement of semi-inclusive asymmetries grants a direct access to flavour-separated valence as well as sea quark contributions to the nucleon spin. The first measurement of semi-inclusive DIS (SIDIS) asymmetries was performed by the EMC collaboration in 1989 [10]. More recently, in 1997, the SMC collaboration measured SIDIS asymmetries for unidentified charged hadrons [45]. In 2008 the HERMES collaboration published semi-inclusive DIS asymmetries [24] for charged pion production on a proton and a deuteron target, and for charged kaon production on a proton target. While these asymmetries allowed for a flavour decomposition into five[1] helicity distributions, they did not permit a separate extraction of $\Delta \bar{s}$.

An earlier publication by the COMPASS collaboration presented a LO evaluation of the isoscalar[2] polarised valence, sea and strange distributions $(\Delta u_v + \Delta d_v)$, $(\Delta \bar{u} + \Delta \bar{d})$ and

---

[1]The five extracted helicity distributions were $\Delta u, \Delta d, \Delta \bar{u}, \Delta \bar{d}$, and $\Delta s = \Delta \bar{s}$.

[2]Due to the exclusive use of data collected with an isoscalar target, only the sum of the valence and antiquark distributions could be extracted.

$(\Delta s + \Delta \bar{s})$, derived from DIS and SIDIS asymmetries on a polarised deuteron target only ([23], cf. Section 2.5).

The analysis discussed here was based on several sets of asymmetries:

- new semi-inclusive asymmetries for scattering high-energy muons off a polarised proton target for

  - charged pions: $A_{1,p}^{\pi^+}$, $A_{1,p}^{\pi^-}$
  - charged kaons: $A_{1,p}^{K^+}$, $A_{1,p}^{K^-}$ (first time measurement)

- previously measured semi-inclusive asymmetries for scattering high-energy muons off a polarised deuteron target for

  - charged pions: $A_{1,d}^{\pi^+}$, $A_{1,d}^{\pi^-}$
  - charged kaons: $A_{1,d}^{K^+}$, $A_{1,d}^{K^-}$

- previously measured inclusive asymmetries for both proton and deuteron targets: $A_{1,d}$ [23], $A_{1,p}$ [46].

Using these measurements, a full flavour decomposition in LO was performed, accessing for the first time all up, down and strange quark (and antiquark) distributions separately [47].

4.2   Data and Asymmetries

The data used for this analysis were collected in 2007, using the COMPASS spectrometer (see Chapter 3). A 160 GeV muon beam was scattered off a polarised NH$_3$ target consisting of three consecutive cells. The energy of the muons was constrained to the interval 140 GeV $< E_\mu <$ 180 GeV. The deep-inelastic scattering region was defined by cuts on the photon virtuality, $Q^2 > 1\,(\mathrm{GeV/c})^2$, and on the fractional energy transfered from the muon to the virtual photon, y, constrained to $0.1 < y < 0.9$. The data sample used covered the x range of $0.004 < x < 0.7$, and consisted of 85.3 million events.

All events were required to have a reconstructed primary vertex inside one of the three target cells. Hadron tracks were required to originate from the primary vertex, with their fractional energy z larger than 0.2 in order to select hadrons produced in the current fragmentation region (cf. Section 2.5), and smaller than 0.85 to suppress hadrons produced in diffractive processes. Hadrons were identified in the RICH detector. The available momentum range was therefore restricted to an interval of $10\,\mathrm{GeV/c} < p < 50\,\mathrm{GeV/c}$ in order to ensure the identification of both pions and kaons (cf. Section 3.4.1). The total samples of π^+ (π^-) amounted to 12.3 (10.9) million hadrons, the ones for K^+ (K^-) to 3.6 (2.3) million hadrons, respectively.

The experimental double-spin asymmetries for a proton target which were used in the analysis are shown in Fig. 4.1. Two additional sets of asymmetries are displayed for comparison; the predictions of the DSSV[3] fit [48] for (x, Q^2) values of the data, and the HERMES inclusive [49] and semi-inclusive [24] measurements for π^+ and π^-. Even though no kaon data had been available for the DSSV fits, they agree very well with the COMPASS asymmetries, including the semi-inclusive kaon asymmetries. The agreement of the COMPASS and HERMES inclusive and pion asymmetries is also good, despite the different kinematic regions (in Q^2 for the same x), illustrating the fact that the Q^2 dependence for a fixed value of x is small for semi-inclusive asymmetries.
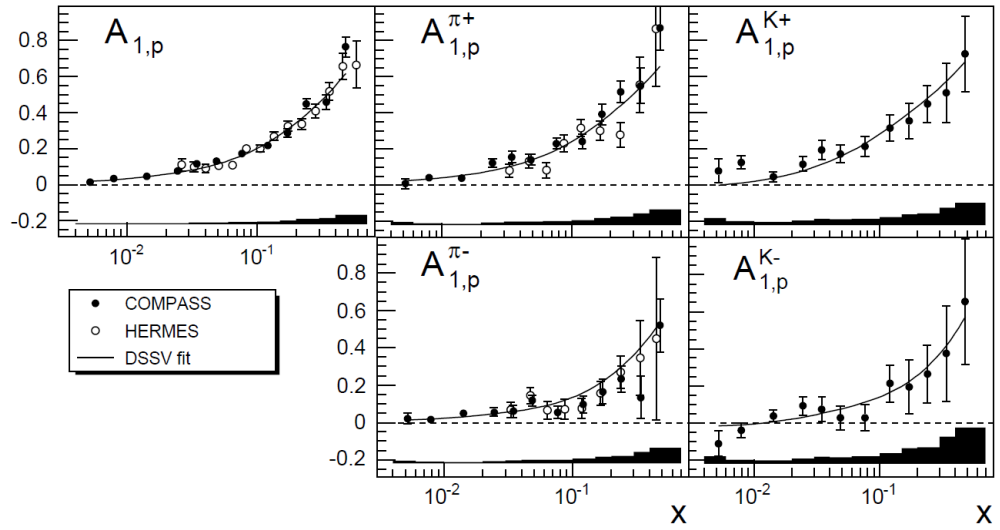
Figure 4.1: The inclusive asymmetry $A_{1,p}$ [46] and the semi-inclusive asymmetries $A_{1,p}^{\pi^+}$, $A_{1,p}^{\pi^-}$, $A_{1,p}^{K^+}$, $A_{1,p}^{K^-}$ (closed circles). The bands at the bottom of each plot show the systematic errors. The $A_{1,p}$, $A_{1,p}^{\pi^+}$ and $A_{1,p}^{\pi^-}$ measurements from HERMES [49], [24] (open circles) are shown for comparison. The curves show the predictions of the DSSV fit [48]. (plot taken from [44])

.

4.3   Extracted Helicity Distributions

At LO in QCD and under the assumption of independent quark fragmentation, the spin asymmetry for hadrons produced in the current fragmentation region can be written as (see also Eq. 2.55 in Chapter 2.3.2):

---
[3]DSSV: D. de Florian, R. Sassot, M. Stratmann, and W. Vogelsang

$$A_1^h(x, z, Q^2) = \frac{\sum_q e_q^2 \left(\Delta q(x, Q^2) D_q^h(z, Q^2) + \Delta \bar{q}(x, Q^2) D_{\bar{q}}^h(z, Q^2) \right)}{\sum_q e_q^2 \left(q(x, Q^2) D_q^h(z, Q^2) + \bar{q}(x, Q^2) D_{\bar{q}}^h(z, Q^2) \right)} \tag{4.1}$$

with $q = u, d, s$. The asymmetries were measured at the average Q^2 values in each x bin starting from $1.3 \, (\text{GeV/c})^2$ at low x up to $60 \, (\text{GeV/c})^2$ for the larges x values. Since no significant dependence upon Q^2 had been observed, the Q^2 dependence was neglected in the analysis; all measurements were assumed to be valid at $Q_0^2 = 3 \, (\text{GeV/c})^2$. The unpolarised PDFs (in LO) from the MRST parametrisation [25] were used, the fragmentation functions were taken from the DSS LO parametrisation [26].

The values for the unpolarised MRST PDFs originate from the measured structure function F_2 in which the ratio $R = \sigma_L/\sigma_T$ adopts non-zero values whereas R is assumed to be zero at LO (cf. Eq. 2.24). To correct for this, the asymmetries were divided by $1 + R(x, Q_0^2)$. The asymmetries for a deuteron target were corrected by a factor $(1 - 1.5\omega_D)$ with ω_D being the probability for a deuteron to be in a D state[4].

Integrating over the measured range of z ($0.2 < z < 0.85$) and neglecting the Q^2 dependence of the asymmetries, Eq. 4.1 is reduced to:

$$A_1^h(x) = \frac{\sum_q e_q^2 \left(\Delta q(x) D_q^h + \Delta \bar{q}(x) D_{\bar{q}}^h \right)}{\sum_q e_q^2 \left(q(x) D_q^h + \bar{q}(x) D_{\bar{q}}^h \right)}, \tag{4.2}$$

in which D_q^h stands for $\int_{0.2}^{0.85} D_q^h(z, Q_0^2 = 3(GeV/c)^2$. The ten asymmetries used in the analysis ($A_{1,p}$, $A_{1,p}^{\pi^\pm}$, $A_{1,p}^{K^\pm}$, $A_{1,d}$, $A_{1,d}^{\pi^\pm}$, $A_{1,d}^{K^\pm}$) provide a system of ten equations for six unknowns (Δu, Δd, Δs, $\Delta \bar{u}$, $\Delta \bar{d}$, $\Delta \bar{s}$):

$$\vec{A} = B \vec{\Delta q}, \tag{4.3}$$

with

$$\vec{A} = \left(A_{1,p}, A_{1,p}^{\pi^\pm}, A_{1,p}^{K^\pm}, A_{1,d}, A_{1,d}^{\pi^\pm}, A_{1,d}^{K^\pm} \right), \tag{4.4}$$

and

$$\vec{\Delta q} = \left(\Delta u, \Delta d, \Delta d, \Delta \bar{u}, \Delta \bar{d}, \Delta \bar{s} \right). \tag{4.5}$$

B is a matrix containing linear combinations of the unloarised PDFs. To extract the polarised quark distributions $\Delta q(x)$ as a function of x, the system of equations had to be

---

[4]D state refers to an orbital angular momentum of $L = 2$. The deuteron D-state admixture accounts for its magnetic moment: $\omega_D \approx 0.04$.

solved in each x bin by performing a least-square fit, which required to minimize the χ^2, defined by:

$$\chi^2 = (\vec{A} - B\vec{\Delta q})^T (cov_A)^{-1} (\vec{A} - B\vec{\Delta q}), \tag{4.6}$$

where cov_A is the covariance matrix containing the uncertainties of the measured asymmetries.

Since the antiquark distributions become insignificant for large values of x, $x = 0.3$ was used as an upper limit for the analysis. Above this limit, $\Delta u(x)$ and $\Delta d(x)$ were taken from the inclusive structure functions $g_1^p(x)$ and $g_1^d(x)$ (assuming the antiquark helicity distributions $\Delta\bar{q}$ to be zero).

Figure 4.2 shows the results of the least-square fit for the Δs and $\Delta\bar{s}$ distributions, as well as the difference $\Delta s - \Delta\bar{s}$. Both distributions are compatible with zero within the measured range. This also applies to their difference.
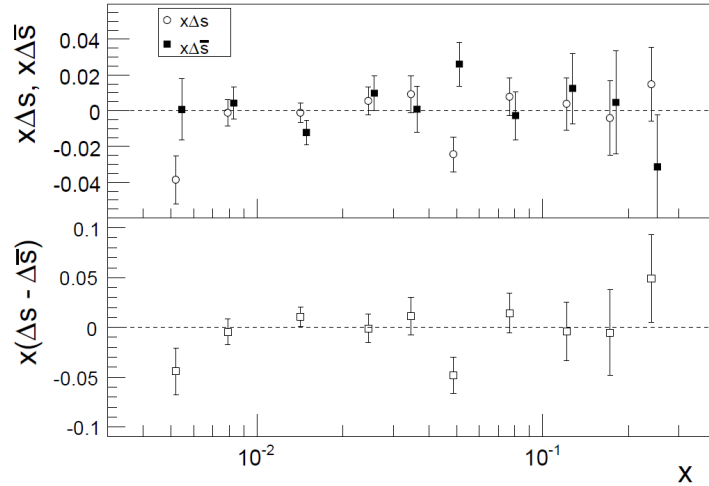
Figure 4.2: Comparison of $x\Delta s$ (open circles) and $x\Delta\bar{s}$ (squares) at $Q_0^2 = 3\,(\text{GeV/c})^2$ (top) and the corresponding values of the difference $x(\Delta s - \Delta\bar{s})$ (bottom) (plot taken from [44])
.

For unpolarised PDFs of the MRST parametrisation $s(x) = \bar{s}(x)$ was assumed. To verify that this assumption does not artificially generate the vanishing values for $\Delta s - \Delta\bar{s}$, the $s(x)$ and $\bar{s}(x)$ distributions were scaled simultaneously by a factor of 2 and 0.5, respectively, and allowed to differ by a factor up to 2 in any interval of x. The resulting values of Δs and $\Delta\bar{s}$ were found to be nearly independent of those modifications.

It was concluded that there is no significant difference between $\Delta s(x)$ and $\Delta\bar{s}(x)$ in the covered range; a conclusion that also remained valid when the DSS fragmentation functions

used in the fit were replaced by those derived by the EMC collaboration. Therefore the distributions of $\Delta s(x)$ and $\Delta \bar{s}(x)$ were assumed to be equal, reducing the number of unknowns from six to five, which in turn improved the statistical precision of the fit results.

The results for the quark helicity distributions $\Delta u(x)$, $\Delta d(x)$, $\Delta \bar{u}(x)$, $\Delta \bar{d}(x)$ and $\Delta s(x)$ $(\Delta s(x) = \Delta \bar{s}(x))$ are shown in Fig. 4.3. Three additional values of $\Delta u(x)$ and $\Delta d(x)$ are displayed for the range $0.3 < x < 0.7$, derived from the $g_1^p(x)$ and $g_1^d(x)$ structure functions. The curves show the results of the DSSV fit at Next-to-Leading Order (NLO) [48]. Therefore the comparison with the experimental results derived at LO can be only qualitative. Even so, the DSSV curves reproduce the shape of the data quite well, which indicates that a direct extraction at LO provides a good estimate of the shape of the helicity distributions.

The antiquark distributions $\Delta \bar{u}$ and $\Delta \bar{d}$ do not show any significant variation in x; $\Delta \bar{u}$ remains consistant with zero in the measured range, while $\Delta \bar{d}$ is slightly negative.
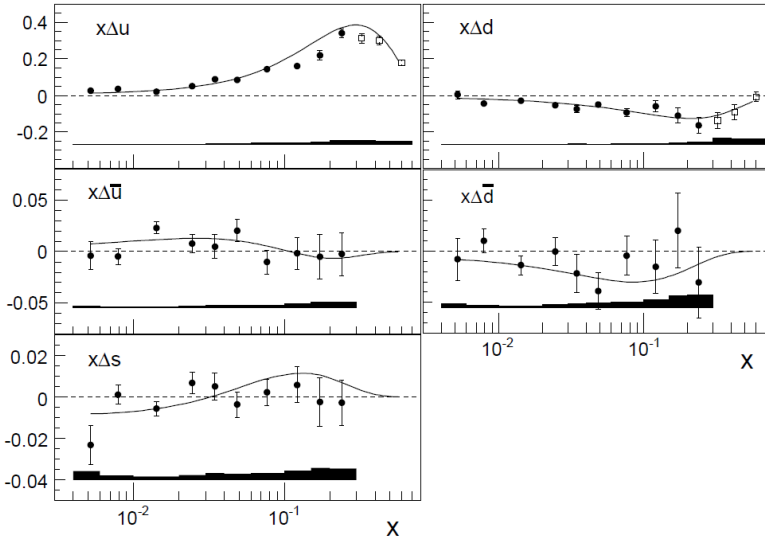
Figure 4.3: The quark helicity distributions $x\Delta u$, $x\Delta \bar{u}$, $x\Delta u$, $x\Delta \bar{u}$, $x\Delta u$ at $Q_0^2 = 3\,(\mathrm{GeV/c})^2$ as a function of x. The values for $x < 0.3$ (black dots) are derived at LO from the COMPASS spin asymmetries using the DSS fragmentation functions. The values for $x > 0.3$ (squares) are derived from the values of the polarised structure function $g_1(x)$, assuming $\Delta \bar{q} = 0$. The bands at the bottom show the systematic errors, the curves show the predictions of the DSSV fit calculated at NLO (plot taken from [44]).

The values of the strange quark helicity distribution confirm the results obtained from the deuteron data ([23], cf. Chapter 2.5), with slightly reduced errors. With the first point at low x as the only exception $\Delta s(x)$ shows no significant variation and remains compatible with zero over the measured range. These results are particularly interesting,

due to the apparent contradiction between the inclusive and semi-inclusive measurements already outlined previously (cf. Chapters 1 and 2); while the first moment of the polarised strange quark distribution derived from the spin structure function $g_1(x)$ [50] is large and negative, the semi-inclusive results indicate a $\Delta s(x)$ compatible with zero in the measured x range.

Two possible explanations for these observations are a breaking of the $SU(3)$ flavour symmetry, or a sign change of $\Delta s(x)$ at lower values of x. Supporting the first possibility are recent model calculations[5] [51], resulting in a non-negative value for the first moment of Δs. The second option is used by the DSSV fit, which compensates for the differences between the results from inclusive and semi-inclusive measurements by including a negative contribution for small values of x.

Finally, as already illustrated in Chapter 2.5, the results for the polarised parton distributions depend strongly on the fragmentation functions used in the analysis. This will be further explored in Section 4.4.

4.3.1 First Moments of Δq

The first moments of the helicity distributions are listed in Table 4.1. The missing contributions outside the measured range have been evaluated twice, once by extrapolating the measured values, and alternatively by using the values provided by the DSSV parametrisation.

	Extrapolation	DSSV
Δu	$0.71 \pm 0.02 \pm 0.03$	$0.71 \pm 0.02 \pm 0.03$
Δd	$-0.34 \pm 0.04 \pm 0.03$	$-0.35 \pm 0.04 \pm 0.03$
$\Delta \bar{u}$	$0.02 \pm 0.02 \pm 0.01$	$0.03 \pm 0.02 \pm 0.01$
$\Delta \bar{d}$	$-0.05 \pm 0.03 \pm 0.02$	$-0.07 \pm 0.03 \pm 0.02$
$\Delta s(\Delta \bar{s})$	$-0.01 \pm 0.01 \pm 0.01$	$-0.05 \pm 0.01 \pm 0.01$
Δu_v	$0.68 \pm 0.03 \pm 0.03$	$0.68 \pm 0.03 \pm 0.03$
Δd_v	$-0.29 \pm 0.06 \pm 0.03$	$-0.28 \pm 0.06 \pm 0.03$
$\Delta \Sigma$	$0.32 \pm 0.03 \pm 0.03$	$0.22 \pm 0.03 \pm 0.03$

Table 4.1: Full first moments of the quark helicity distributions at $Q_0^2 = 3\,(GeV)^2$. The unmeasured contributions at low and high x were estimated by extrapolating the data towards $x = 0$ and $x = 1$ and by using the DSSV parametrisation (data taken from [44]).

---

[5]The evaluation of Δs from inclusive measurements relies on the value of the octet axial charge a_8, which in turn is derived - under the assumption of $SU(3)_f$ symmetry - from hyperon weak decays. A possible solution is offered by [51], suggesting a substantially reduced value for a_8, in which case the inclusive data would no longer imply a negative value $\Delta s(x)$.

Both methods lead to similar values for the valence quark moments $\Delta u_v = \Delta u - \Delta \bar{u}$ and $\Delta d_v = \Delta d - \Delta \bar{d}$. However, the results for the strange quark moments show considerable differences, depending on the method of evaluation. The values for the first moments of Δs ($\Delta \bar{s}$) derived using the DSSV parametrisation are not compatible with zero, but significantly negative due to the sign change of the parametrisation at $x = 0.03$. Consequently, the values for $\Delta \Sigma$, as the total sum of the valence and sea quark contributions, differ strongly for the two evaluations.

4.4 Influence of Fragmentation Functions on Δq

As already explored in Chapter 2.5, the relation between the semi-inclusive asymmetries and the quark helicity distributions depends only on ratios of fragmentation functions integrated over the measured interval of z ($0.2 < z < 0.85$). The relevant ratios for kaon asymmetries are R_{SF} and R_{UF}, of the strange-to-favoured and unfavoured-to-favoured fragmentation functions (cf. Eq. 2.61). Both ratios have distinct values for the fragmentation function parametrisations used; $R_{SF} = 6.6$ and $R_{UF} = 0.13$ for DSS, and $R_{SF} = 3.4$ and $R_{UF} = 0.35$ for EMC.

The dependence of the first moments (truncated to the measured range) on the fragmentation functions was evaluated as follows: R_{SF} was gradually increased from 2.0 to 7.0. To ensure that the K^+ multiplicities remained approximately constant, the value of R_{UF} was decreased simultaneously. For this the relation $R_{UF} = 0.35 - 0.07(R_{SF} - 3.4)$ was used, resulting in values of 0.45 to 0.10 for the unfavoured-to-favoured ratio.

Figure 4.4 shows the resulting first moments Δu, $\Delta \bar{u}$, Δd, $\Delta \bar{d}$, Δs, ($\Delta \bar{u} - \Delta \bar{d}$) as a function of R_{SF}. The values of Δu decrease from 0.50 to 0.47, while the ones for $\Delta \bar{u}$ increase from zero to 0.015 with the evolution of R_{SF} from EMC to DSS values. Δd and $\Delta \bar{d}$ remain nearly constant. Correspondingly, the difference $\Delta \bar{u} - \Delta \bar{d}$ follows the same trend as $\Delta \bar{u}$.

Δs on the other hand changes much more strongly. It increases from -0.04 for the EMC fragmentation functions to -0.01 for the DSS FFs, although is has to be noted that the statistical uncertainty for the EMC fragmentation functions is quite large.

4.5 Conclusions

The inclusive and semi-inclusive asymmetries measured by the COMPASS collaboration were used to evaluate the quark and antiquark helicity distributions Δu, Δd, $\Delta \bar{u}$, $\Delta \bar{d}$ and Δs (assumed equal to $\Delta \bar{s}$). The first moments determined for all extracted distributions have been found in good agreement with previous measurements and the DSSV parametrisation.

The problem of the discrepancies between evaluations of the strange quark contribution to the nucleon spin from inclusive and semi-inclusive measurements has remained unsolved so
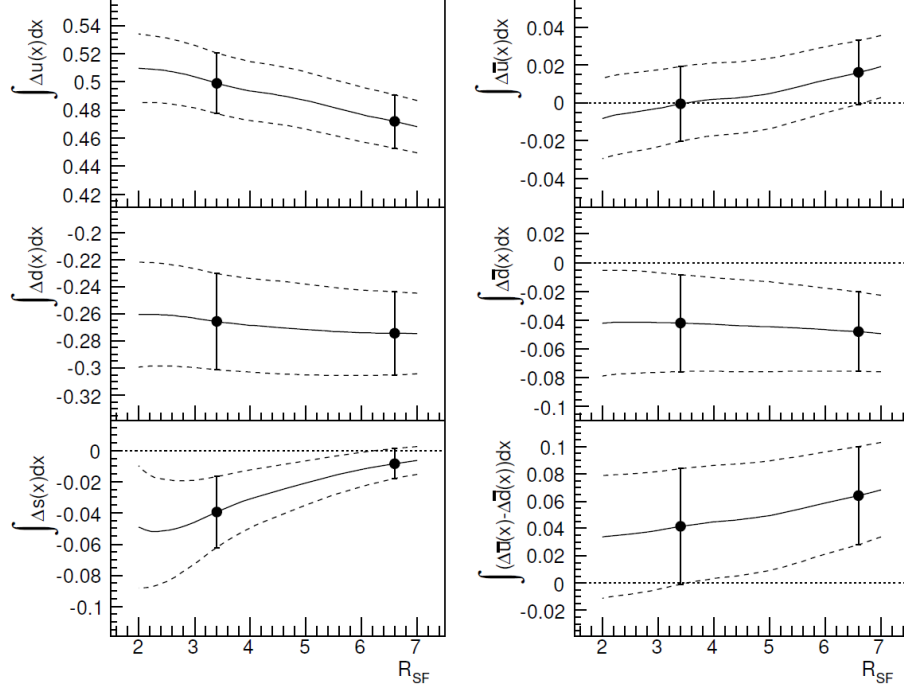
Figure 4.4: Variation of the first moments Δu, $\Delta \bar{u}$, Δd, $\Delta \bar{d}$, Δs, $\Delta \bar{u} - \Delta \bar{d}$, integrated over the interval $0.004 < x < 0.3$ as a function of the ratio R_{SF} of s and u quark fragmentation functions into K^+. The ratio R_{UF} is varied linearly from 0.13 at $R_{SF} = 6.6$ to 0.35 at $R_{SF} = 3.4$. The black dots indicate the values obtained using the EMC and the DSS kaon fragmentation functions, respectively (plot taken from [44]).

.

far. However, studies have been performed, examining the evolution of the first moments of the extracted helicity distributions with the FF ratios R_{SF} and R_{UF}. The results strongly indicate a substantial dependence of the extracted polarised PDFs on the fragmentation functions used in the analysis. The moments of Δu, $\Delta \bar{u}$ and Δs all vary significantly with the choice of fragmentation functions. Particularly for Δs this dependence appears to be critical; a negative strange quark contribution may be possible, although the uncertainties for the evaluation are very large.

A more precise determination of fragmentation functions is therefore essential. The development of a method for the extraction of FFs from COMPASS data is the main subject of this thesis and will be covered in detail in the following chapters.

Chapter 5

The Extraction of Fragmentation Functions from COMPASS Data

In the following a method for extracting fragmentation functions from hadron multiplicities is developed and tested. As described in detail in Section 2.5, and again illustrated by the results presented in Chapter 4, the evaluation of the strange quark helicity distribution from semi-inclusive asymmetries depends strongly on the fragmentation functions used in the analysis. Kaon fragmentation functions in particular are poorly known; therefore an independent evaluation of those FFs would be useful for the further exploration of the nucleon spin distribution.

5.1   Method of Extraction

The starting point in deriving the method of extraction of fragmentation functions is the relation between the number of hadrons $\frac{dN^h}{dxdz}$, depending on the two scaling variables x and z, and the unpolarised quark distributions, $q(x)$, and the fragmentation functions, $D_q^h(z)$:

$$\frac{dN^h}{dxdz} \sim \sum_q e_q^2 q(x) D(z).$$

(5.1)

There is an additional Q^2 dependence to all the factors (cf. Section 2.4.1), which is omitted here. Normalised to the number of scattered leptons $\frac{dN^l}{dx}$ one obtains in LO QCD:

$$r^h(x, z) = \frac{\frac{dN^h}{dxdz}}{\frac{dN^l}{dx}} = \frac{\sum_q e_q^2 q(x) D_q^h(z)}{\sum_q e_q^2 q(x)},$$

(5.2)

where $r^h(x, z)$ stands for the hadron multiplicities (cf. Eq. 2.31). The sum runs over all six light quark flavours: $q = u, d, s, \bar{u}, \bar{d}, \bar{s}$.

For a proton target Eq. 5.2 reads:

$$r^h(x, z) = \frac{4uD_u^h + dD_d^h + sD_s^h + 4\bar{u}D_{\bar{u}}^h + \bar{d}D_{\bar{d}}^h + \bar{s}D_{\bar{s}}^h}{4(u + \bar{u}) + (d + \bar{d}) + (s + \bar{s})}. \tag{5.3}$$

For a deuteron target the relation can be expressed via the sum for a proton and neutron target. Using isospin symmetry ($u_{proton} \equiv d_{neutron}$ and $d_{proton} \equiv u_{neutron}$) one finds:

$$r^h(x, z) = \frac{(u + d)(4D_u^h + D_d^h) + (\bar{u} + \bar{d})(4D_{\bar{u}}^h + D_{\bar{d}}^h) + 2sD_s^h + 2\bar{s}D_{\bar{s}}^h}{5(u + \bar{u} + d + \bar{d}) + 2(s + \bar{s})}. \tag{5.4}$$

Using existing parametrisations for the unpolarised PDFs, and the multiplicities measured by the COMPASS collaboration [39], these equations can be used to extract fragmentation functions.

If now a hadron type h is specified, twelve fragmentation functions appear in this expression, corresponding to six quark flavours and two hadron charges. For instance, for charged kaons (K^+, K^-) these twelve fragmentation functions are: $D_u^{K^+}$, $D_d^{K^+}$, $D_s^{K^+}$, $D_{\bar{u}}^{K^+}$, $D_{\bar{d}}^{K^+}$, $D_{\bar{s}}^{K^+}$, $D_u^{K^-}$, $D_d^{K^-}$, $D_s^{K^-}$, $D_{\bar{u}}^{K^-}$, $D_{\bar{d}}^{K^-}$, $D_{\bar{s}}^{K^-}$. Assuming charge conjugation symmetry ($D_u^{K^+} = D_{\bar{u}}^{K^-}$, $D_d^{K^+} = D_{\bar{d}}^{K^-}$, ...), this number can be reduced to six[1].

5.2   System of Equations for Kaons

For kaons ($K^+ \equiv \bar{s}u$, $K^- \equiv s\bar{u}$) these remaining six fragmentation functions ($D_u^{K^+}$, $D_d^{K^+}$, $D_s^{K^+}$, $D_{\bar{u}}^{K^+}$, $D_{\bar{d}}^{K^+}$, $D_{\bar{s}}^{K^+}$) can be classified as follows:

The largest one is the favoured strange quark fragmentation function, $D_{\bar{s}}^{K^+}$, followed in magnitude by the favoured up quark fragmentation function, $D_u^{K^+}$, and the unfavoured fragmentation functions, $D_s^{K^+}$, $D_{\bar{u}}^{K^+}$, $D_{\bar{d}}^{K^+}$, $D_d^{K^+}$.

In a first step it is now assumed that these unfavoured fragmentation functions are the same. They are denoted D_{unf}. Correspondingly, the strange quark favoured fragmentation function is denoted D_{str}, and up quark favoured fragmentation function D_{fav}.

---

[1]No further symmetry considerations apply. Note that the isospin partner of K^+ is K^0.

An overview of the three groups, their denotations, and the fragmentation functions contained is given in the following table:

D_{str}	$D_{\bar{s}}^{K^+} \equiv D_s^{K^-}$			
D_{fav}	$D_u^{K^+} \equiv D_{\bar{u}}^{K^-}$			
D_{unf}	$D_s^{K^+} \equiv D_{\bar{s}}^{K^-}$,	$D_{\bar{u}}^{K^+} \equiv D_u^{K^-}$,	$D_d^{K^+} \equiv D_{\bar{d}}^{K^-}$,	$D_{\bar{d}}^{K^+} \equiv D_d^{K^-}$

For a deuteron target this leads to the following equations:

$$r^{K^+} = \frac{2\bar{s}\mathbf{D_{str}} + 4(u+d)\mathbf{D_{fav}} + (u+d+5(\bar{u}+\bar{d})+2s)\mathbf{D_{unf}}}{5(u+d+\bar{u}+\bar{d}+2(s+\bar{s}))} \tag{5.5}$$

$$r^{K^-} = \frac{2s\mathbf{D_{str}} + 4(\bar{u}+\bar{d})\mathbf{D_{fav}} + (\bar{u}+\bar{d}+5(u+d)+2\bar{s})\mathbf{D_{unf}}}{5(u+d+\bar{u}+\bar{d}+2(s+\bar{s}))} \tag{5.6}$$

The next step makes use of the factorisation ansatz for hadron production in deep-inelastic scattering (cf. Section 2.2.2); the assumption that the unpolarised PDFs, $q(x)$, only depend on x, while the fragmentation functions $D_q^h(z)$ only depend on z . By writing Eq.s 5.5 and 5.6 in bins of x for a fixed range of z allows to extract the fragmentation functions for this z range:

$$\vec{r} = B(q) \times \vec{D}. \tag{5.7}$$

The resulting system of equations for twelve bins of x is:

$$
\begin{pmatrix}
r^{K^+}(x_1) \\
r^{K^-}(x_1) \\
\\
r^{K^+}(x_2) \\
r^{K^-}(x_2) \\
\vdots \\
r^{K^+}(x_{12}) \\
r^{K^-}(x_{12})
\end{pmatrix}
=
\begin{pmatrix}
b_{1,1} & b_{1,2} & b_{1,3} \\
b_{2,1} & b_{2,2} & b_{2,3} \\
\\
b_{3,1} & b_{3,2} & b_{3,3} \\
b_{4,1} & b_{4,2} & b_{4,3} \\
\vdots & \vdots & \vdots \\
b_{23,1} & b_{23,2} & b_{23,3} \\
b_{24,1} & b_{24,2} & b_{24,3}
\end{pmatrix}
\begin{pmatrix}
\mathbf{D_{str}} \\
\\
\mathbf{D_{fav}} \\
\\
\mathbf{D_{unf}}
\end{pmatrix}. \tag{5.8}
$$

The entries $b_{i,i}$ for the matrix B contain the unpolarised PDFs according to Eq.s 5.5 and 5.6:

$$
\begin{pmatrix}
r^{K^+}(x_1) \\
r^{K^-}(x_1) \\
\\
r^{K^+}(x_2) \\
r^{K^-}(x_2) \\
\vdots \\
r^{K^+}(x_{12}) \\
r^{K^-}(x_{12})
\end{pmatrix}
=
\begin{pmatrix}
\frac{[2\bar{s}](x_1)}{DIS(x_1)} & \frac{[4(u+d)](x_1)}{DIS(x_1)} & \frac{[u+d+5(\bar{u}+\bar{d})+2s](x_1)}{DIS(x_1)} \\
\frac{[2s](x_1)}{DIS(x_1)} & \frac{[4(\bar{u}+\bar{d})](x_1)}{DIS(x_1)} & \frac{[\bar{u}+\bar{d}+5(u+d)+2\bar{s}](x_1)}{DIS(x_1)} \\
\\
\frac{[2\bar{s}](x_2)}{DIS(x_2)} & \frac{[4(u+d)](x_2)}{DIS(x_2)} & \frac{[u+d+5(\bar{u}+\bar{d})+2s](x_2)}{DIS(x_2)} \\
\frac{[2s](x_2)}{DIS(x_2)} & \frac{[4(\bar{u}+\bar{d})](x_2)}{DIS(x_2)} & \frac{[\bar{u}+\bar{d}+5(u+d)+2\bar{s}](x_2)}{DIS(x_2)} \\
\vdots & \vdots & \vdots \\
\frac{[2\bar{s}](x_{12})}{DIS(x_{12})} & \frac{[4(u+d)](x_{12})}{DIS(x_{12})} & \frac{[u+d+5(\bar{u}+\bar{d})+2s](x_{12})}{DIS(x_{12})} \\
\frac{[2s](x_{12})}{DIS(x_{12})} & \frac{[4(\bar{u}+\bar{d})](x_{12})}{DIS(x_{12})} & \frac{[\bar{u}+\bar{d}+5(u+d)+2\bar{s}](x_{12})}{DIS(x_{12})}
\end{pmatrix}
\begin{pmatrix}
\mathbf{D_{str}} \\
\\
\mathbf{D_{fav}} \\
\\
\mathbf{D_{unf}}
\end{pmatrix}, \quad (5.9)
$$

with $DIS(x_i) = 5[u + d + \bar{u} + \bar{d} + 2(s + \bar{s})](x_i)$.

In a simple model the nucleon can be described in terms of a valence quark (q_v) and a sea quark distribution ($\bar{q}$). The u and d valence quark distributions differ only in magnitude, but not in shape, and all sea quark distributions are considered to be roughly equal (see Fig. 5.1).
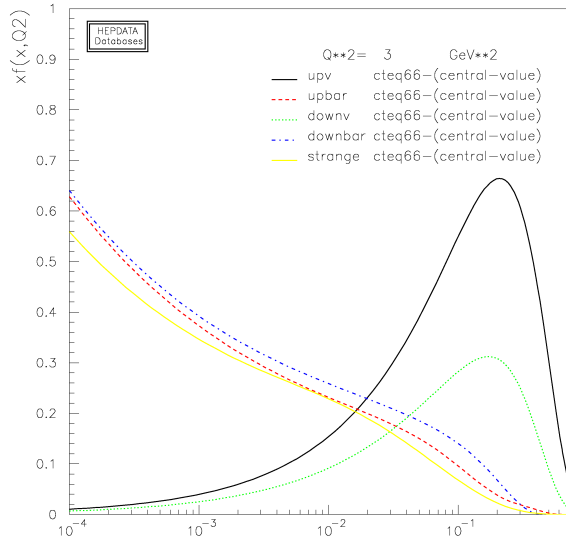
Figure 5.1: Parton distribution functions from the CTEQ6 parametrisation. In a simplified model all sea quark distributions can be considered roughly equal [52].

In this case the resulting unpolarised PDFs for the individual quark flavours can be written as:

$$u(x) = 2q_v(x) + \alpha_u \bar{q}(x) \tag{5.10}$$

$$d(x) = q_v(x) + \alpha_d \bar{q}(x) \tag{5.11}$$

$$q(x) = \alpha_q \bar{q}(x) \tag{5.12}$$

for $q = \bar{u}, \bar{d}, s, \bar{s}$.

With this the matrix in Eq. 5.9 can be re-written as:

$$
\begin{pmatrix}
r^{K^+}(x_1) \\
r^{K^-}(x_1) \\
\\
r^{K^+}(x_2) \\
r^{K^-}(x_2) \\
\vdots \\
r^{K^+}(x_{12}) \\
r^{K^-}(x_{12})
\end{pmatrix}
=
\begin{pmatrix}
\frac{[2\alpha_q \bar{q}](x_1)}{DIS(x_1)} & \frac{[12q_v + 8\alpha_q \bar{q}](x_1)}{DIS(x_1)} & \frac{[3q_v + 14\alpha_q \bar{q}](x_1)}{DIS(x_1)} \\
\frac{[2\alpha_q \bar{q}](x_1)}{DIS(x_1)} & \frac{[8\alpha_q \bar{q}](x_1)}{DIS(x_1)} & \frac{[15q_v + 14\alpha_q \bar{q}](x_1)}{DIS(x_1)} \\
\\
\frac{[2\alpha_q \bar{q}](x_2)}{DIS(x_2)} & \frac{[12q_v + 8\alpha_q \bar{q}](x_2)}{DIS(x_2)} & \frac{[3q_v + 14\alpha_q \bar{q}](x_2)}{DIS(x_2)} \\
\frac{[2\alpha_q \bar{q}](x_2)}{DIS(x_2)} & \frac{[8\alpha_q \bar{q}](x_2)}{DIS(x_2)} & \frac{[15q_v + 14\alpha_q \bar{q}](x_2)}{DIS(x_2)} \\
\vdots & \vdots & \vdots \\
\frac{[2\alpha_q \bar{q}](x_{12})}{DIS(x_{12})} & \frac{[12q_v + 8\alpha_q \bar{q}](x_{12})}{DIS(x_{12})} & \frac{[3q_v + 14\alpha_q \bar{q}](x_{12})}{DIS(x_{12})} \\
\frac{[2\alpha_q \bar{q}](x_{12})}{DIS(x_{12})} & \frac{[8\alpha_q \bar{q}](x_{12})}{DIS(x_{12})} & \frac{[15q_v + 14\alpha_q \bar{q}](x_{12})}{DIS(x_{12})}
\end{pmatrix}
\begin{pmatrix}
\mathbf{D_{str}} \\
\\
\mathbf{D_{fav}} \\
\\
\mathbf{D_{unf}}
\end{pmatrix}. \tag{5.13}
$$

Analysing Eq. 5.13 one finds the rank of the matrix containing the unpolarised PDFs is three. Thus, even by using a very simplified model of nucleon quark distributions as described above, and without regarding the values of the α_q, the system of equations represented by the matrix can be solved for three unknown fragmentation functions.

5.2.1   Assumption $D_s^{K^+} = D_{\bar{u}}^{K^+} = D_d^{K^+} = D_{\bar{d}}^{K^+}$

While the assumption $D_d^{K^+} = D_{\bar{d}}^{K^+}$ seems valid considering the quark content of the K^+ ($\equiv u\bar{s}$), a more careful consideration of the processes involved in the production of charged kaons yields another picture. A K^+ may originate from $K^{0*} \equiv d\bar{s}$ via the decay $K^+\pi^-$ but not from $\bar{K}^{0*} \equiv \bar{d}s$ which decays to $K^-\pi^+$. Therefore a K^+ is more likely to be produced from a d quark, via K^{0*}, than from a $\bar{d}$ quark. This leads to the expectation $D_d^{K^+} > D_{\bar{d}}^{K^+}$. To confirm this assumption, the particle physics event generator PYTHIA [53] was used to simulate the fragmentation process for kaons.

The values for the PYTHIA generated kaon fragmentation are plotted in Fig. 5.2, for $0.2 < z < 1$. The integrated values are listed in Table 5.1. The results confirm the above explained expectations. So is e.g. $D_d^{K^+} \approx 2D_{\bar{d}}^{K^+}$.
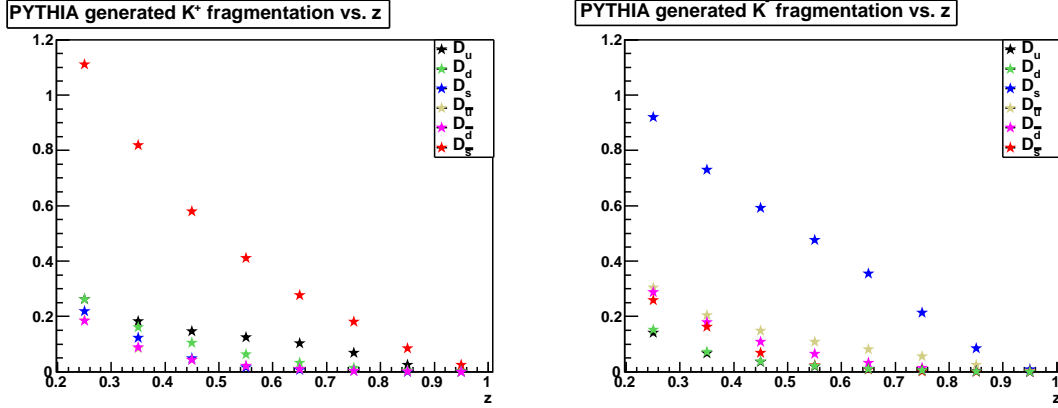
Figure 5.2: Kaon fragmentation functions generated with PYTHIA [53]. The fragmentation functions are plotted in eight z bins, with a bin width of $dz = 0.1$

Considering these findings, it does seem advisable to increase the number of fragmentation function groups to extract from three to four.

quark q	hadron h	$\int_{0.2}^{1} D_q^h(z)$	quark q	hadron h	$\int_{0.2}^{1} D_q^h(z)$
$\bar{s}$	K^+	0.358	s	K^-	0.342
u	K^+	0.092	$\bar{u}$	K^-	0.093
d	K^+	0.061	$\bar{d}$	K^-	0.067
s	K^+	0.043	$\bar{s}$	K^-	0.052
$\bar{u}$	K^+	0.036	u	K^-	0.030
$\bar{d}$	K^+	0.037	d	K^-	0.029

Table 5.1: Expected values for the kaon fragmentation functions from PYTHIA simulation

5.2.2   Alternative System of Equations for Kaons

For this approach the remaining six fragmentation functions for charged kaons ($D_u^{K^+}$, $D_d^{K^+}$, $D_s^{K^+}$, $D_{\bar{u}}^{K^+}$, $D_{\bar{d}}^{K^+}$, $D_{\bar{s}}^{K^+}$) are classified in a slightly different way. They are now divided into four different groups; the first consisting of the favoured strange quark fragmentation function, $D_{\bar{s}}^{K^+}$, followed by the favoured up quark fragmentation function, $D_u^{K^+}$. The unfavoured fragmentation functions are again divided into two groups, according to the expected values from the PYTHIA simulation (see Table 5.1). The third group is made up of the unfavoured fragmentaion functions for the d and s quarks, $D_d^{K^+}$ and $D_s^{K^+}$ (PYTHIA values of 0.06 and 0.05, respectively), while the fourth one contains the fragmentation functions with the smallest expected values (0.03), $D_{\bar{u}}^{K^+}$ and $D_{\bar{d}}^{K^+}$.

The new denotations are listed in table below:

D_{str}	$D_{\bar{s}}^{K^+} \equiv D_s^{K^-}$
D_{fav}	$D_u^{K^+} \equiv D_{\bar{u}}^{K^-}$
D_{uf1}	$D_s^{K^+} \equiv D_{\bar{s}}^{K^-}$, $D_d^{K^+} \equiv D_{\bar{d}}^{K^-}$
D_{uf2}	$D_{\bar{u}}^{K^+} \equiv D_u^{K^-}$, $D_{\bar{d}}^{K^+} \equiv D_d^{K^-}$

For a deuteron target this leads to the following equations:

$$r^{K^+} = \frac{2\bar{s}\mathbf{D_{str}} + 4(u+d)\mathbf{D_{fav}} + (u+d+2s)\mathbf{D_{uf1}} + 5(\bar{u}+\bar{d})\mathbf{D_{uf2}}}{5(u+d+\bar{u}+\bar{d}+2(s+\bar{s}))} \tag{5.14}$$

$$r^{K^-} = \frac{2s\mathbf{D_{str}} + 4(\bar{u}+\bar{d})\mathbf{D_{fav}} + (\bar{u}+\bar{d}+2\bar{s})\mathbf{D_{uf1}} + 5(u+d)\mathbf{D_{uf2}}}{5(u+d+\bar{u}+\bar{d}+2(s+\bar{s}))}. \tag{5.15}$$

Like before (cf. Section 5.2) one can take advantage of the fact that the unpolarised parton distributions only depend on x, while the fragmentation functions only depend on z (see Eq. 5.7). The obtained system on equations now has the structure:

$$\begin{pmatrix} r^{K^+}(x_1) \\ r^{K^-}(x_1) \\ \\ r^{K^+}(x_2) \\ r^{K^-}(x_2) \\ \\ \vdots \\ \\ r^{K^+}(x_{12}) \\ r^{K^-}(x_{12}) \end{pmatrix} = \begin{pmatrix} b_{1,1} & b_{1,2} & b_{1,3} & b_{1,4} \\ b_{2,1} & b_{2,2} & b_{2,3} & b_{2,4} \\ \\ b_{3,1} & b_{3,2} & b_{3,3} & b_{3,4} \\ b_{4,1} & b_{4,2} & b_{4,3} & b_{4,4} \\ \\ \vdots & \vdots & \vdots \\ \\ b_{23,1} & b_{23,2} & b_{23,3} & b_{23,4} \\ b_{24,1} & b_{24,2} & b_{24,3} & b_{24,4} \end{pmatrix} \begin{pmatrix} \mathbf{D_{str}} \\ \\ \mathbf{D_{fav}} \\ \\ \mathbf{D_{uf1}} \\ \\ \mathbf{D_{uf2}} \end{pmatrix}. \tag{5.16}$$

The entries $b_{i,i}$ for the matrix B contain the unpolarised PDFs according to Eq.s 5.14 and 5.15:

$$
\begin{pmatrix}
r^{K^+}(x_1) \\
r^{K^-}(x_1) \\
\\
r^{K^+}(x_2) \\
r^{K^-}(x_2) \\
\\
\vdots \\
\\
r^{K^+}(x_{12}) \\
r^{K^-}(x_{12})
\end{pmatrix}
=
\begin{pmatrix}
\frac{[2\bar{s}](x_1)}{DIS(x_1)} & \frac{[4(u+d)](x_1)}{DIS(x_1)} & \frac{[u+d+2s](x_1)}{DIS(x_1)} & \frac{[5(\bar{u}+\bar{d})](x_1)}{DIS(x_1)} \\
\frac{[2s](x_1)}{DIS(x_1)} & \frac{[4(\bar{u}+\bar{d})](x_1)}{DIS(x_1)} & \frac{[\bar{u}+\bar{d}+2\bar{s}](x_1)}{DIS(x_1)} & \frac{[5(u+d)](x_1)}{DIS(x_1)} \\
\\
\frac{[2\bar{s}](x_2)}{DIS(x_2)} & \frac{[4(u+d)](x_2)}{DIS(x_2)} & \frac{[u+d+2s](x_2)}{DIS(x_2)} & \frac{[5(\bar{u}+\bar{d})](x_2)}{DIS(x_2)} \\
\frac{[2s](x_2)}{DIS(x_2)} & \frac{[4(\bar{u}+\bar{d})](x_2)}{DIS(x_2)} & \frac{[\bar{u}+\bar{d}+2\bar{s}](x_2)}{DIS(x_2)} & \frac{[5(u+d)](x_2)}{DIS(x_2)} \\
\\
\vdots & \vdots & \vdots & \vdots \\
\\
\frac{[2\bar{s}](x_{12})}{DIS(x_{12})} & \frac{[4(u+d)](x_{12})}{DIS(x_{12})} & \frac{[u+d+2s](x_{12})}{DIS(x_{12})} & \frac{[5(\bar{u}+\bar{d})](x_{12})}{DIS(x_{12})} \\
\frac{[2s](x_{12})}{DIS(x_{12})} & \frac{[4(\bar{u}+\bar{d})](x_{12})}{DIS(x_{12})} & \frac{[\bar{u}+\bar{d}+2\bar{s}](x_{12})}{DIS(x_{12})} & \frac{[5(u+d)](x_{12})}{DIS(x_{12})}
\end{pmatrix}
\begin{pmatrix}
\mathbf{D_{str}} \\
\\
\mathbf{D_{fav}} \\
\\
\mathbf{D_{uf1}} \\
\\
\mathbf{D_{uf2}}
\end{pmatrix},
$$

$$(5.17)$$

with $DIS(x_i) = 5[u + d + \bar{u} + \bar{d} + 2(s + \bar{s})](x_i)$.

Using the simplified model for the nucleon-quark distributions from Section 5.2 again (cf. Eq.s 5.10, 5.11, 5.12 and Fig. 5.1), the matrix in Eq. 5.17 can be rewritten as:

$$
\begin{pmatrix}
r^{K^+}(x_1) \\
r^{K^-}(x_1) \\
\\
r^{K^+}(x_2) \\
r^{K^-}(x_2) \\
\\
\vdots \\
\\
r^{K^+}(x_{12}) \\
r^{K^-}(x_{12})
\end{pmatrix}
=
\begin{pmatrix}
\frac{[2\alpha_q\bar{q}](x_1)}{DIS(x_1)} & \frac{[12q_v+8\alpha_q\bar{q}](x_1)}{DIS(x_1)} & \frac{[3q_v+4\alpha_q\bar{q}](x_1)}{DIS(x_1)} & \frac{[10\alpha_q\bar{q}](x_1)}{DIS(x_1)} \\
\frac{[2\alpha_q\bar{q}](x_1)}{DIS(x_1)} & \frac{[8\alpha_q\bar{q}](x_1)}{DIS(x_1)} & \frac{[4\alpha_q\bar{q}](x_1)}{DIS(x_1)} & \frac{[15q_v+10\alpha_q\bar{q}](x_1)}{DIS(x_1)} \\
\\
\frac{[2\alpha_q\bar{q}](x_2)}{DIS(x_2)} & \frac{[12q_v+8\alpha_q\bar{q}](x_2)}{DIS(x_2)} & \frac{[3q_v+4\alpha_q\bar{q}](x_2)}{DIS(x_2)} & \frac{[10\alpha_q\bar{q}](x_2)}{DIS(x_2)} \\
\frac{[2\alpha_q\bar{q}](x_2)}{DIS(x_2)} & \frac{[8\alpha_q\bar{q}](x_2)}{DIS(x_2)} & \frac{[4\alpha_q\bar{q}](x_2)}{DIS(x_2)} & \frac{[15q_v+10\alpha_q\bar{q}](x_2)}{DIS(x_2)} \\
\\
\vdots & \vdots & \vdots & \vdots \\
\\
\frac{[2\alpha_q\bar{q}](x_{12})}{DIS(x_{12})} & \frac{[12q_v+8\alpha_q\bar{q}](x_{12})}{DIS(x_{12})} & \frac{[3q_v+4\alpha_q\bar{q}](x_{12})}{DIS(x_{12})} & \frac{[10\alpha_q\bar{q}](x_{12})}{DIS(x_{12})} \\
\frac{[2\alpha_q\bar{q}](x_{12})}{DIS(x_{12})} & \frac{[8\alpha_q\bar{q}](x_{12})}{DIS(x_{12})} & \frac{[4\alpha_q\bar{q}](x_{12})}{DIS(x_{12})} & \frac{[15q_v+10\alpha_q\bar{q}](x_{12})}{DIS(x_{12})}
\end{pmatrix}
\begin{pmatrix}
\mathbf{D_{str}} \\
\\
\mathbf{D_{fav}} \\
\\
\mathbf{D_{uf1}} \\
\\
\mathbf{D_{uf2}}
\end{pmatrix}
$$

$$(5.18)$$

Analysing the matrix in Eq. 5.18 one realises that the third column is a linear combination of the first two columns:

$$C_3 = C_2/4 + C_1. \tag{5.19}$$

The rank of the matrix is 3, which implies that it is not possible to extract four unknown fragmentation functions. Assuming that the relations 5.10, 5.11 and 5.12 hold, any attempt

to extract more than three unknown fragmentation functions would have to rely on the difference in shape of the valence quark PDFs u_v and d_v, or sea quark PDFs $\bar{u}$, $\bar{d}$ and $\bar{s}$. Considering the shapes of these two (respectively three) distributions are very similar (cf. Fig. 5.1), this would result in an unacceptably large statistical error.

5.3 System of Equations for Pions

If the hadron type specified for Eq. 5.4 are charged pions ($\pi^+ \equiv u\bar{d}$, $\pi^- \equiv d\bar{u}$), the following twelve fragmentation functions remain: $D_u^{\pi^+}$, $D_d^{\pi^+}$, $D_s^{\pi^+}$, $D_{\bar{u}}^{\pi^+}$, $D_{\bar{d}}^{\pi^+}$, $D_{\bar{s}}^{\pi^+}$, $D_u^{\pi^-}$, $D_d^{\pi^-}$, $D_s^{\pi^-}$, $D_{\bar{u}}^{\pi^-}$, $D_{\bar{d}}^{\pi^-}$, $D_{\bar{s}}^{\pi^-}$. Assuming charge conjugation symmetry ($D_u^{\pi^+} = D_{\bar{u}}^{\pi^-}$, $D_d^{\pi^+} = D_{\bar{d}}^{\pi^-}$, ...), this number can be reduced to six.

These six remaining fragmentation functions are $D_u^{\pi^+}$, $D_d^{\pi^+}$, $D_s^{\pi^+}$, $D_{\bar{u}}^{\pi^+}$, $D_{\bar{d}}^{\pi^+}$, $D_{\bar{s}}^{\pi^+}$. They can be treated in a similar way as the ones for the charged kaons. The favoured fragmentation functions are in this case $D_u^{\pi^+}$ and $D_{\bar{d}}^{\pi^+}$. Because pions do not contain s or $\bar{s}$ valence quarks, the strange quark fragmentation functions are to be expected of the same order of magnitude as the other unfavoured fragmentation functions. It follows that all remaining fragmentation functions ($D_d^{\pi^+}$, $D_{\bar{u}}^{\pi^+}$, $D_s^{\pi^+}$, $D_{\bar{s}}^{\pi^+}$) are unfavoured and considered equal. PYTHIA simulations of pion fragmentation (Fig. 5.3 and Tab. 5.2) support that assumption. Accordingly, the pion fragmentation functions can only be divided into two groups, denoted D_{fav} and D_{unf}. The new denotations are listed in the table below:

D_{fav}	$D_u^{\pi^+} \equiv D_{\bar{u}}^{\pi^-}$, $D_{\bar{d}}^{\pi^+} \equiv D_d^{\pi^-}$
D_{unf}	$D_d^{\pi^+} \equiv D_{\bar{d}}^{\pi^-}$, $D_{\bar{u}}^{\pi^+} \equiv D_u^{\pi^-}$
	$D_s^{\pi^+} \equiv D_{\bar{s}}^{\pi^-}$, $D_{\bar{s}}^{\pi^+} \equiv D_s^{\pi^-}$

Using these new definitions and assuming a deuteron target, the pion multiplicities can be expressed by the following equations:

$$r^{\pi^+} = \frac{4[(u+d) + \bar{u} + \bar{d}]\mathbf{D_{fav}} + [u + d + 4(\bar{u} + \bar{d}) + 2s + 2\bar{s}]\mathbf{D_{unf}}}{5(u + d + \bar{u} + \bar{d} + 2(s + \bar{s}))} \qquad (5.20)$$

$$r^{\pi^-} = \frac{4[(\bar{u} + \bar{d}) + u + d]\mathbf{D_{fav}} + [4(u + d) + \bar{u} + \bar{d} + 2s + 2\bar{s}]\mathbf{D_{unf}}}{5(u + d + \bar{u} + \bar{d} + 2(s + \bar{s}))}. \qquad (5.21)$$

As for the kaon multiplicities Eq.s 5.20 and 5.21 can be written in bins of x to allow the extraction of the fragmentation functions:

$$
\begin{pmatrix}
r^{K^+}(x_1) \\
r^{K^-}(x_1) \\[4pt]
r^{K^+}(x_2) \\
r^{K^-}(x_2) \\[4pt]
\vdots \\[4pt]
r^{K^+}(x_{12}) \\
r^{K^-}(x_{12})
\end{pmatrix}
=
\begin{pmatrix}
b_{1,1} & b_{1,2} \\
b_{2,1} & b_{2,2} \\[4pt]
b_{3,1} & b_{3,2} \\
b_{4,1} & b_{4,2} \\[4pt]
\vdots & \vdots \\[4pt]
b_{23,1} & b_{23,2} \\
b_{24,1} & b_{24,2}
\end{pmatrix}
\begin{pmatrix}
\mathbf{D_{fav}} \\[12pt]
\mathbf{D_{unf}}
\end{pmatrix}.
\tag{5.22}
$$

The entries $b_{i,i}$ of the matrix contain the linear combinations of the unpolarised PDFs according to Eq.s 5.20 and 5.20:

$$
\begin{pmatrix}
r^{\pi^+}(x_1) \\
r^{\pi^-}(x_1) \\[4pt]
r^{\pi^+}(x_2) \\
r^{\pi^-}(x_2) \\[4pt]
\vdots \\[4pt]
r^{\pi^+}(x_{12}) \\
r^{\pi^-}(x_{12})
\end{pmatrix}
=
\begin{pmatrix}
\frac{[4(u+d)+\bar{u}+\bar{d}](x_1)}{DIS(x_1)} & \frac{[u+d+4(\bar{u}+\bar{d})+2s+2\bar{s}](x_1)}{DIS(x_1)} \\
\frac{[4(\bar{u}+\bar{d})+u+d](x_1)}{DIS(x_1)} & \frac{[\bar{u}+\bar{d}+4(u+d)+2s+2\bar{s}](x_1)}{DIS(x_1)} \\[6pt]
\frac{[4(u+d)+\bar{u}+\bar{d}](x_2)}{DIS(x_2)} & \frac{[u+d+4(\bar{u}+\bar{d})+2s+2\bar{s}](x_2)}{DIS(x_2)} \\
\frac{[4(\bar{u}+\bar{d})+u+d](x_2)}{DIS(x_2)} & \frac{[\bar{u}+\bar{d}+4(u+d)+2s+2\bar{s}](x_12)}{DIS(x_2)} \\[6pt]
\vdots & \vdots \\[6pt]
\frac{[4(u+d)+\bar{u}+\bar{d}](x_{12})}{DIS(x_{12})} & \frac{[u+d+4(\bar{u}+\bar{d})+2s+2\bar{s}](x_{12})}{DIS(x_{12})} \\
\frac{[4(\bar{u}+\bar{d})+u+d](x_{12})}{DIS(x_{12})} & \frac{[\bar{u}+\bar{d}+4(u+d)+2s+2\bar{s}](x_{12})}{DIS(x_{12})}
\end{pmatrix}
\begin{pmatrix}
\mathbf{D_{fav}} \\[12pt]
\mathbf{D_{unf}}
\end{pmatrix},
\tag{5.23}
$$

with $DIS(x_i) = 5[u + d + \bar{u} + \bar{d} + 2(s + \bar{s})](x_i)$.

Using again the simplified model of the nucleon quark distribution (see Eq.s 5.10, 5.11 and 5.12 and Figure 5.1), this matrix can be re-written as:

$$
\begin{pmatrix}
r^{\pi^+}(x_1) \\[4pt]
r^{\pi^-}(x_1) \\[14pt]
r^{\pi^+}(x_2) \\[4pt]
r^{\pi^-}(x_2) \\[14pt]
\vdots \\[14pt]
r^{\pi^+}(x_{12}) \\[4pt]
r^{\pi^-}(x_{12})
\end{pmatrix}
=
\begin{pmatrix}
\frac{[12q_v+10\alpha_q\bar{q}](x_1)}{DIS(x_1)} & \frac{[3q_v+14\alpha_q\bar{q}](x_1)}{DIS(x_1)} \\[8pt]
\frac{[3q_v+10\alpha_q\bar{q}](x_1)}{DIS(x_1)} & \frac{[12q_v+14\alpha_q\bar{q}](x_1)}{DIS(x_1)} \\[14pt]
\frac{[12q_v+10\alpha_q\bar{q}](x_2)}{DIS(x_2)} & \frac{[3q_v+14\alpha_q\bar{q}](x_2)}{DIS(x_2)} \\[8pt]
\frac{[3q_v+10\alpha_q\bar{q}](x_2)}{DIS(x_2)} & \frac{[12q_v+14\alpha_q\bar{q}](x_1 2)}{DIS(x_2)} \\[14pt]
\vdots & \vdots \\[14pt]
\frac{[12q_v+10\alpha_q\bar{q}](x_{12})}{DIS(x_{12})} & \frac{[3q_v+14\alpha_q\bar{q}](x_{12})}{DIS(x_{12})} \\[8pt]
\frac{[3q_v+10\alpha_q\bar{q}](x_{12})}{DIS(x_{12})} & \frac{[12q_v+14\alpha_q\bar{q}](x_{12})}{DIS(x_{12})}
\end{pmatrix}
\begin{pmatrix}
\mathbf{D_{fav}} \\[20pt]
\mathbf{D_{unf}}
\end{pmatrix}.
\tag{5.24}
$$

The rank of the matrix containing the unpolarised PDFs is two, therefore the system of equations can be solved for the two unknown fragmentation functions.

Figure 5.3 shows PYTHIA simulated pion fragmentations, the respective values for $\int_{0.2}^{1} D_q^h(z)$ are listed in Table 5.2.
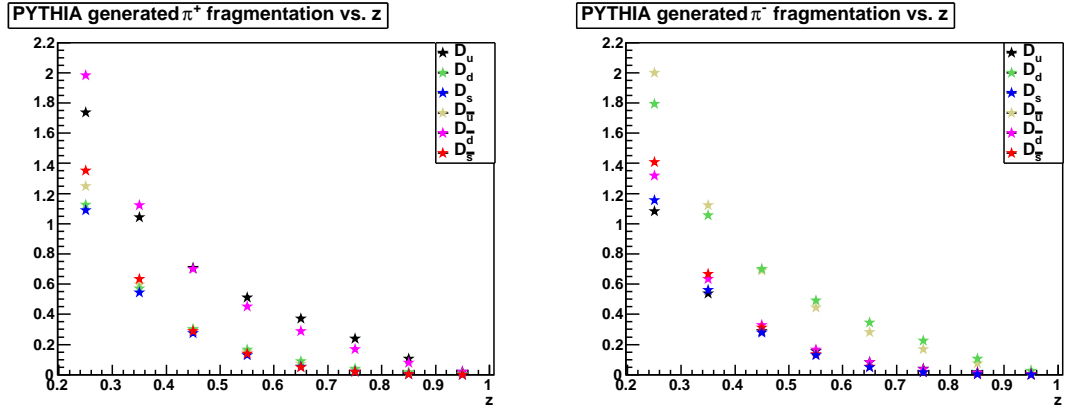
Figure 5.3: Pion fragmentation functions generated with PYTHIA [53]. The fragmentation functions are plotted in eight z bins, with a bin width of $dz = 0.1$.

quark q	hadron h	$\int_{0.2}^{1} D_q^h(z)$	quark q	hadron h	$\int_{0.2}^{1} D_q^h(z)$
$\bar{d}$	π^+	0.486	d	π^-	0.479
u	π^+	0.468	$\bar{u}$	π^-	0.474
d	π^+	0.256	$\bar{d}$	π^-	0.251
$\bar{s}$	π^+	0.248	s	π^-	0.245
s	π^+	0.226	$\bar{s}$	π^-	0.227
$\bar{u}$	π^+	0.217	u	π^-	0.214

Table 5.2: Expected values for the pion fragmentation functions from a PYTHIA [53] simulation.

5.4   Multiplicities

The pion and kaon multiplicities used in this analysis have been extracted from COMPASS data collected in 2004 by deep-inelastic scattering of muons off a deuteron (^{6}LiD) target [39].

The multiplicities are shown in Fig. 5.4 as a function of x in four z bins ([0.2, 0.3], [0.3, 0.45], [0.45, 0.65], [0.65, 0.85]). They are compared to theoretical predictions, which have been calculated using the LO definition of hadron multiplicities:

$$\frac{1}{\sigma^{incl}(x, Q^2)} \frac{d\sigma^h(x, Q^2, z)}{dx dQ^2 dz} = \frac{\sum_q e_q^2 q(x, Q^2 D_q^h(z, Q^2))}{\sum_q e_q^2 q(x, Q^2)}, \tag{5.25}$$

the LO DSS parametrisation [26] for fragmentation functions and the LO MRST 2004 parametrisation [25] for unpolarised parton distribution functions. The MRST parametrisation was chosen because of its validity in the kinematic range of COMPASS. The PDFs have been evaluated in every x bin, at the mean values of x and Q^2 in that bin. The fragmentation functions have been evaluated at the mean value of Q^2 and integrated over z in each interval. Both the experimental multiplicities and theoretical predictions are plotted at the mean value of x in each bin of x and z.

The charged kaon multiplicities (Fig. 5.4, bottom) increase (K^+), respectively decrease (K^-), with x in nearly all regions of z, a tendency that is more pronounced in the high z bins. Both multiplicities agree with the LO predictions in the low x region only, but deviate from the theoretical curves significantly for larger x.

These discrepancies might be explained by higher order corrections missing in the LO definition of hadron multiplicities (see Eq. 5.25), or by the poor knowledge of the strange quark distributions and strange quark fragmentation functions. Figure 5.5 (left) shows s quark PDFs from various parametrisations. They show significant differences in all x regions.

The knowledge of strange quark fragmentation functions is limited to parametrisations using a number of assumptions (see Chapter 2); and there has been only one attempt to measure them experimentally as of now [39].
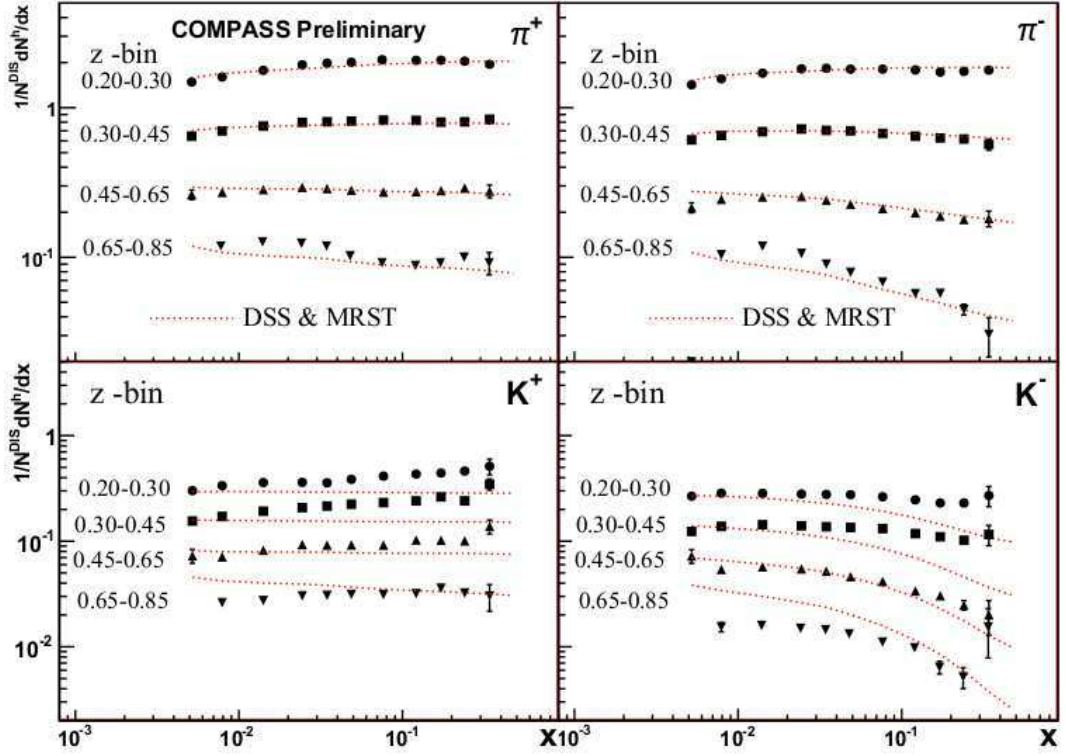
Figure 5.4: Charged pion (π^+ and π^-)and kaon (K^+ and K^-) multiplicities extracted from COMPASS data as a function of x in four z bins, compared to LO theoretical calculations using the LO DSS for FFs and the LO MRST 2004 for PDFs [39]

Nonetheless, the large number of negatively charged kaons for large x (Fig. 5.4, bottom left) does seem to contradict all knowledge of the fragmentation process. While the favoured u quark fragmentation function, $D_{\bar{u}}^{K^-}$, is the second largest fragmentation function for kaons, it should decrease strongly with increasing x, corresponding to the decreasing number of available $\bar{u}$ quarks at large x (see Fig. 5.5 (right)).

The charged pion multiplicities (Fig. 5.4, top) show a weak x dependence in high z bins, confirming the theoretical predictions. Both show some discrepancies in the highest z bin, $0.65 < z < 0.85$, however.
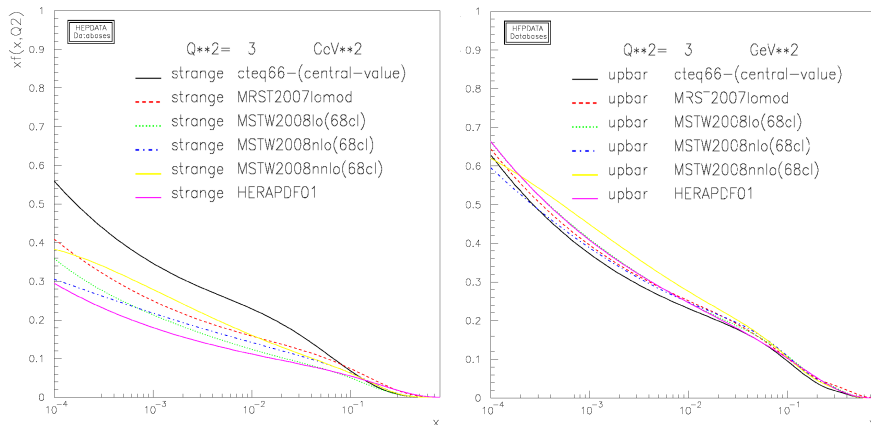
Figure 5.5: Strange quark (left) and anti-up quark (right) distributions from various parametrisations [52]

5.5   Unpolarised Parton Distribution Functions

The method of extraction of fragmentation functions is based on the LO definition of hadron multiplicities (cf. Eq. 5.2). Owing to that two different LO parametrisations of parton distributions have been used as input in the calculations, CTEQ6l, and MSTW2008-LO.

5.5.1   CTEQ6

CTEQ[2] [54, 55] is a programme for the determination of parton distributions through a global QCD analysis of data for various hard scattering processes. The global analysis of the CTEQ group has two goals: Firstly, trying to find a universal set of parton distributions which provide an accurate description of all of the used sets of data and can therefore be utilised in the calculation of other high energy processes. Secondly, a determination of the degree in which the theoretical treatment of the hard scattering processes in the QCD framework is consistent with the available experimental results.

The experimental input includes data from various DIS experiments measuring different

---

[2]CTEQ: The Coordinated Theoretical-Experimental Project on QCD

nucleon structure functions, e.g. NMC[3] [56], CCFR[4] [56] [57], BCDMS[5] [58], E605 [59], CDF[6], Na51 [60] and others.

5.5.2 MSTW

The MSTW[7] [61] collaboration is dedicated to the determination of leading order, next-to-leading order and next-to-next-to-leading order parton distribution functions from global analysis of hard-scattering data. These parton distributions supersede the previously available MRST sets.

The new data sets fitted include CCFR/NuTeV[8] [62] dimuon cross sections, which constrain the strange quark and antiquark distributions, as well as Tevatron and HERA[9] jet data.

5.6 Testing the Method of Extraction

The systems of equations derived above (cf. Sections 5.2 and 5.3) were tested by assuming fragmentation functions in the order of magnitude of the PYTHIA results (cf. Table 5.1). Using these artificial fragmentation functions and CTEQ6 parton distribution functions, multiplicities were calculated using Eq. 5.7. These multiplicities were then used to extract fragmentation functions for two sets of parton distribution functions. (For a detailed description of the calculation method consult Appendix A.) The first set used was again taken from the CTEQ6 parametrisation, while for the second calculation MSTW parton distribution functions were employed. Solving the system for the CTEQ6 PDFs, the initially injected fragmentation functions were extracted. The use of MSTW PDFs yielded slightly differing results, most notably for the strange fragmentation function. The test results for kaon fragmentation functions are listed below:

$x \int_{0.2}^{0.85} D$	CTEQ PDFs	MSTW PDFs
D_{str}	0.300	0.260
D_{fav}	0.100	0.102
D_{unf}	0.030	0.030
R_{SF}	3.000	2.449
R_{UF}	0.300	0.294

---

[3]NMC: New Muon Collaboration
[4]CCFR: Chicago Columbia Fermilab Rochester Collaboration
[5]BCDMS: Bologna CERN Dubna Munich Saclay
[6]CDF: Collider Detector at Fermilab
[7]MSTW: A.D. Martin, W.J. Stirling, R.S. Thorne, G. Watt
[8]NuTeV: Neutrinos at the Tevatron
[9]HERA: Hadron-Electron Ring Accelerator

5.7   Use of the Unpolarised PDFs and Hadron Multiplicities

The fragmentation functions for charged kaons and pions were evaluated in each of the four z intervals [0.2, 0.3], [0.3, 0.45], [0.45, 0.65], [0.65, 0,85] separately, integrated over the width of the z bin.

The values of the parton distribution functions used in the analysis (CTEQ6l [54] and MSTW2008-LO [61]) were retrieved at the mean value of Q^2 corresponding to the x interval at COMPASS energies. Table 5.3 lists the values of Q^2 for each x; they are plotted in Fig. 5.6.
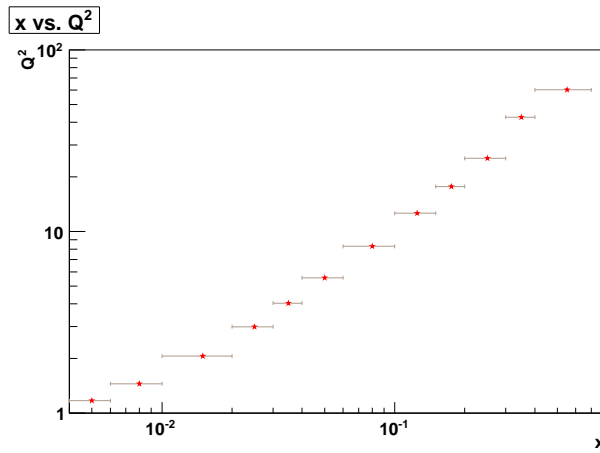
Figure 5.6: The mean values of Q^2 for the x intervals used in the analysis, cf. Tab. 5.3

The COMPASS kaon and pion multiplicities for each of the twelve x bins, four z intervals and two charges were used including their statistical and systematical errors; all are listed in Tables C.1, C.2 (pions) and C.3, C.4 (kaons) in Appendix C.

x	Q^2	x	Q^2	x	Q^2
[0.004, 0.006]	1.17	[0.03, 0.04]	4.03	[0.15, 0.2]	17.70
[0.006, 0.01]	1.45	[0.04, 0.06]	5.56	[0.2, 0.3]	25.30
[0.01, 0.02]	2.06	[0.06, 0.1]	8.29	[0.3, 0.4]	42.60
[0.02, 0.03]	2.99	[0.1, 0.15]	12.60	[0.4, 0.7]	60.20

Table 5.3: The average Q^2 for various x ranges

Figure 5.7 shows the evolution of both the CTEQ6 and the MSTW parton distribution functions for $u, d, \bar{u}, \bar{d}$ and s quarks with increasing values of Q^2 (1, 10 and $100\,(\text{GeV/c})^2$), and in Fig. 5.8 the CTEQ6 PDFS are plotted as a function of x, at the Q^2 value corresponding to each x interval.
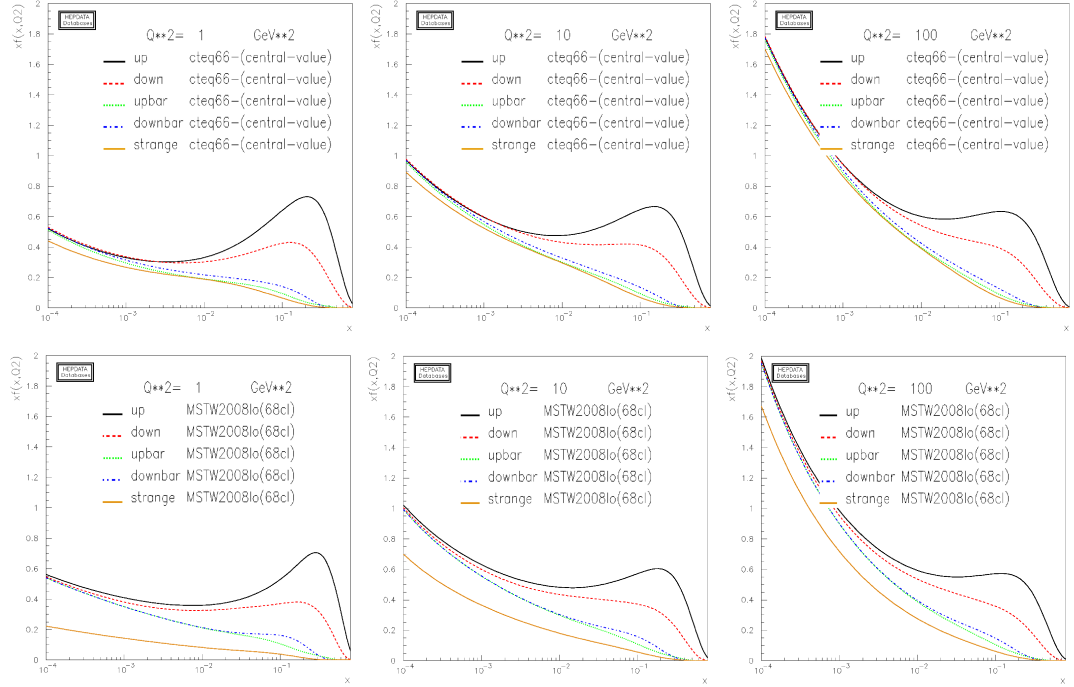
Figure 5.7: The evolution of the unpolarised parton distribution functions for u (black), d (red dashed), $\bar{u}$ (green dotted), $\bar{d}$ (blue dashed dotted), and s (yellow) quarks with increasing Q^2, for CTEQ6 (top) and MSTW (bottom) PDFs, plotted against x for Q^2 = 1, 10 and 100 $(\text{Gev/c})^2$ [52]
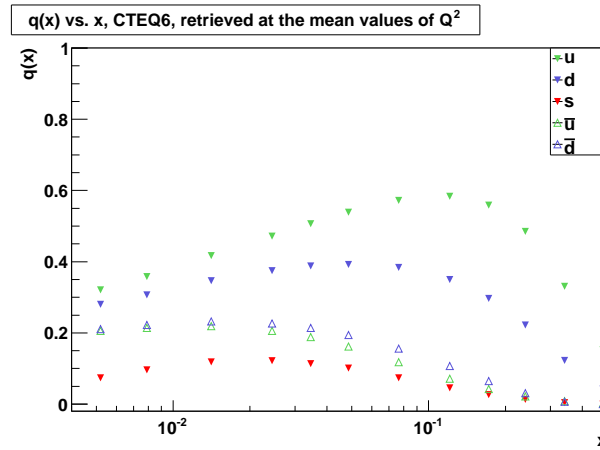
Figure 5.8: The CTEQ6 parton distribution functions, plotted against x. The PDFs were retrieved at the mean value of Q^2 corresponding to the x interval at COMPASS energies.

Chapter 6

Results for Pion and Kaon Fragmentation Functions

In the previous chapter the method of extraction of fragmentation functions from hadron multiplicities was developed. Systems of equations for charged kaon and pion FFs were derived and tested, and the data used for extraction was introduced. This chapter will present and discuss the results for the extracted fragmentation functions. The pion FFs have been determined before by other experiments; they will serve as a test case here. The results for charged pions are presented first, followed by the ones for charged kaons.

6.1   Results for the Pion Fragmentation Functions

The charged pion fragmentation functions were extracted in four bins of z, using two versions of unpolarised PDFs (CTEQ6 and MSTW, cf. Section 5.5) and the full set of pion multiplicities available (cf. Tables C.1 and C.2 in Appendix C and Section 5.4). The method of extraction and the calculation of the uncertainties are described in detail in Chapter 5 and Appendix A.

To test the influence of uncertainties of the multiplicities and the validity of the factorisation assumption (cf. Section 2.2.2), the analysis was performed again using only pion multiplicities from limited ranges of x. This section presents and discusses the results.

6.1.1   Pion Fragmentation Functions for $0.004 < x < 0.7$

The pion fragmentation functions D_{fav} and D_{unf} extracted using the full set of multiplicities are listed in Table B.1 and plotted in Fig. 6.1.

The results for both the favoured and the unfavoured pion fragmentation functions show very little dependence on the unpolarised parton distribution used in the calculation. The

difference due to the disparity of the two PDFs is less than 3% in all intervals of z. Only in the largest z bin it increases to 6% for D_{fav} and 12% for D_{unf}. The uncertainty is of the same order of magnitude over the whole z range for both FFs. Within their margin of error the results for both sets of unpolarised PDFs agree very well for the two extracted fragmetation functions.
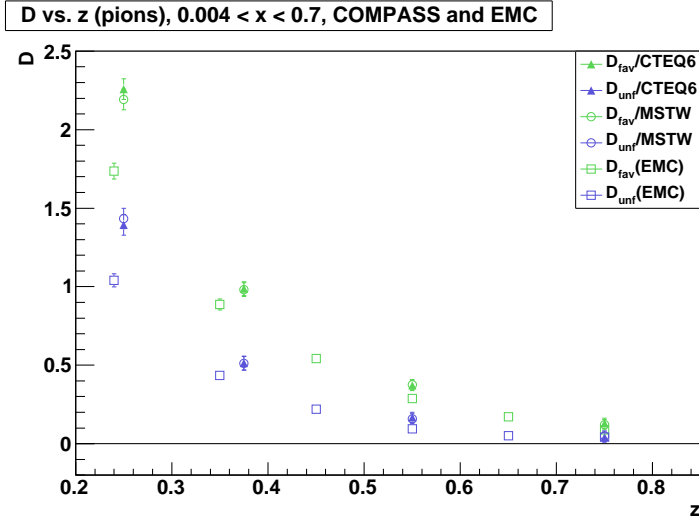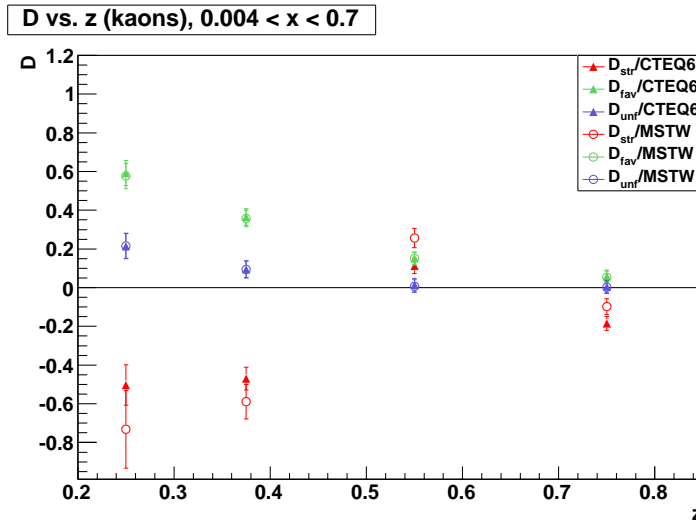

Figure 6.1: The extracted kaon fragmentation functions D_{fav} (green) and D_{unf} (blue) for $0.004 < x < 0.07$, plotted against z. The full triangles mark the fragmentation functions extracted with CTEQ6 parton distribution functions, the open circles the ones extracted by using the MSTW parton distributions. The errors shown are statistical and systematical uncertainties combined (cf. Table B.1).

6.1.2   Pion Fragmentation Functions for $0.006 < x < 0.4$

The pion multiplicities used for this analysis show rather large uncertainties as well as missing data points in the smallest ($0.004 < x < 0.006$) and the largest ($0.3 < x < 0.7$) bins of x (cf. Tables C.1 and C.2 in Appendix C and Fig. 5.4). Even though data points with large errors are given little weight in the calculation (cf. Section A.1) it is worth exploring how these deficiencies influence the calculation. For this reason the pion FFs were extracted again, this time using only the ten 'middle' x bins ($0.006 < x < 0.3$).

The resulting values for the charged pion fragmentation functions are listed in Table B.2 and plotted in Fig. 6.2.

The differences in the fragmentation functions due to the different sets of unpolarised parton distributions are minimal. Similar to the values calculated using the full x range there are very slight differences between fragmentation functions extracted with the MSTW and the CTEQ PDFs in the first and last z bin, but within their error bars they agree very well.
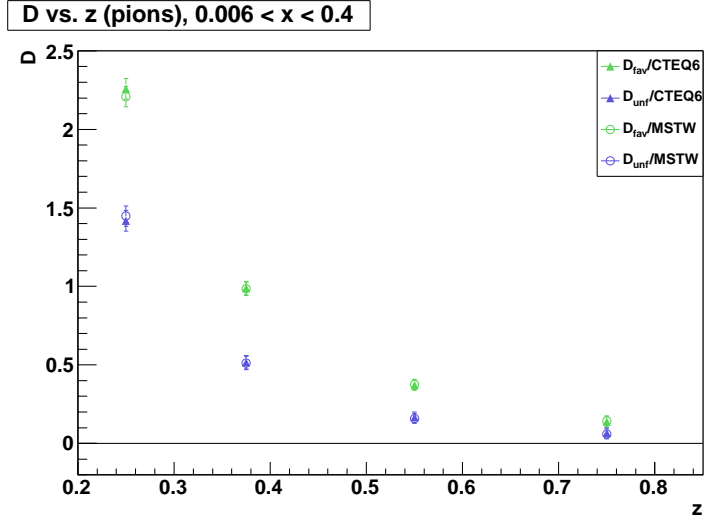
Figure 6.2: The extracted pion fragmentation functions D_{fav} and D_{unf} for $0.006 < x < 0.4$, plotted against z. The full triangles mark the fragmentation functions extracted with CTEQ6 parton distribution functions, the open circles the ones extracted by using the MSTW parton distributions. The errors shown are statistical and systematical uncertainties combined (cf. Table B.2).

The comparison of the extracted values with the ones including all x bins reveals virtually no change for either of the fragmentation functions in any of the four z intervals.

It appears that inclusion of the outer x bins, and with that the inclusion of the uncertainties and missing data points from the multiplicities does have little influence the extracted values.

6.1.3 Test for Split x Range

The x dependence of hadron multiplicities can be used to test the factorisation assumption which states that the fragmentation of a quark is independent of the initial scattering event from which it originates (cf. Section 2.2.2). If the factorisation holds, the fragmentation functions must be independent of x, and the x dependence of the hadron multiplicities is a result of the x dependence of the parton distribution functions alone. For this purpose, the twelve intervals of x of the pion multiplicities used in this analysis have been divided into two parts. The lower six x bins cover the interval $[0.004, 0.06]$, the upper six the interval $[0.06, 0.7]$. The fragmentation functions were again calculated, using twelve multiplicities (for six x bins and two charges) as input twice, once for the lower and once for the higher x range. The results are listed in Tables B.3 and B.4 and plotted in Fig. 6.3.

Both D_{fav} and D_{unf} show very little change due to the different x ranges used in the analysis. Almost all extracted values agree with the ones for the full set of multiplicities within their margin of error, with only two exceptions.
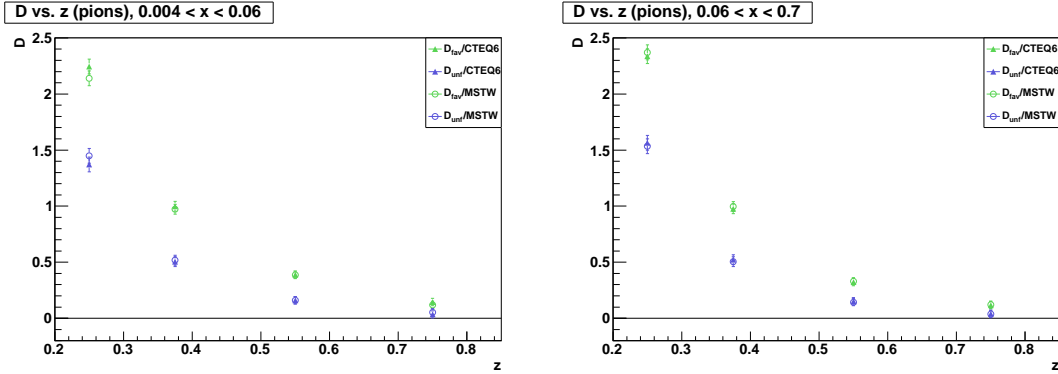
Figure 6.3: The extracted pion fragmentation functions D_{fav} (green) and D_{unf} (blue) for $0.004 < x < 0.06$ (left) and $0.06 < x < 0.7$ (right), plotted against z. The full triangles mark the fragmentation functions extracted with CTEQ6 parton distribution functions, the open circles the ones extracted by using the MSTW parton distributions. The errors shown are statistical and systematical uncertainties combined (cf. Tables B.3 and B.4).

The analysis for the lower x range shows very little effect on both fragmentation functions, only a very slight increase for D_{fav} and decrease for D_{unf} (less than 2%) in almost all z intervals for the CTEQ values and the opposite for the MSTW results. The effects of the use of the higher x range on the extracted values are a slightly stronger; both D_{unf} extracted with the CTEQ parton distribution and D_{fav} extracted with the MSTW PDFs increase by more than 10% in the lowest z bin, and do not agree with the values extracted with the full set of multiplicities. Again the MSTW and CTEQ calculations show the opposite effect.

In conclusion, the use of different intervals of x for the analysis does not appear to have a significant influence on the results for pion fragmentation functions.

6.1.4   Conclusions

The pion fragmentation functions D_{fav} and D_{unf} have been extracted, using two sets of unpolarised parton distribution functions, and the full set of pion multiplicities available, as well as multiplicities for a limited range of x. The FFs appear to be quite stable with regard to the parton distribution used in the calculation as well as to the x range in which the analysis was conducted.

6.2   Results for the Kaon Fragmentation Functions

Like the pion fragmentation functions, the kaon FFs were extracted multiple times. (For details on the method of extraction consult Chapter 5 and Appendix A.) After using the

full set of kaon multiplicities (cf. Tables C.3 and C.4 in Appendix C and Section 5.4) available, the analysis was performed again for a limited range of x. The factorisation assumption was tested by splitting the full range of x into two sub-intervals and extracting the fragmentation functions for the low and the high x bins separately. This section presents and discusses the results.

6.2.1 Kaon Fragmentation Functions for $0.004 < x < 0.7$

The kaon fragmentation functions extracted using the full set of charged kaon multiplicities are listed in Table B.5 and plotted in Fig. 6.4.
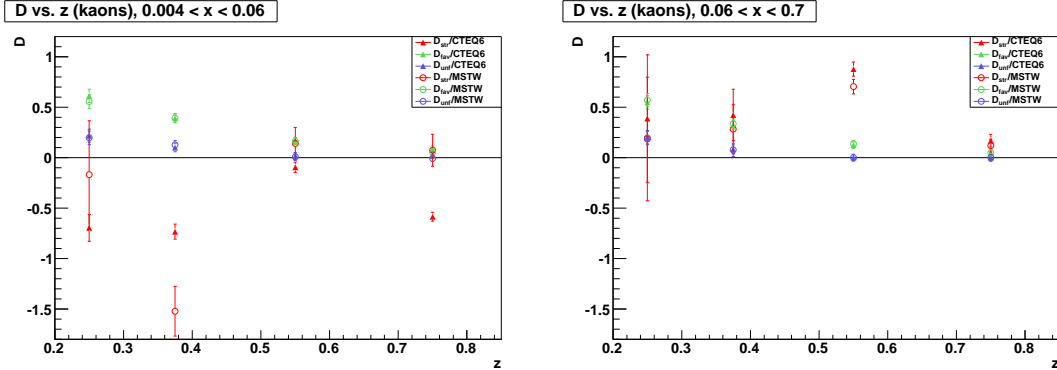

Figure 6.4: The extracted kaon fragmentation functions D_{str} (red), D_{fav} (green) and D_{unf} (blue) for $0.004 < x < 0.7$ plotted against z. The full triangles mark the fragmentation functions extracted with CTEQ6 parton distribution functions, the open circles the ones extracted by using the MSTW parton distributions The errors shown are statistical and systematical uncertainties combined (cf. Table B.5).

The results for the D_{fav} and the D_{unf} fragmentation functions show little dependence on the parton distributions used in the analysis. While the CTEQ PDFs result systematically in slightly larger values for the two fragmentation functions, the difference is very small. Within their margin of error both D_{fav} and the D_{unf} agree very well for both sets of PDFs.

The values for D_{fav} agree within 2% in all z bins, as does their integral over all z intervals [0.2, 0.8]. The same applies to D_{unf}; the extracted values are in very good agreement in all bins of z, with only a slightly bigger difference in the third interval. Both the favoured and unfavoured fragmentation functions have the same errors for the CTEQ and MRST parton distributions.

The results for the strange quark fragmentation function on the other hand are less consistent and adopt unphysical values in nearly every bin of z. In the first two z intervals large negative values for D_{str} are extracted for both sets of parton distribution functions. The errors in these z bins are large, especially so for the MSTW PDFs.

The D_{str} values for the larger z have smaller uncertainties, but still larger than the ones for the favoured and unfavoured fragmentation functions in the same z intervals. The values themselves are larger than zero in the third bin and negative again in the fourth. The strange quark fragmentation function remains well below the theoretical expectations (cf. Section 5.2.1) over the whole range of z. The extracted D_{str} values for the CTEQ and MSTW parton distributions do not agree with each other in three of the four z bins.

The fragmentation function ratio $R_{SF} = \int_{0.2}^{0.85} D_{str} / \int_{0.2}^{0.85} D_{fav}$ (cf. Eq. 2.61) calculated from these results is also negative and unphysical, regardless of the unpolarised PDF used in the calculations.

$$R_{SF}^{CTEQ6} = -0.870 \pm 0.038$$
$$R_{SF}^{MSTW} = -0.852 \pm 0.106$$

The ratio $R_{UF} = \int_{0.2}^{0.85} D_{unf} / \int_{0.2}^{0.85} D_{fav}$ takes on the values 0.26 ± 0.10 for the CTEQ and 0.25 ± 0.11 for the MSTW parton distributions, respectively, and falls in-between the corresponding values calculated from the EMC ($R_{UF}^{EMC} = 0.36$) and DSS ($R_{UF}^{DSS} = 0.13$) results (cf. Section 4.4).

$$R_{UF}^{CTEQ6} = 0.256 \pm 0.105$$
$$R_{UF}^{MSTW} = 0.247 \pm 0.107$$

6.2.2   Kaon Fragmentation Functions for $0.01 < x < 0.3$

Even more so than the pion multiplicities the kaon multiplicities used for this analysis show large uncertainties and missing data points in the outer x intervals, especially in the first two ($0.004 < x < 0.01$) and last two ($0.3 < x < 0.7$) bins of x (cf. Tables C.3, C.4 in Appendix C and Fig. 5.4).

To test how these uncertainties influence the results, and if they possibly are responsible for the unphysical values of the extracted strange quark fragmentation functions in the lower z intervals, the above analysis was performed again, this time using only the eight 'middle' x bins ($0.01 < x < 0.3$). The resulting values for the fragmentation functions are listed in Table B.6 and plotted in Fig. 6.5.

The results for the favoured and unfavoured fragmentation functions show very little change. The values for D_{fav} are slightly smaller (about 2%) for the CTEQ parton distributions and slightly larger (about 1%) for the MSTW parton distributions, compared to

the calculations using the multiplicities for the whole x range. The unfavoured fragmentation functions decrease by up to 4% for both sets of parton distributions. Within their (slightly increased) error bars both D_{fav} and D_{unf} remain virtually unchanged.
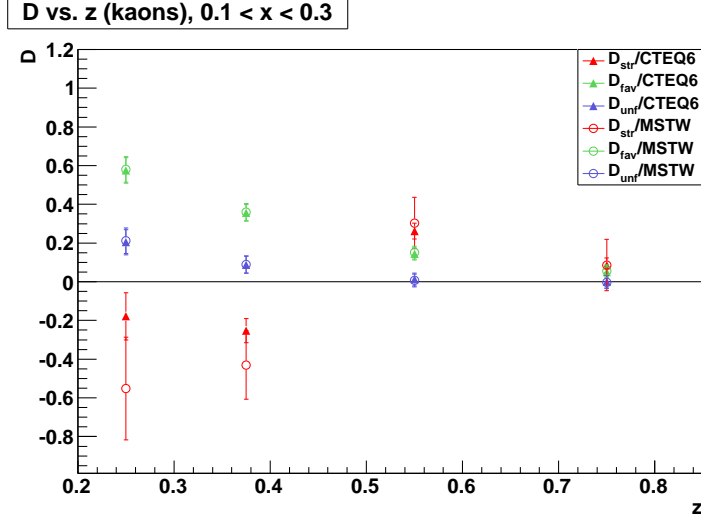
Figure 6.5: The extracted kaon fragmentation functions D_{str} (red), D_{fav} (green) and D_{unf} (blue) for $0.1 < x < 0.3$, plotted against z. The full triangles mark the fragmentation functions extracted with CTEQ6 parton distribution functions, the open circles the ones extracted by using the MSTW parton distributions. The errors shown are statistical and systematical uncertainties combined (cf. Table B.6).

The strange fragmentation function increases strongly for both sets of parton distributions, but still remains negative in all but one of the z bins. The uncertainty of D_{str} increases as well (in most bins of z by more than a factor 2), especially for the MSTW calculations. For both sets of parton distributions the strange quark fragmentation function is much smaller than expected or physically possible.

The large uncertainty of the fragmentation function ratio R_{SF} calculated from these results allows for values larger than zero for both parton distributions, but still remains much smaller than the ratios from the EMC and DSS parametrisations (3.4 and 6.6, respectively, cf. Section 4.4):

$$R_{SF}^{CTEQ6} = -0.002 \pm 0.216$$
$$R_{SF}^{MSTW} = -0.273 \pm 0.323.$$

The ratio R_{UF} decreases slightly for both parton distribution functions compared to the values obtained using the multiplicities for the full x range:

$$R_{UF}^{CTEQ6} = 0.242 \pm 0.108$$
$$R_{UF}^{MSTW} = 0.231 \pm 0.106.$$

In conclusion, it can be assumed that the uncertainties and missing data points in the outer x bins of the COMPASS multiplicities are not responsible for the unphysical results obtained using the full x range (cf. Section 6.2.1).

These results do, however, raise the question if the factorisation assumption of hadron fragmentation can be trusted in this case.

6.2.3   Test for Split x Range

Like for the pion fragmentation functions (cf. Section 6.1.3), the factorisation assumption is tested by splitting the twelve x intervals for the multiplicities into two parts. The lower six x bins cover the interval [0.004, 0.06], the upper six the interval [0.06, 0.7]. The pion fragmentation functions were again calculated, using twelve multiplicities (for six x bins and two charges) as input, for the lower and the higher x range, respectively. The results are listed in Tables B.7 and B.8 and plotted in Figure 6.6.

Figure 6.6: The extracted charged kaon fragmentation functions D_{str} (red), D_{fav} (green) and D_{unf} (blue) for $0.004 < x < 0.06$ (left) and $0.06 < x < 0.7$ (right), plotted against z. The full triangles mark the fragmentation functions extracted with CTEQ6 parton distribution functions, the open circles the ones extracted by using the MSTW parton distributions. The errors shown are statistical and systematical uncertainties combined (cf. Tables B.7 and B.8).

The values for the favoured fragmentation function (CTEQ parton distributions) increase for the lower x intervals, compared to the extraction using the whole available x range, especially for the larger z bins. The opposite effect can be observed for the second analysis using the multiplicities in the higher x range. D_{fav} (MSTW PDFs) shows a similar

behaviour, although it does not increase in all z intervals for the low x range. All these effects are more pronounced for high z intervals.

The unfavoured fragmentation function increases for the smaller x range, especially for the analysis using the CTEQ PDFs as input. For the interval $0.06 < x < 0.3$ D_{unf} decreases; this effect is stronger for the MSTW parton distribution.

Uniformly, for larger x both the favoured and the unfavoured fragmentation function values decrease, especially for larger z, regardless of the parton distributions used for the analysis. For the lower x range both D_{fav} and D_{unf} increase for the calculations using the CTEQ parton distributions as input, the MSTW values decrease or increase, depending on the z interval. There's no change in the uncertainties for any of the favoured or unfavoured fragmentation functions.

Overall, both D_{fav} and D_{unf} show only little change. Both still agree within their margin of error for the higher and the lower x range, and also with the fragmentation functions extracted using the full set of the measured multiplicities.

Accordingly, the values of the ratio R_{UF} agree with the ones calculated for the full x range. R_{UF} decreases for the fragmentation functions extracted using the larger x bins from 0.26 to 0.24 and from 0.25 to 0.22 for the CTEQ and the MRST parton distributions respectively. For smaller x R_{UF} increases slightly, most notably for the CTEQ PDFs (from 0.26 to 0.27).

$$(\text{for } 0.004 < x < 0.06)$$
$$R_{UF}^{CTEQ6} = 0.268 \pm 0.097$$
$$R_{UF}^{MSTW} = 0.246 \pm 0.105$$

$$(\text{for } 0.06 < x < 0.7)$$
$$R_{UF}^{CTEQ6} = 0.243 \pm 0.119$$
$$R_{UF}^{MSTW} = 0.216 \pm 0.110$$

The strange fragmentation function values decrease or increase, depending on the x range of the multiplicities, the parton distribution functions used and the z interval, with no recognisable pattern. Especially for the MSTW parton distributions and small z bins the errors are strongly increased (by more than a factor of 2) in comparison with the results for the full x range. The values of D_{str} do not agree within their margin of error for either of the intervals of x used in the analysis. For $0.004 < x < 0.06$ D_{str} is negative in all z bins, resulting in large negative values for R_{SF}. For $0.06 < x < 0.3$ D_{str} is positive in all intervals of z. Consequently, R_{SF} is large and positive for this x range.

$$(\text{for } 0.004 < x < 0.06)$$
$$R_{SF}^{CTEQ6} = -1.859 \pm 0.013$$
$$R_{SF}^{MSTW} = -1.285 \pm 0.394$$

$$(\text{for } 0.06 < x < 0.7)$$
$$R_{SF}^{CTEQ6} = 2.275 \pm 0.775$$
$$R_{SF}^{MSTW} = 1.560 \pm 0.654$$

While the values for R_{SF} for large x are physically possible (but still smaller that the DSS and EMC results both), the behaviour of the D_{str} values as a function of both x and z suggest that this is pure coincidence.

6.2.4   Conclusions

The kaon fragmentation functions D_{fav}, D_{unf} and D_{str} have been extracted, using two sets of unpolarised parton distribution functions, and the full set of pion multiplicities available, as well as multiplicities for a limited range of x. The favoured and unfavoured kaon FFs are quite stable with regard to the parton distribution used, as well as to the x interval in which the analysis was performed, and - in order of magnitude - fall between the results of the EMC and the DSS parametrisation.

The extracted values for D_{str} on the other hand tend to differ by a large amount, depending on the unpolarised PDFs used in the analysis, and especially with regard to the x range of multiplicities. They are often negative, and therefore physically impossible. These results cast serious doubts on this method of extraction, and therefore on the validity of the factorisation assumption, at least for strange quarks.

It is also possible that the problems with the extraction of D_{str} are related to other issues, e.g. the data used as input for the equations. Both the multiplicities and the parton distributions contain diverse uncertainties, in particular for very large and very small x.

For $0.004 < x < 0.02$ the various unpolarised parton distributions show significant differences for strange quarks (cf. Fig. 5.5). The COMPASS multiplicities show large uncertainties in the same x range, as well as missing data points, especially for large z. Both these uncertainties are reproduced in the extracted fragmentation functions. For small x all extractions of D_{str} have large errors, and show also large differences for the two used parton distributions.

For $x > 0.06$ the available unpolarised strange quark PDFs agree with each other quite well. However, the multiplicities show for $x > 0.2$ again large uncertainties and missing

data. Especially for small z they disagree with the LO theoretical calculations. The extracted fragmentation functions reflect these problems as well. The largest uncertainties appear for large x and small z.

Apart from the difference between the unpolarised strange quark parton distributions at small x, these issues apply to all the extractions. And yet the results for the non-strange fragmentation functions are quite stable and appear to be physically reasonable.

This could indicate that the measured kaon asymmetries do not carry as much information about Δs as assumed [63]. Another possibility is that the Q^2 dependence of fragmentation functions may be more significant than expected (cf. Section 2.4.1), and neglecting it may not be an option, at least in the case of strange quarks.

6.3 Comparison with EMC Results

Both pion and non-strange kaon fragmentation functions have been extracted before by the EMC collaboration in 1989 [10]. EMC was a fixed target experiment which used a 280 GeV muon beam to scatter off proton and deuterium targets. It was designed to cover a large acceptance and was equipped with detectors allowing particle identification.

The data analysis covered the kinematic domain of $Q^2 > 4\,(\text{GeV/c})^2$, a W^2 interval of [16, 200] GeV^2, an energy transfer ν in the range [20, 260] GeV and $x > 0.12$. The final statistics for the deuterium target include approximately 8000 DIS events. The parton distribution functions were taken from a parametrisation.

While the favoured and unfavoured pion fragmentation functions were defined as they are in this analysis, for the kaon fragmentation functions the following ad-hoc assumption has been made:

$$\frac{1}{2}(D_s^{K^+} + D_{\bar{s}}^{K^+}) = D_u^{K^+} \tag{6.1}$$

This method allowed to extract the u and $\bar{u}$ quark fragmentation functions into charged pions, kaons and protons. These data are usually refered to as 'EMC parametrisation of fragmentation functions'. In this section the EMC results for $D_u^{K^+}$, $D_{\bar{u}}^{K^+}$, $D_u^{\pi^+}$ and $D_{\bar{u}}^{\pi^+}$ are compared with the values for D_{fav} and D_{unf} for kaons and pions extracted in this analysis.

6.3.1 Pion Fragmentation Functions

Figure 6.7 shows the extracted pion fragmentation functions D_{fav} and D_{unf} from Section 6.1.1 and the pion fragmentation functions published by the EMC collaboration.

It has to be noted that the errors shown on the EMC pion fragmentation functions are statistical errors only. Their experimental systematic error was estimated to be about 10%

due to uncertainties in particle identification and less than 2% due to the parametrisation of the quark distribution functions [10].

The fragmentation functions extracted with the COMPASS multiplicities are uniformly larger than the EMC ones. Restricting the x range of this analysis to the EMC one $(0.030 < x < 0.440)$ does not change the results.

Taking into account the above mentioned systematic errors, the EMC fragmentation functions agree with the ones extracted from COMPASS multiplicities in all but the lowest z interval. In this interval, the COMPASS values are larger than the EMC ones by approximately 8% and 9% for D_{fav} and D_{unf} respectively.
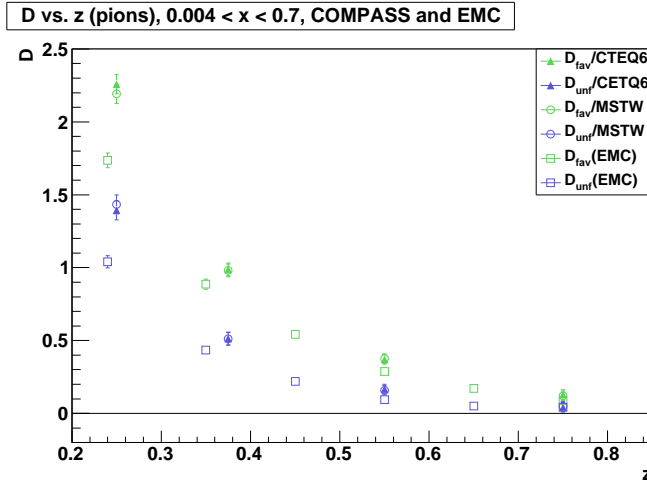
Figure 6.7: Pion fragmentation functions D_{fav} (green) and D_{unf} (blue). The full triangles mark the fragmentation functions extracted with CTEQ6 parton distribution functions, the open circles the ones extracted by using the MSTW parton distributions. The errors shown are statistical and systematical uncertainties combined. The open squares mark the fragmentation functions extracted by the EMC collaboration. The EMC errors shown are statistical errors only [10].

6.3.2   Kaon Fragmentation Functions

Figure 6.8 shows the extracted kaon fragmentation functions D_{fav} and D_{unf} from Section 6.2.1 and the kaon fragmentation functions published by the EMC collaboration.

As for the pion fragmentation functions, the errors shown for the EMC pion fragmentation functions are statistical errors only. Their systematic error was estimated to be approximately 15% due to uncertainties in the particle identification and less than 4% due to the parametrisation of the distribution functions [10].

Even without taking these systematic uncertainties into account the values for both the

D_{fav} and D_{unf} agree very well for the EMC fragmentation functions and the ones extracted in this analysis.
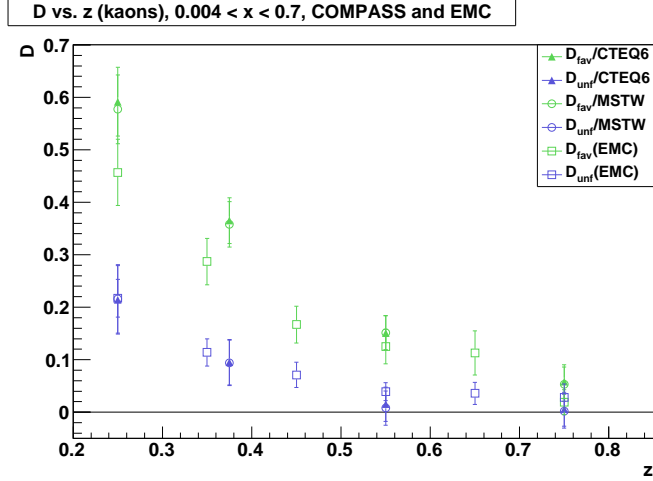
Figure 6.8: Kaon fragmentation functions D_{fav} (green)and D_{unf} (blue). The full triangles mark the fragmentation functions extracted with CTEQ6 parton distribution functions, the open circles the ones extracted by using the MSTW parton distributions. The errors shown are statistical and systematical uncertainties combined. The open squares mark the fragmentation functions extracted by the EMC collaboration. The EMC errors shown are statistical errors only [10].

6.3.3   Conclusions

The pion fragmentation functions extracted with the COMPASS multiplicities are larger than the EMC ones in all z bins, but agree with them within their systematic and statistical errors in all but the lowest z interval. The COMPASS kaon fragmentation functions D_{fav} and D_{unf} agree with the ones published by EMC very well.

6.4   Fragmentation Functions from Generated Multiplicities

The last few sections presented and discussed the results for fragmentation functions extracted from COMPASS multiplicities. While the values for the favoured and unfavoured fragmentation functions agree within the margin of error with the theoretical expectations, this is not the case for the kaon strange quark fragmentation functions. Possible reasons for these puzzling results might be found in the differences of the two sets of unpolarised PDFs used as input for the analysis, an underestimation of the importance of the Q^2 dependence of the fragmentation functions, or problems with the factorisation assumption

itself. Another reason for the unphysical results might lie in the multiplicities used in the analysis. This last option can be investigated by using another set of multiplicities.

Since no second set of experimental multiplicities was available, the PYTHIA simulation programme was used to create artificial multiplicities, which then were used as input for the system of equations to extract charged pion and kaon fragmentation functions. As in the analysis presented in the sections above, the unpolarised PDFs were again taken from the MSTW and the CTEQ6 parametrisations. Since all fragmentation functions extracted with the generated multiplicities showed the same dependency on the different sets of unpolarised PDFs as the ones for the measured multiplicities, only the results extracted with CTEQ PDFs are discussed in the following sections.

6.4.1   Generated Multiplicities

The particle physics event generator programme PYTHIA [53] uses a combination of various QCD-based models and parametrisations of experimental results to simulate physical processes (in this case deep-inelastic scattering) in an analytical way.

For this analysis ten million lepton-nucleon DIS events have been generated in the kinematic domain of the 2004 COMPASS muon set-up. The fragmentation of quarks into hadrons was simulated according to the LUND fragmentation model (cf. Section 2.2.2.1), and parametrisations of experimentally measured branching ratios were used to simulate the subsequent decay of unstable particles into stable ones.

In the following sections the generated charged pion and kaon multiplicities are shown and compared to the ones measured at COMPASS (cf. Section 5.4).

6.4.1.1   Generated Charged Pion Multiplicities

Figure 6.9 shows the generated multiplicities for charged pions, together with the experimentally extracted COMPASS pion multiplicities used in the analysis in the sections above. Both sets of multiplicities are plotted together, for two charges, in ten bins of x and four z intervals.

The generated multiplicities show considerable differences to the ones extracted from COMPASS data. The PYTHIA generated π^+ values disagree with the experimental ones in almost all intervals of z. At low z ($0.2 < z < 0.3$) they are smaller by 20 to 30% in all but the highest two bins of x. In the interval $0.3 < z < 0.45$ the generated multiplicities agree with the extracted ones within their margin of error. In the largest two intervals of z ($0.45 < z < 0.85$) the simulated values are larger than the experimental ones, and their difference increases with increasing x. Here the two multiplicities only agree at in the lowest bins of x.
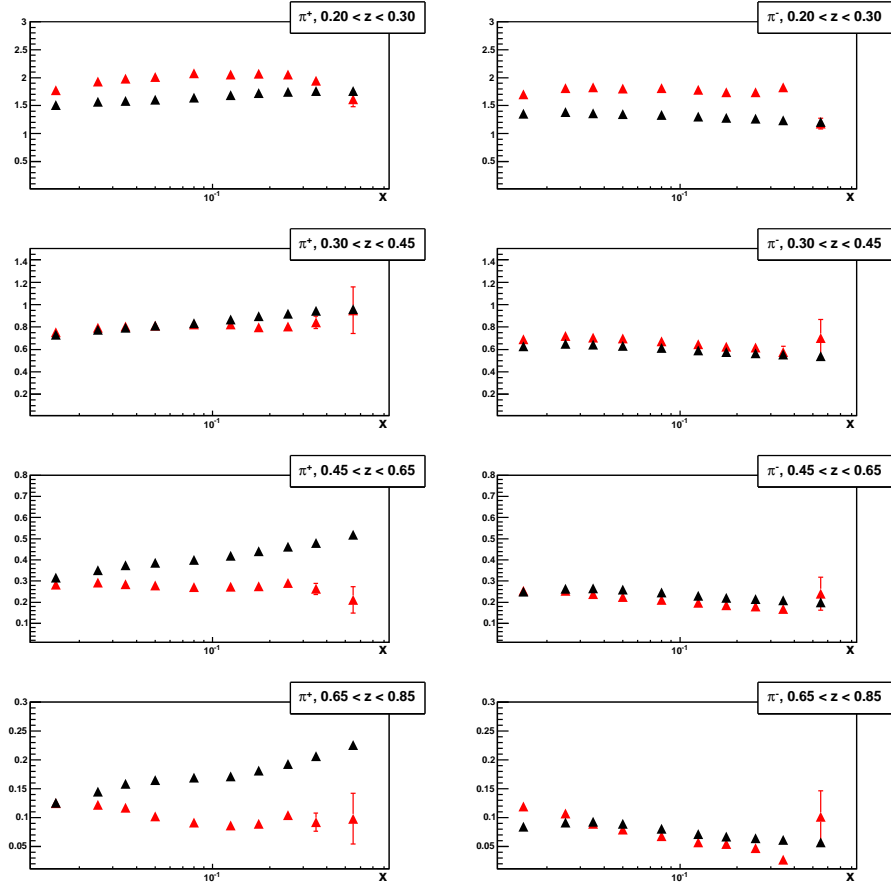
Figure 6.9: Generated and extracted multiplicities for charged pions (π^+ left and π^- right) in ten bins of x and four z intervals. The red triangles mark the values for the experimentally extracted COMPASS multiplicities, the black triangles the multiplicities simulated with PYTHIA.

The simulation of the π^- multiplicities is closer to the ones extracted from the experimental data. They agree within their margin of error in all but the lowest interval of z. For this interval the simulated values are again smaller than the experimental ones, by about 20 to 30% in all but the highest bin of x, much like the π^+ simulation for low z.

6.4.1.2 Generated Charged Kaon Multiplicities

Figure 6.10 shows the generated multiplicities for charged kaons, together with the experimentally extracted COMPASS kaon multiplicities. Both sets of multiplicities are plotted together, for two charges, in ten bins of x and four z intervals.

Like the generated pion multiplicities, the generated kaon multiplicities show significant differences to the experimental ones. For positvely charged kaons they are uniformly

smaller than the measured multiplicities for small z ($0.2 < z < 0.45$), with the largest x bin as the only exception. For large z ($0.65 < z < 0.85$) on the other hand the generated multiplicities exceed the experimentally measured values over the whole x range and also follow an opposite trend; the generated multiplicities increase with increasing x, while the measured ones decrease.

The generated K^- multiplicities show a better agreement with the experimental data; within the margin of error they agree with the measured multiplicities in three of the four intervals of z ($0.2 < z < 0.85$), in almost every bin of x. For small z they show the same trend as the generated K^+ multiplicities and fall below the measured values in all but the largest x bin, but the difference is much smaller.
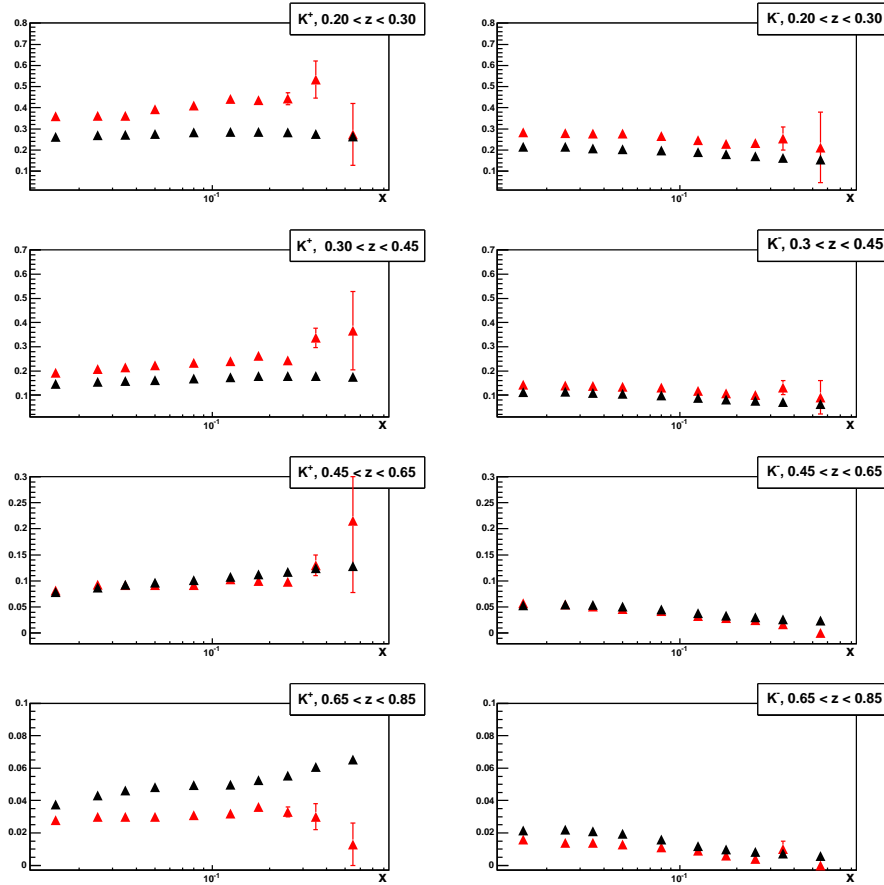
Figure 6.10: Generated and extracted multiplicities for charged kaons (K^+ left and K^- right) in ten bins of x and four z intervals. The red triangles mark the values for the experimentally extracted COMPASS multiplicities, the black triangles the multiplicities simulated with PYTHIA.

Generally the generated charged kaon multiplicities display the same behaviour as the

ones for charged pions; they are smaller then the measured ones for small z and larger for large z, and the best agreement is reached for negatively charged hadrons and $z > 0.2$.

6.4.2 Fragmentation Functions from PYTHIA Generated Multiplicities

In the following sections the pion and kaon fragmentation functions extracted with both sets of multiplicities (generated and measured) are presented together with simulated values for charged pion and kaon fragmentation functions (cf. Fig. 5.3 in Section 5.3 and 5.2 in Section 5.2) and their differences are discussed.

6.4.2.1 D_{fav} and D_{unf} for Charged Pions

The favoured and unfavoured pion fragmentation functions D_{fav} and D_{unf} extracted with the generated multiplicities are plotted in Fig. 6.11. For comparison the FFs extracted with the measured COMPASS multiplicities are shown, as well as the PYTHIA simulations of the corresponding pion fragmentation functions. For the latter the mean values of the favoured ($D_u^{\pi^+}$, $D_{\bar{d}}^{\pi^-}$, $D_{\bar{u}}^{\pi^-}$, $D_d^{\pi^-}$) and unfavoured ($D_{\bar{u}}^{\pi^+}$, $D_d^{\pi^+}$, $D_s^{\pi^+}$, $D_{\bar{s}}^{\pi^+}$, $D_u^{\pi^-}$, $D_{\bar{d}}^{\pi^-}$, $D_s^{\pi^-}$, $D_{\bar{s}}^{\pi^-}$) pion FFs respectively were calculated for each charge in each bin of z.
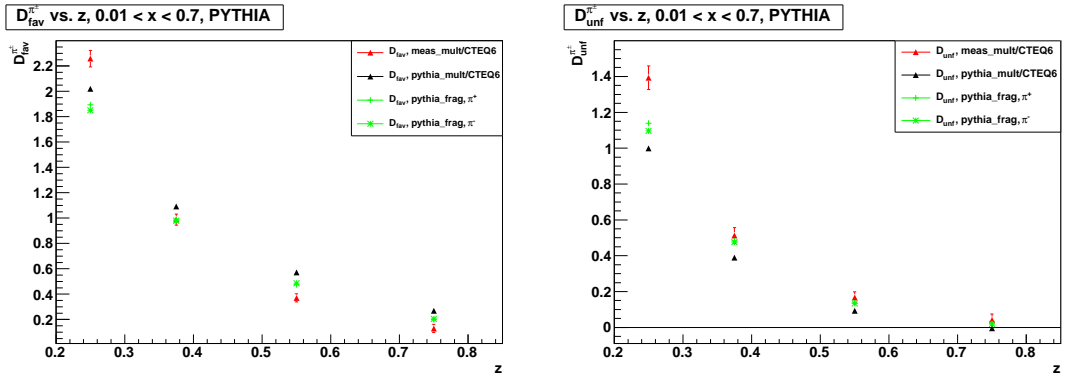
Figure 6.11: Favoured and unfavoured pion fragmentation functions D_{fav} (left) and D_{unf} (right) in four z bins. The black markers indicate the FFs extracted with generated multiplicities, the red markers the FFs extracted with experimental multiplicities. The green markers show the mean values for the corresponding simulated pion fragmentation functions ($D_u^{\pi^+}$ and $D_{\bar{d}}^{\pi^+}$ (+) and $D_{\bar{u}}^{\pi^-}$ and $D_d^{\pi^-}$ (∗) for D_{fav} and $D_{\bar{u}}^{\pi^+}$, $D_d^{\pi^+}$, $D_s^{\pi^+}$ and $D_{\bar{s}}^{\pi^+}$ (+) and $D_u^{\pi^-}$, $D_{\bar{d}}^{\pi^-}$, $D_s^{\pi^-}$ and $D_{\bar{s}}^{\pi^-}$ (∗) for D_{unf}) for comparison.

The D_{fav} values extracted with generated multiplicities are slightly smaller than the ones from the measured multiplicities for the first z bin ($0.2 < z < 0.3$), and larger for the last three ($0.3 < z < 0.85$). The same applies for the mean of the simulated fragmentation functions $D_u^{\pi^+}$ and $D_{\bar{d}}^{\pi^+}$ ($D_{\bar{u}}^{\pi^-}$ and $D_d^{\pi^-}$), but their values are uniformly smaller than the FFs from the simulated multiplicities.

For D_{unf} both the simulated fragmentation functions and the ones extracted with simulated multiplicities are smaller than the FFs extracted with measured COMPASS multiplicities in all bins of z. Unlike for D_{fav} the simulated multiplicities result in lower values than the simulation of the fragmentation functions themselves. While the latter agree within their margin of error with the values from the measured multiplicities in all but the lowest z interval, the FFs extracted using the simulated multiplicities differ by up to 35% from the ones for the experimental multiplicities. The differences are especially large for low z.

Generally, the values for both D_{fav} and D_{unf} from the PYTHIA simulated pion multiplicities and fragmentation functions display a more flat distribution as a function of z than the ones extracted from the measured multiplicities. It is also worth noting that the simulated fragmentation functions show significant differences to the FFs extracted with simulated multiplicities, despite the fact that the same fragmentation model (cf. Section 2.2.2.1) was used for both simulations.

6.4.2.2 D_{fav}, D_{unf} and D_{str} for Charged Kaons

The favoured and unfavoured kaon fragmentation functions D_{fav} and D_{unf} extracted with the simulated multiplicities are plotted in Fig. 6.12. For comparison the FFs extracted with the measured COMPASS multiplicities are shown, as well as the PYTHIA simulations of the corresponding quark fragmentation functions into kaons. These are $D_u^{K^+}$ and $D_{\bar{u}}^{K^-}$ for D_{fav}; for D_{unf} the mean values of all unfavoured FFs ($D_{\bar{u}}^{K^+}$, $D_d^{K^+}$, $D_{\bar{d}}^{K^+}$, $D_s^{K^+}$, $D_u^{K^-}$, $D_d^{K^-}$, $D_{\bar{d}}^{K^-}$ and $D_s^{K^-}$) were calculated in each interval of z for K^+ and K^- respectively.
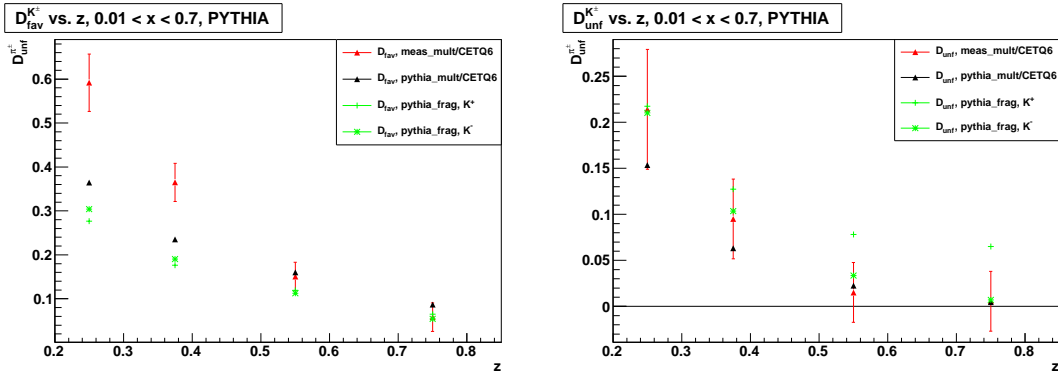
Figure 6.12: The favoured and unfavoured kaon fragmentation functions D_{fav} (left) and D_{unf} (right) in four bins of z. The black markers indicate the FFs extracted with simulated multiplicities, the red markers the FFs extracted with experimental multiplicities. The green markers show the corresponding simulated kaon fragmentation functions: $D_u^{K^+}$ (+) and $D_{\bar{u}}^{K^-}$ (*) for D_{fav} and the mean values of $D_{\bar{u}}^{K^+}$, $D_d^{K^+}$, $D_{\bar{d}}^{K^+}$, $D_s^{K^+}$ (+) and $D_u^{K^-}$, $D_d^{K^-}$, $D_{\bar{d}}^{K^-}$, $D_s^{K^-}$ (*) for D_{unf}.

Like the pion D_{fav}, the favoured kaon fragmentation function extracted from simulated multiplicities shows a more flat distribution as a function of z than the one for the measured

multiplicities; with lower values for small z and higher values for large z. The simulated fragmentation functions show the same behaviour, but have uniformly smaller values over the whole range of z.

D_{unf} from simulated multiplicities agrees within the (quite large) margin of error with the one from the measured COMPASS multiplicities in all bins of z, as well as with the simulated fragmentation functions for K^-. The latter though show quite significant differences to the simulated FFs for K^+, especially for the higher z intervals, casting doubt on the validity of the assumption that D_{unf} is equal for positively and negatively charged kaons (see also Section 5.2.1). Also, unlike the favoured kaon fragmentation functions, both are larger than the D_{unf} extracted with the simulated multiplicities.

Like the pion fragmentation functions, the simulated kaon FFs do not agree with the ones extracted from the simulated multiplicities; they are smaller for D_{fav} and larger for D_{unf}, even though both are based on PYTHIA simulations and the same model of fragmentation.

Figure 6.13 shows the strange quark fragmentation function D_{str} extracted with the PYTHIA generated multiplicities, together with the ones from the measured multiplicities and the simulated FFs $D_{\bar{s}}^{K^+}$ and $D_s^{K^-}$ for comparison.
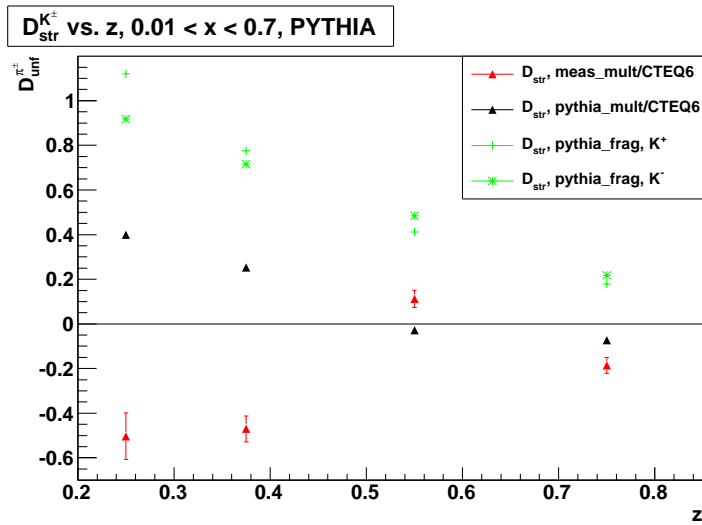
Figure 6.13: The kaon fragmentation function D_{str} in four bins of z. The black markers indicate the D_{str} values extracted with simulated multiplicities, the red markers the ones extracted with experimental multiplicities. The green markers show the corresponding simulated kaon fragmentation functions: $D_{\bar{s}}^{K^+}$ (+) and $D_s^{K^-}$ (∗)

The D_{str} extracted using the simulated multiplicities shows the same trend as a function of z as the simulated one, but is smaller by more than 50% over the whole range, and even negative for the lowest two z bins, although just slightly. None of the PYTHIA based strange quark fragmentation functions agree with the ones from the measured multiplicities. Again significant differences show between the simulated FFs for K^+ and K^-, in

this case especially for low z, casting doubt on the validity of grouping $D_{\bar{s}}^{K^+}$ and $D_s^{K^-}$ together into D_{str}.

While the results extracted with the PYTHIA generated multiplicities do not agree with the expectations from the simulation and even show negative and therefore unphysical values for large z, the overall distribution of D_{str} as a function of z does look much more reasonable than the one for the strange quark fragmentation function extracted with the measured multiplicities. To examine these results further, the influence of the x dependence of the simulated multiplicities on the extracted fragmentation functions will be tested here as well.

6.4.2.3 D_{str} for Charged Kaons for Split x Range

As already discussed in Sections 6.1.3 and 6.2.3 the x dependence of hadron multiplicities can be used to test the assumption that the fragmentation of a quark is independent of the initial scattering event from which it originates. If this factorisation holds, the fragmentation functions must be independent of x. To verify this assumption the x range for the multiplicities is divided into two parts, covering the intervals $[0.01 < x < 0.1]$ and $[0.1 < x < 0.7]$, respectively. The fragmentation functions are extracted again, using ten values of the simulated multiplicities (for five x bins and two charges) as input twice, once for the lower and once for the higher range of x. The results are plotted in Fig. 6.14. Like in the plots in the sections above, the FFs from the measured COMPASS multiplicities are shown for comparison, as well as the PYTHIA simulated strange quark fragmentation functions into kaons.
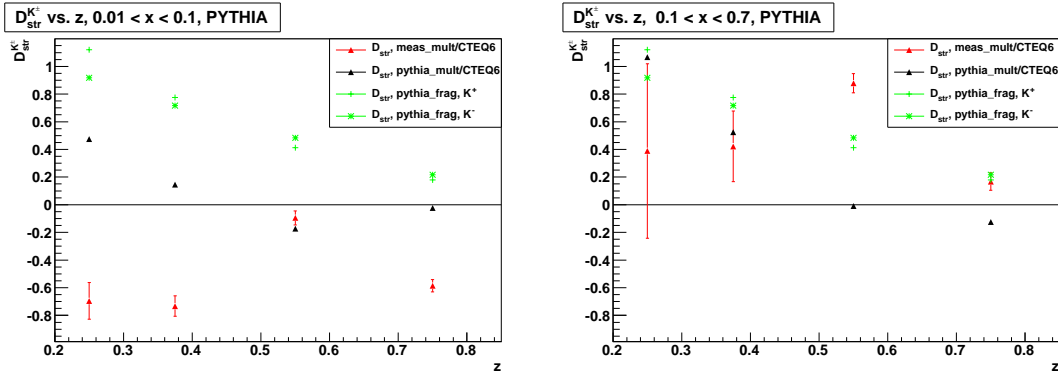
Figure 6.14: The kaon fragmentation function D_{str} in four bins of z for $0.01 < x < 0.1$ (left) and $0.1 < x < 0.7$ (right). The black markers indicate the D_{str} values extracted with simulated multiplicities, the red markers the ones extracted with experimental multiplicities. The green markers show the corresponding simulated kaon fragmentation functions $D_{\bar{s}}^{K^+}$ (+) and $D_s^{K^-}$ (∗).

Like the results for the full x range, the values for D_{str} extracted from simulated multiplicities are significantly smaller than the ones for the simulated fragmention functions $D_{\bar{s}}^{K^+}$

and $D_s^{K^-}$ in almost all bins of z for both the lower and the higher x range, and become compatible with zero or even slightly negative for $z > 0.45$. The values for the lower x interval are more than 50% lower for $0.01 < x < 0.1$ than they are for $0.1 < x < 0.7$.

It is worth noting though, that the distribution of the FFs as a function of z is quite similar for the two ranges of x. In both intervals D_{str} follows the same trend as the PYTHIA simulated $D_{\bar{s}}^{K^+}$ and $D_s^{K^-}$, something that is not the case for the strange fragmentation function extracted with the experimental multiplicities. While the results based on the simulation are far from the expected values, they do reproduce the shape of their distribution quite well, and also appear to be more stable in regard to the chosen range of x.

6.4.3   Conclusions

Pion and kaon multiplicities in ten x bins and four intervals of z have been simulated using the particle physics event generator PYTHIA. A comparison of the generated multiplicities with the experimental ones measured at COMPASS revealed significant differences, notably for positively charged hadrons, with the largest discrepancies found for $z > 0.65$; while the experimental multiplicities tend to decrease with increasing values of x, the simulated ones increase. To evaluate these results it is important to note that the PYTHIA generated multiplicities do not include a simulation of detector responses or accceptances, or an experimental set-up of any kind. The simulation is based on theoretical models and parametrisations of experimental results only.

These generated multiplicities were then used as input for the system of equations to extract charged pion and kaon fragmentation functions. The unpolarised PDFs were again taken from the MSTW and the CTEQ6 parametrisations. The two sets of fragmentation functions (extracted with simulated and measured multiplicities respectively) were then compared with each other as well as with PYTHIA simulations of quark fragmentation functions into charged pions and kaons.

The three sets of favoured and unfavoured pion fragmentation functions do not agree within their margin of error, but they only show larger deviations (up to 35%) for the smallest bin of z. The PYTHIA fragmentation functions and the FFs from the simulated multiplicities show the same distribution in z as the ones from the experimental multiplicities, although both decrease more slowly with increasing z. The same deviations can be observed for the favoured and unfavoured kaon fragmentation functions; the three sets of FFs agree with each other only for large z (D_{fav}) or small z (D_{unf}). Like for charged pions, the distribution of the FFs based on simulations appears to be more flat than the ones extracted with the measured multiplicities.

The strange quark fragmentation functions extracted with the PYTHIA generated multiplicities are up to 50% smaller than the simulated FFs $D_{\bar{s}}^{K^+}$ and $D_s^{K^-}$, but do reproduce the shape of their distribution quite well. Both decrease with increasing z. They do not agree with the FFs from the experimental multiplicities. The extracted D_{str} for two different intervals of x do not agree with either the corresponding simulated FFs, or each other.

However, they do display the same trend as a function of z (decreasing with increasing z), and as such appear to be more reasonable physically. Compared to strange quark FF extracted from measured multiplicities they also prove much more stable in regard to the chosen interval of x. It is also worth noting that the values for D_{str} are much larger for larger x, regardless of the multiplicities (experimental or simulated) used in the analysis, casting doubt on the validity of the factorisation assumption.

While these results suggest the possibility that the sets of kaon multiplicities measured at COMPASS are at least partly responsible for unphysical results for strange quark fragmentation function extracted with them, the evidence is not very convincing. The simulated multiplicities do not lead to results that agree with the simulated FFs or the various parametrisations for strange quark fragmentation. Another set of experimentally measured multiplicities would be necessary to clarify this issue.

Chapter 7

Summary and Outlook

Quark helicity distributions can be accessed by measuring spin asymmetries in polarised deep-inelastic scattering, but for a full flavour separation the precise knowledge of quark fragmentation functions is essential. Those can only be inferred from experimental data, and are still poorly determined today. The few existing parametrisations of fragmentation functions are derived from world data (mainly on electron-positron annihilation), and often differ considerably, most notably for strange quarks.

This thesis presents an independent evaluation of fragmentation functions from charged pion and kaon multiplicities extracted from data recorded at the COMPASS experiment. A method of extraction was developed, based on the relation between hadron multiplicities, $r^h(x, z)$, unpolarised parton distribution functions, $q(x)$, and quark fragmentation functions into hadrons, $D_q^h(z)$. An additional Q^2 dependence to all the factors was expected to be insignificant, and was neglected in this analysis.

The number of fragmentation functions in the equation can be reduced to six by specifying the hadron type and assuming charge conjugation symmetry. By grouping the remaining FFs according to magnitude and making use of the assumption that they depend only on the scaling variable z - while the unpolarisd PDFs only depend on the scaling variable x - a system of equations can be constructed that allows to extract fragmentation functions. Using experimental multiplicities and unpolarised PDFs from global parametrisations, three different FFs can be extracted for charged kaons (D_{str}, D_{fav}, D_{unf}), and two different ones (D_{fav}, D_{unf}) for pions.

Multiplicities for charged kaons and pions from 2004 semi-inclusive deep-inelastic scattering data have been extracted by the COMPASS collaboration last year. Together with two sets of unpolarised parton distribution functions from global parametrisations (CTEQ6 and MSTW) they were used as input for the system of equations outlined above, and charged pion and kaon fragmentation functions were extracted in four z bins. To evaluate the stability of the results a number of tests was performed. The x range of the multiplicities and unpolarised PDFs was limited to study the influence of larger uncertainties and missing data points of the experimental multiplicities on the resulting fragmentation

functions. The factorisation assumption - stating that the fragmentation of a quark is independent of the initial scattering event from which it originates - was put to the test by splitting the multiplicities and unpolarised PDFs into two subsets, one for the lower and one for the higher intervals of x. The extracted fragmentation functions were compared to the ones published by EMC, as well as to results derived with a set of artificial multiplicities generated with the particle physics event generator PYTHIA.

Four of the five extracted fragmentation functions - D_{fav} and D_{unf} for both pions and kaons - are quite stable with regard to the parton distribution used in the calculation as well as to the x range in which the analysis was performed, and agree with the ones published by EMC.

This is not the case for the fifth fragmentation function, D_{str} for charged kaons. The extracted strange quark fragmentation function is very unstable with regard to the x range of the multiplicities and PDFs used in the analysis, and also shows significant differences for the two different sets of unpolarised parton distribution functions. The extracted values for D_{str} are often negative - and therefore physically impossible. The test of the factorisation assumption leads to incompatible results for the two intervals of x. The two sets of D_{str} extracted using experimental and simulated multiplicities also do not agree. While the use of PYTHIA generated multiplicities leads to results that are more stable with regard to the interval of x used in the analysis, as well as physically possible, they are much smaller than expected. All sets of D_{str} extracted in this analysis, regardless of the interval of x, the version unpolarised PDFs or multiplicities used, disagree with PYTHIA simulations of strange quark fragmentation functions, as well as with predictions from parametrisations.

The study of fragmentation functions, in particular the strange quark fragmentation functions into kaons, is a subject of ongoing and future research for the COMPASS collaboration. Alternative methods of extraction of FFs are being explored, as are various approaches of integrating the Q^2 dependence of fragmentation functions into the analysis. The charged pion and kaon multiplicities used in this analysis represent only a first attempt of an extraction of hadron multiplicities from experimental data. This, too, continues to be an important field of research for COMPASS.

Appendix A

Calculation of the Fragmentation Functions

The matrices in Eq.s 5.9 and 5.23 (cf. Sections 5.2 and 5.3) represent a system of 24 linear equations (for twelve x bins and two charges each) which is used to calculate three (for kaons) or two (for pions) unknowns - the three and two unknown fragmentation functions for kaons and pions, respectively. The 24 equations constrain the system, it is overdetermined; therefore no exact solution exists. To find an approximate solution the method of least squares is used. For the system of equations

$$\vec{r} = B \times \vec{D},$$

χ^2 is given by

$$\chi^2 = (B\vec{D} - \vec{r})^T G (B\vec{D} - \vec{r}), \qquad (A.1)$$

where $\vec{D}$ is the vector containing the fragmentation functions, B the matrix containing the unpolarised PDFs, and $\vec{r}$ the vector containing the multiplicities.

The errors for the multiplicities are enclosed in the covariance matrix, cov. The inverted error matrix, cov^{-1}, is represented by G.

Minimising χ^2:

$$\frac{\delta}{\delta\vec{D}}\chi^2 = 0 \qquad (A.2)$$

yields the equation for the fragmentation functions:

$$\vec{D} = \left[(B^T G B)^{-1} \cdot B^T G\right]\vec{r}. \qquad (A.3)$$

The error matrices used in this analysis are explained in detail below.

A.1   Error Matrices

The extracted COMPASS multiplicities [39] are given with a statistical and a systematical error in each x and z bin (cf. Tables C.3, C.4, C.1, C.2).

The statistical uncertainties, $\sigma^{stat}_{K^\pm(x_i)}$, are uncorrelated; the respective error matrix is therefore diagonal:

$$cov^{stat} = \begin{pmatrix} \left(\sigma^{stat}_{K^+(x_1)}\right)^2 & 0 & \cdots & 0 & 0 \\ 0 & \left(\sigma^{stat}_{K^-(x_1)}\right)^2 & \cdots & 0 & 0 \\ \vdots & \vdots & \ddots & \vdots & \vdots \\ 0 & 0 & \cdots & \left(\sigma^{stat}_{K^+(x_{12})}\right)^2 & 0 \\ 0 & 0 & \cdots & 0 & \left(\sigma^{stat}_{K^-(x_{12})}\right)^2 \end{pmatrix} \tag{A.4}$$

The systematical error for the multiplicities, σ_{sys}, also given for each x and z bin, breaks down into three parts (cf. Appendix C):

- Stability of hadron multiplicities versus time (σ^{COMP}_{sys})

- Acceptance calculation (σ^{MC}_{sys})

- Sensitivity to the parameters used for identification in the RICH detector (σ^{RICH}_{sys})

Unlike the statistical uncertainties, these systematical errors are not uncorrelated. To be able to include these errors into the calculation while keeping the covariance matrix invertible, the total systematical error has been averaged over the twelve x bins in each bin of z. The average systematic error σ and the statistical errors $\sigma^{stat}_{K^\pm(x_i)}$ have been combined quadratically for each of the calculations. Assuming 100% correlation, the covariance matrix for the full error cov^{full} is therefore given by:

$$\begin{pmatrix} \left(\sigma^{stat}_{K^+(x_1)}\right)^2 + \sigma^2_{sys} & \sigma^2_{sys} & \cdots & \sigma^2_{sys} & \sigma^2_{sys} \\ \sigma^2_{sys} & \left(\sigma^{stat}_{K^-(x_1)}\right)^2 + \sigma^2_{sys} & \cdots & \sigma^2_{sys} & \sigma^2_{sys} \\ \vdots & \vdots & \ddots & \vdots & \vdots \\ \sigma^2_{sys} & \sigma^2_{sys} & \cdots & \left(\sigma^{stat}_{K^+(x_{12})}\right)^2 + \sigma^2_{sys} & \sigma^2_{sys} \\ \sigma^2_{sys} & \sigma^2_{sys} & \cdots & \sigma^2_{sys} & \left(\sigma^{stat}_{K^-(x_{12})}\right)^2 + \sigma^2_{sys} \end{pmatrix} \tag{A.5}$$

The actual level of correllation is very difficult to evaluate with the available data. To ensure that the uncertainties were not underestimated the error matrix in Eq. A.5 was used for all calculations in this analysis. The quadratical combination of the systematic and statistical errors may lead to a slight overestimation of errors as well, since uncertainties that are common to positively and negatively charged hadron are counted twice.

Appendix B

Pion and Kaon Fragmentation Functions vs. z

This section lists the extracted fragmentation functions for charged pions and kaons from COMPASS multiplicities:

- Pion fragmentation functions

  - Pion fragmentation functions D_{fav}, D_{unf} for $0.004 < x < 0.7$: Table B.1
  - Pion fragmentation functions D_{fav}, D_{unf} for $0.006 < x < 0.4$: Table B.2
  - Pion fragmentation functions D_{fav}, D_{unf} for $0.004 < x < 0.06$: Table B.3
  - Pion fragmentation functions D_{fav}, D_{unf} for $0.06 < x < 0.7$: Table B.4

- Kaon fragmentation functions

  - Kaon fragmentation functions D_{str}, D_{fav}, D_{unf} for $0.004 < x < 0.7$: Table B.5
  - Kaon fragmentation functions D_{str}, D_{fav}, D_{unf} for $0.01 < x < 0.3$: Table B.6
  - Kaon fragmentation functions D_{str}, D_{fav}, D_{unf} for $0.004 < x < 0.06$: Table B.7
  - Kaon fragmentation functions D_{str}, D_{fav}, D_{unf} for $0.06 < x < 0.7$: Table B.8

Details:

- all fragmentation functions extracted with the COMPASS multiplicities listed in Section C

- all fragmentation functions extracted with CTEQ6-LO and MSTW2008-LO parton distributions

z	D_{fav}^{CTEQ}	ΔD_{fav}^{CTEQ}	D_{unf}^{CTEQ}	ΔD_{unf}^{CTEQ}
0.20 - 0.30	0.226	± 0.007	0.140	± 0.007
0.30 - 0.45	0.148	± 0.007	0.077	± 0.007
0.45 - 0.65	0.074	± 0.007	0.033	± 0.007
0.65 - 0.85	0.026	± 0.007	0.009	± 0.007
0.20 - 0.80	0.474	± 0.013	0.258	± 0.013

z	D_{fav}^{MSTW}	ΔD_{fav}^{MSTW}	D_{unf}^{MSTW}	ΔD_{unf}^{MSTW}
0.30 - 0.45	0.219	± 0.007	0.143	± 0.007
0.45 - 0.65	0.147	± 0.007	0.077	± 0.007
0.65 - 0.85	0.075	± 0.007	0.032	± 0.007
0.65 - 0.85	0.024	± 0.007	0.010	± 0.007
0.20 - 0.80	0.466	± 0.013	0.262	± 0.013

Table B.1: The extracted pion fragmentation functions D_{fav} and D_{unf} for $0.004 < x < 0.7$ in four z bins, and integrated over the whole z range, including their combined statistical and systematical errors (cf. Fig. 6.1).

z	D_{fav}^{CTEQ}	ΔD_{fav}^{CTEQ}	D_{unf}^{CTEQ}	ΔD_{unf}^{CTEQ}
0.20 - 0.30	0.226	± 0.007	0.142	± 0.007
0.30 - 0.45	0.148	± 0.007	0.078	± 0.007
0.45 - 0.65	0.074	± 0.007	0.033	± 0.007
0.65 - 0.85	0.028	± 0.007	0.013	± 0.007
0.20 - 0.85	0.476	± 0.013	0.266	± 0.013

z	D_{fav}^{MSTW}	ΔD_{fav}^{MSTW}	D_{unf}^{MSTW}	ΔD_{unf}^{MSTW}
0.20 - 0.30	0.221	± 0.007	0.145	± 0.007
0.30 - 0.45	0.148	± 0.007	0.077	± 0.007
0.45 - 0.65	0.075	± 0.007	0.032	± 0.007
0.65 - 0.85	0.028	± 0.007	0.012	± 0.007
0.20 - 0.85	0.472	± 0.013	0.266	± 0.013

Table B.2: The extracted pion fragmentation functions D_{fav} and D_{unf} for $0.006 < x < 0.4$ in four z bins, and integrated over the whole z range, including their combined statistical and systematical errors (cf. Fig. 6.2).

z	D_{fav}^{CTEQ}	ΔD_{fav}^{CTEQ}	D_{unf}^{CTEQ}	ΔD_{unf}^{CTEQ}
0.20 - 0.30	0.225	$\pm$ 0.007	0.137	$\pm$ 0.007
0.30 - 0.45	0.150	$\pm$ 0.007	0.076	$\pm$ 0.007
0.45 - 0.65	0.078	$\pm$ 0.007	0.032	$\pm$ 0.007
0.65 - 0.85	0.029	$\pm$ 0.007	0.007	$\pm$ 0.007
0.20 - 0.85	0.481	$\pm$ 0.013	0.252	$\pm$ 0.013

z	D_{fav}^{MSTW}	ΔD_{fav}^{MSTW}	D_{unf}^{MSTW}	ΔD_{unf}^{MSTW}
0.20 - 0.30	0.214	$\pm$ 0.007	0.145	$\pm$ 0.007
0.30 - 0.45	0.146	$\pm$ 0.007	0.078	$\pm$ 0.007
0.45 - 0.65	0.077	$\pm$ 0.007	0.032	$\pm$ 0.007
0.65 - 0.85	0.024	$\pm$ 0.007	0.011	$\pm$ 0.007
0.20 - 0.85	0.461	$\pm$ 0.013	0.265	$\pm$ 0.013

Table B.3: The extracted pion fragmentation functions D_{fav} and D_{unf} for $0.004 < x < 0.06$ in four z bins, and integrated over the whole z range, including their combined statistical and systematical errors (cf. Fig. 6.3).

z	D_{fav}^{CTEQ}	ΔD_{fav}^{CTEQ}	D_{unf}^{CTEQ}	ΔD_{unf}^{CTEQ}
0.20 - 0.30	0.234	$\pm$ 0.007	0.157	$\pm$ 0.007
0.30 - 0.45	0.147	$\pm$ 0.007	0.078	$\pm$ 0.007
0.45 - 0.65	0.065	$\pm$ 0.007	0.030	$\pm$ 0.007
0.65 - 0.85	0.023	$\pm$ 0.007	0.008	$\pm$ 0.007
0.20 - 0.85	0.468	$\pm$ 0.013	0.273	$\pm$ 0.013

z	D_{fav}^{MSTW}	ΔD_{fav}^{MSTW}	D_{unf}^{MSTW}	ΔD_{unf}^{MSTW}
0.20 - 0.30	0.237	$\pm$ 0.007	0.153	$\pm$ 0.007
0.30 - 0.45	0.149	$\pm$ 0.007	0.076	$\pm$ 0.007
0.45 - 0.65	0.066	$\pm$ 0.007	0.029	$\pm$ 0.007
0.65 - 0.85	0.024	$\pm$ 0.007	0.007	$\pm$ 0.007
0.20 - 0.85	0.477	$\pm$ 0.013	0.265	$\pm$ 0.013

Table B.4: The extracted pion fragmentation functions D_{fav} and D_{unf} for $0.06 < x < 0.7$ in four z bins, and integrated over the whole z range, including their combined statistical and systematical errors (cf. Fig. 6.3).

z	D_{str}^{CTEQ}	ΔD_{str}^{CTEQ}	D_{fav}^{CTEQ}	ΔD_{fav}^{CTEQ}	D_{unf}^{CTEQ}	ΔD_{unf}^{CTEQ}
0.20 - 0.30	- 0.050	$\pm$ 0.010	+ 0.059	$\pm$ 0.007	+ 0.021	$\pm$ 0.007
0.30 - 0.45	- 0.070	$\pm$ 0.009	+ 0.055	$\pm$ 0.007	+ 0.014	$\pm$ 0.007
0.45 - 0.65	+ 0.022	$\pm$ 0.008	+ 0.030	$\pm$ 0.007	+ 0.003	$\pm$ 0.007
0.65 - 0.85	- 0.037	$\pm$ 0.007	+ 0.012	$\pm$ 0.007	+ 0.001	$\pm$ 0.007
0.20 - 0.80	- 0.135	$\pm$ 0.017	+ 0.156	$\pm$ 0.013	+ 0.040	$\pm$ 0.013

z	D_{str}^{MSTW}	ΔD_{str}^{MSTW}	D_{fav}^{MSTW}	ΔD_{fav}^{MSTW}	D_{unf}^{MSTW}	ΔD_{unf}^{MSTW}
0.20 - 0.30	-0.073	$\pm$ 0.020	0.058	$\pm$ 0.007	0.022	$\pm$ 0.007
0.30 - 0.45	-0.088	$\pm$ 0.013	0.054	$\pm$ 0.007	0.014	$\pm$ 0.007
0.45 - 0.65	0.051	$\pm$ 0.010	0.030	$\pm$ 0.007	0.002	$\pm$ 0.007
0.65 - 0.85	-0.020	$\pm$ 0.008	0.011	$\pm$ 0.007	0.000	$\pm$ 0.007
0.20 - 0.80	-0.130	$\pm$ 0.027	+0.152	$\pm$ 0.013	+0.038	$\pm$ 0.013

Table B.5: The extracted kaon fragmentation functions D_{str}, D_{fav} and D_{unf} for $0.004 < x < 0.7$ in four z bins, and integrated over the whole z range, including their combined statistical and systematical errors (cf. Fig. 6.4).

z	D_{str}^{CTEQ}	ΔD_{str}^{CTEQ}	D_{fav}^{CTEQ}	ΔD_{fav}^{CTEQ}	D_{unf}^{CTEQ}	ΔD_{unf}^{CTEQ}
0.20 - 0.30	-0.019	$\pm$ 0.016	0.057	$\pm$ 0.007	0.021	$\pm$ 0.007
0.30 - 0.45	-0.033	$\pm$ 0.016	0.053	$\pm$ 0.007	0.013	$\pm$ 0.007
0.45 - 0.65	0.039	$\pm$ 0.016	0.030	$\pm$ 0.007	0.002	$\pm$ 0.007
0.65 - 0.85	0.013	$\pm$ 0.016	0.011	$\pm$ 0.007	0.000	$\pm$ 0.007
0.20 - 0.80	-0.000	$\pm$ 0.033	0.151	$\pm$ 0.013	0.036	$\pm$ 0.013

z	D_{str}^{MSTW}	ΔD_{str}^{MSTW}	D_{fav}^{MSTW}	ΔD_{fav}^{MSTW}	D_{unf}^{MSTW}	ΔD_{unf}^{MSTW}
0.20 - 0.30	-0.055	$\pm$ 0.027	0.058	$\pm$ 0.007	0.021	$\pm$ 0.007
0.30 - 0.45	-0.065	$\pm$ 0.027	0.054	$\pm$ 0.007	0.013	$\pm$ 0.007
0.45 - 0.65	0.061	$\pm$ 0.027	0.030	$\pm$ 0.007	0.001	$\pm$ 0.007
0.65 - 0.85	0.017	$\pm$ 0.027	0.011	$\pm$ 0.007	-0.001	$\pm$ 0.007
0.20 - 0.80	-0.042	$\pm$ 0.053	0.153	$\pm$ 0.013	0.035	$\pm$ 0.013

Table B.6: The extracted kaon fragmentation functions D_{str}, D_{fav} and D_{unf} for $0.01 < x < 0.3$ in four z bins, and integrated over the whole z range, including their combined statistical and systematical errors (cf. Fig. 6.5).

z	D_{str}^{CTEQ}	ΔD_{str}^{CTEQ}	D_{fav}^{CTEQ}	ΔD_{fav}^{CTEQ}	D_{unf}^{CTEQ}	ΔD_{unf}^{CTEQ}
0.20 - 0.30	-0.070	± 0.013	0.061	± 0.007	0.022	± 0.007
0.30 - 0.45	-0.110	± 0.011	0.058	± 0.007	0.015	± 0.007
0.45 - 0.65	-0.019	± 0.010	0.034	± 0.007	0.004	± 0.007
0.65 - 0.85	-0.117	± 0.009	0.016	± 0.007	0.005	± 0.007
0.20 - 0.80	-0.316	± 0.022	0.170	± 0.013	0.045	± 0.013

z	D_{str}^{MSTW}	ΔD_{str}^{MSTW}	D_{fav}^{MSTW}	ΔD_{fav}^{MSTW}	D_{unf}^{MSTW}	ΔD_{unf}^{MSTW}
0.20 - 0.30	-0.017	± 0.053	0.056	± 0.007	0.020	± 0.007
0.30 - 0.45	-0.228	± 0.037	0.059	± 0.007	0.019	± 0.007
0.45 - 0.65	0.028	± 0.032	0.033	± 0.007	0.001	± 0.007
0.65 - 0.85	0.015	± 0.032	0.010	± 0.007	-0.001	± 0.007
0.20 - 0.80	-0.202	± 0.079	0.157	± 0.013	0.039	± 0.013

Table B.7: The extracted kaon fragmentation functions D_{str}, D_{fav} and D_{unf} for $0.004 < x < 0.06$ in four z bins, and integrated over the whole z range, including their combined statistical and systematical errors (cf. Fig. 6.6).

z	D_{str}^{CTEQ}	ΔD_{str}^{CTEQ}	D_{fav}^{CTEQ}	ΔD_{fav}^{CTEQ}	D_{unf}^{CTEQ}	ΔD_{unf}^{CTEQ}
0.20 - 0.30	0.039	± 0.063	0.055	± 0.007	0.020	± 0.007
0.30 - 0.45	0.063	± 0.038	0.048	± 0.007	0.013	± 0.007
0.45 - 0.65	0.176	± 0.014	0.025	± 0.007	0.000	± 0.007
0.65 - 0.85	0.034	± 0.013	0.009	± 0.007	0.000	± 0.007
0.20 - 0.80	0.311	± 0.076	0.137	± 0.013	0.033	± 0.013

z	D_{str}^{MSTW}	ΔD_{str}^{MSTW}	D_{fav}^{MSTW}	ΔD_{fav}^{MSTW}	D_{unf}^{MSTW}	ΔD_{unf}^{MSTW}
0.20 - 0.30	0.019	± 0.061	0.057	± 0.007	0.020	± 0.007
0.30 - 0.45	0.043	± 0.037	0.050	± 0.007	0.012	± 0.007
0.45 - 0.65	0.141	± 0.014	0.028	± 0.007	0.000	± 0.007
0.65 - 0.85	0.024	± 0.013	0.010	± 0.007	0.000	± 0.007
0.20 - 0.80	0.226	± 0.074	0.145	± 0.013	0.031	± 0.013

Table B.8: The extracted kaon fragmentation functions D_{str}, D_{fav} and D_{unf} for $0.06 < x < 0.7$ in four z bins, and integrated over the whole z range, including their combined statistical and systematical errors (cf. Fig. 6.6).

Appendix C

Multiplicities vs. x and z

This section lists the COMPASS multiplicities (corrected for acceptance, smearing and radiative effects) used for the extraction of the fragmentation functions. They are given in twelve x bins and four intervals of z (taken from [39]):

- π^+ multiplicities: Table C.1

- π^- multiplicities: Table C.2

- K^+ multiplicities: Table C.3

- K^- multiplicities: Table C.4

Details:

- COMPASS data taken in 2004: muon beam on ^{6}LiD target

- $Q^2 > 1$ [GeV/c]^2

- $0.1 < y < 0.9$

- $0.004 < x < 0.7$

- $W > 7$ GeV

z bin	x bin	M^{π^+}	σ_{stat}	σ_{sys}^{COMP}	σ_{sys}^{MC}	σ_{sys}^{RICH}	σ_{sys}^{tot}
[0.20, 0.30]	[0.004, 0.006]	1.470	0.011	0.012	0.0202	0.0490	0.0543
[0.20, 0.30]	[0.006, 0.01]	1.605	0.006	0.006	0.0298	0.0642	0.0711
[0.20, 0.30]	[0.01, 0.02]	1.775	0.004	0.004	0.0003	0.0565	0.0567
[0.20, 0.30]	[0.02, 0.03]	1.934	0.005	0.006	0.0224	0.0488	0.0540
[0.20, 0.30]	[0.03, 0.04]	1.985	0.007	0.008	0.0349	0.0405	0.0541
[0.20, 0.30]	[0.04, 0.06]	2.011	0.007	0.008	0.0328	0.0372	0.0502
[0.20, 0.30]	[0.06, 0.10]	2.081	0.008	0.009	0.0332	0.0348	0.0490
[0.20, 0.30]	[0.10, 0.15]	2.058	0.014	0.015	0.0149	0.0387	0.0440
[0.20, 0.30]	[0.15, 0.20]	2.071	0.026	0.028	0.0183	0.0451	0.0562
[0.20, 0.30]	[0.20, 0.30]	2.055	0.039	0.043	0.0409	0.0377	0.0701
[0.20, 0.30]	[0.30, 0.40]	1.943	0.113	0.124	0.0005	0.0496	0.1337
[0.20, 0.30]	[0.40, 0.70]	1.611	0.363	0.400	0.0096	0.1401	0.4236
[0.30, 0.45]	[0.004, 0.006]	0.645	0.008	0.009	0.0458	0.0687	0.0831
[0.30, 0.45]	[0.006, 0.01]	0.700	0.004	0.004	0.0158	0.0392	0.0425
[0.30, 0.45]	[0.01, 0.02]	0.754	0.002	0.003	0.0065	0.0224	0.0234
[0.30, 0.45]	[0.02, 0.03]	0.795	0.003	0.003	0.0018	0.0157	0.0161
[0.30, 0.45]	[0.03, 0.04]	0.804	0.004	0.004	0.0094	0.0122	0.0160
[0.30, 0.45]	[0.04, 0.06]	0.814	0.004	0.004	0.0073	0.0124	0.0150
[0.30, 0.45]	[0.06, 0.10]	0.824	0.004	0.004	0.0104	0.0091	0.0146
[0.30, 0.45]	[0.10, 0.15]	0.824	0.007	0.007	0.0106	0.0041	0.0134
[0.30, 0.45]	[0.15, 0.20]	0.798	0.012	0.013	0.0109	0.0002	0.0170
[0.30, 0.45]	[0.20, 0.30]	0.804	0.018	0.020	0.0076	0.0072	0.0228
[0.30, 0.45]	[0.30, 0.40]	0.842	0.056	0.061	0.0296	0.0000	0.0680
[0.30, 0.45]	[0.40, 0.70]	0.950	0.209	0.230	0.3551	0.0432	0.4253
[0.45, 0.65]	[0.004, 0.006]	0.256	0.019	0.021	0.0144	0.0427	0.0496
[0.45, 0.65]	[0.006, 0.01]	0.270	0.003	0.004	0.0065	0.0239	0.0250
[0.45, 0.65]	[0.01, 0.02]	0.284	0.001	0.002	0.0032	0.0109	0.0115
[0.45, 0.65]	[0.02, 0.03]	0.293	0.002	0.002	0.0006	0.0079	0.0081
[0.45, 0.65]	[0.03, 0.04]	0.285	0.002	0.002	0.0015	0.0061	0.0067
[0.45, 0.65]	[0.04, 0.06]	0.279	0.002	0.002	0.0035	0.0052	0.0066
[0.45, 0.65]	[0.06, 0.10]	0.272	0.002	0.002	0.0005	0.0031	0.0039
[0.45, 0.65]	[0.10, 0.15]	0.274	0.003	0.004	0.0020	0.0009	0.0041
[0.45, 0.65]	[0.15, 0.20]	0.276	0.006	0.006	0.0054	0.0028	0.0089
[0.45, 0.65]	[0.20, 0.30]	0.290	0.010	0.010	0.0056	0.0073	0.0139
[0.45, 0.65]	[0.30, 0.40]	0.263	0.026	0.029	0.0045	0.0393	0.0490
[0.45, 0.65]	[0.40, 0.70]	0.211	0.063	0.069	0.0661	0.0000	0.0959
[0.65, 0.85]	[0.004, 0.006]	0.000	0.000	0.000	0.0000	0.0000	0.0000
[0.65, 0.85]	[0.006, 0.01]	0.120	0.005	0.006	0.0004	0.0138	0.0150
[0.65, 0.85]	[0.01, 0.02]	0.125	0.001	0.001	0.0008	0.0055	0.0058
[0.65, 0.85]	[0.02, 0.03]	0.122	0.001	0.001	0.0001	0.0040	0.0043
[0.65, 0.85]	[0.03, 0.04]	0.117	0.002	0.002	0.0006	0.0037	0.0041
[0.65, 0.85]	[0.04, 0.06]	0.102	0.001	0.001	0.0008	0.0034	0.0038
[0.65, 0.85]	[0.06, 0.10]	0.091	0.001	0.001	0.0001	0.0002	0.0014
[0.65, 0.85]	[0.10, 0.15]	0.086	0.002	0.002	0.0002	0.0022	0.0030
[0.65, 0.85]	[0.15, 0.20]	0.089	0.003	0.004	0.0015	0.0058	0.0071
[0.65, 0.85]	[0.20, 0.30]	0.104	0.006	0.007	0.0011	0.0137	0.0152
[0.65, 0.85]	[0.30, 0.40]	0.092	0.016	0.018	0.0022	0.0290	0.0339
[0.65, 0.85]	[0.40, 0.70]	0.098	0.044	0.048	0.0597	0.0983	0.1247

Table C.1: Positive pion multiplicities in bins of x and z [39]

z bin	x bin	M^{π^-}	σ_{stat}	σ_{sys}^{COMP}	σ_{sys}^{MC}	σ_{sys}^{RICH}	σ_{sys}^{tot}
[0.20, 0.30]	[0.004, 0.006]	1.423	0.011	0.007	0.0330	0.0345	0.0483
[0.20, 0.30]	[0.006, 0.01]	1.560	0.006	0.004	0.0161	0.0957	0.0972
[0.20, 0.30]	[0.01, 0.02]	1.701	0.004	0.003	0.0005	0.0622	0.0622
[0.20, 0.30]	[0.02, 0.03]	1.816	0.005	0.004	0.0226	0.0207	0.0309
[0.20, 0.30]	[0.03, 0.04]	1.829	0.007	0.005	0.0270	0.0172	0.0325
[0.20, 0.30]	[0.04, 0.06]	1.807	0.007	0.005	0.0255	0.0125	0.0288
[0.20, 0.30]	[0.06, 0.10]	1.812	0.008	0.006	0.0345	0.0025	0.0350
[0.20, 0.30]	[0.10, 0.15]	1.784	0.013	0.009	0.0379	0.0163	0.0422
[0.20, 0.30]	[0.15, 0.20]	1.736	0.024	0.017	0.0130	0.0187	0.0282
[0.20, 0.30]	[0.20, 0.30]	1.736	0.037	0.026	0.0112	0.0090	0.0294
[0.20, 0.30]	[0.30, 0.40]	1.828	0.108	0.076	0.0724	0.0155	0.1058
[0.20, 0.30]	[0.40, 0.70]	1.179	0.311	0.218	0.1755	0.0000	0.2799
[0.30, 0.45]	[0.004, 0.006]	0.610	0.008	0.005	0.0335	0.0309	0.0459
[0.30, 0.45]	[0.006, 0.01]	0.650	0.004	0.003	0.0155	0.0241	0.0288
[0.30, 0.45]	[0.01, 0.02]	0.691	0.002	0.002	0.0044	0.0246	0.0250
[0.30, 0.45]	[0.02, 0.03]	0.719	0.003	0.002	0.0082	0.0169	0.0189
[0.30, 0.45]	[0.03, 0.04]	0.704	0.004	0.003	0.0032	0.0155	0.0161
[0.30, 0.45]	[0.04, 0.06]	0.699	0.003	0.002	0.0089	0.0132	0.0162
[0.30, 0.45]	[0.06, 0.10]	0.671	0.004	0.003	0.0093	0.0120	0.0154
[0.30, 0.45]	[0.10, 0.15]	0.645	0.006	0.004	0.0120	0.0053	0.0137
[0.30, 0.45]	[0.15, 0.20]	0.626	0.011	0.008	0.0158	0.0086	0.0195
[0.30, 0.45]	[0.20, 0.30]	0.616	0.016	0.011	0.0182	0.0136	0.0254
[0.30, 0.45]	[0.30, 0.40]	0.578	0.049	0.034	0.0398	0.0168	0.0550
[0.30, 0.45]	[0.40, 0.70]	0.700	0.168	0.117	0.0057	0.0368	0.1232
[0.45, 0.65]	[0.004, 0.006]	0.222	0.017	0.012	0.0245	0.0319	0.0420
[0.45, 0.65]	[0.006, 0.01]	0.244	0.003	0.002	0.0050	0.0172	0.0180
[0.45, 0.65]	[0.01, 0.02]	0.253	0.001	0.001	0.0035	0.0077	0.0085
[0.45, 0.65]	[0.02, 0.03]	0.253	0.002	0.001	0.0003	0.0070	0.0071
[0.45, 0.65]	[0.03, 0.04]	0.239	0.002	0.001	0.0025	0.0059	0.0065
[0.45, 0.65]	[0.04, 0.06]	0.225	0.002	0.001	0.0026	0.0054	0.0061
[0.45, 0.65]	[0.06, 0.10]	0.211	0.002	0.001	0.0020	0.0064	0.0068
[0.45, 0.65]	[0.10, 0.15]	0.197	0.003	0.002	0.0003	0.0058	0.0061
[0.45, 0.65]	[0.15, 0.20]	0.186	0.005	0.003	0.0028	0.0088	0.0098
[0.45, 0.65]	[0.20, 0.30]	0.179	0.007	0.005	0.0006	0.0095	0.0108
[0.45, 0.65]	[0.30, 0.40]	0.168	0.021	0.015	0.0201	0.0098	0.0267
[0.45, 0.65]	[0.40, 0.70]	0.241	0.078	0.055	0.0510	0.0688	0.1017
[0.65, 0.85]	[0.004, 0.006]	0.000	0.000	0.000	0.0000	0.0000	0.0000
[0.65, 0.85]	[0.006, 0.01]	0.103	0.005	0.003	0.0004	0.0065	0.0073
[0.65, 0.85]	[0.01, 0.02]	0.119	0.001	0.001	0.0029	0.0044	0.0053
[0.65, 0.85]	[0.02, 0.03]	0.107	0.001	0.001	0.0016	0.0029	0.0034
[0.65, 0.85]	[0.03, 0.04]	0.089	0.001	0.001	0.0000	0.0042	0.0043
[0.65, 0.85]	[0.04, 0.06]	0.079	0.001	0.001	0.0003	0.0040	0.0041
[0.65, 0.85]	[0.06, 0.10]	0.068	0.001	0.001	0.0014	0.0036	0.0039
[0.65, 0.85]	[0.10, 0.15]	0.057	0.002	0.001	0.0019	0.0057	0.0061
[0.65, 0.85]	[0.15, 0.20]	0.054	0.003	0.002	0.0002	0.0039	0.0044
[0.65, 0.85]	[0.20, 0.30]	0.047	0.004	0.003	0.0009	0.0080	0.0084
[0.65, 0.85]	[0.30, 0.40]	0.027	0.008	0.006	0.0024	0.0042	0.0076
[0.65, 0.85]	[0.40, 0.70]	0.101	0.045	0.032	0.1193	0.0000	0.1234

Table C.2: Negative pion multiplicities in bins of x and z [39]

z bin	x bin	M^{K^+}	σ_{stat}	σ_{sys}^{COMP}	σ_{sys}^{MC}	σ_{sys}^{RICH}	σ_{sys}^{tot}
$[0.20, 0.30]$	$[0.004, 0.006]$	0.305	0.005	0.002	0.0042	0.0764	0.0766
$[0.20, 0.30]$	$[0.006, 0.01]$	0.334	0.003	0.001	0.0065	0.0156	0.0169
$[0.20, 0.30]$	$[0.01, 0.02]$	0.359	0.002	0.001	0.0010	0.0018	0.0024
$[0.20, 0.30]$	$[0.02, 0.03]$	0.362	0.004	0.002	0.0047	0.0006	0.0051
$[0.20, 0.30]$	$[0.03, 0.04]$	0.362	0.005	0.002	0.0016	0.0012	0.0031
$[0.20, 0.30]$	$[0.04, 0.06]$	0.392	0.005	0.002	0.0077	0.0009	0.0081
$[0.20, 0.30]$	$[0.06, 0.10]$	0.411	0.006	0.003	0.0109	0.0109	0.0157
$[0.20, 0.30]$	$[0.10, 0.15]$	0.441	0.011	0.005	0.0110	0.0159	0.0200
$[0.20, 0.30]$	$[0.15, 0.20]$	0.436	0.020	0.009	0.0021	0.0157	0.0183
$[0.20, 0.30]$	$[0.20, 0.30]$	0.443	0.028	0.013	0.0175	0.0030	0.0218
$[0.20, 0.30]$	$[0.30, 0.40]$	0.533	0.088	0.039	0.0485	0.0193	0.0654
$[0.20, 0.30]$	$[0.40, 0.70]$	0.274	0.146	0.066	0.1742	0.1201	0.2215
$[0.30, 0.45]$	$[0.004, 0.006]$	0.157	0.004	0.002	0.0086	0.0703	0.0709
$[0.30, 0.45]$	$[0.006, 0.01]$	0.170	0.002	0.001	0.0045	0.0314	0.0317
$[0.30, 0.45]$	$[0.01, 0.02]$	0.193	0.001	0.001	0.0006	0.0100	0.0100
$[0.30, 0.45]$	$[0.02, 0.03]$	0.208	0.002	0.001	0.0017	0.0023	0.0030
$[0.30, 0.45]$	$[0.03, 0.04]$	0.215	0.002	0.001	0.0047	0.0004	0.0049
$[0.30, 0.45]$	$[0.04, 0.06]$	0.223	0.002	0.001	0.0032	0.0029	0.0044
$[0.30, 0.45]$	$[0.06, 0.10]$	0.233	0.003	0.001	0.0051	0.0049	0.0071
$[0.30, 0.45]$	$[0.10, 0.15]$	0.241	0.004	0.002	0.0031	0.0064	0.0074
$[0.30, 0.45]$	$[0.15, 0.20]$	0.263	0.008	0.004	0.0031	0.0052	0.0070
$[0.30, 0.45]$	$[0.20, 0.30]$	0.244	0.011	0.005	0.0028	0.0038	0.0068
$[0.30, 0.45]$	$[0.30, 0.40]$	0.337	0.040	0.018	0.0197	0.0036	0.0269
$[0.30, 0.45]$	$[0.40, 0.70]$	0.367	0.162	0.073	0.0540	0.1222	0.1522
$[0.45, 0.65]$	$[0.004, 0.006]$	0.065	0.010	0.004	0.0013	0.0488	0.0490
$[0.45, 0.65]$	$[0.006, 0.01]$	0.072	0.002	0.001	0.0051	0.0251	0.0256
$[0.45, 0.65]$	$[0.01, 0.02]$	0.082	0.001	0.000	0.0024	0.0067	0.0071
$[0.45, 0.65]$	$[0.02, 0.03]$	0.093	0.001	0.000	0.0003	0.0040	0.0040
$[0.45, 0.65]$	$[0.03, 0.04]$	0.092	0.001	0.001	0.0015	0.0044	0.0047
$[0.45, 0.65]$	$[0.04, 0.06]$	0.092	0.001	0.001	0.0011	0.0058	0.0059
$[0.45, 0.65]$	$[0.06, 0.10]$	0.092	0.001	0.001	0.0013	0.0060	0.0062
$[0.45, 0.65]$	$[0.10, 0.15]$	0.103	0.002	0.001	0.0015	0.0081	0.0083
$[0.45, 0.65]$	$[0.15, 0.20]$	0.100	0.004	0.002	0.0005	0.0096	0.0098
$[0.45, 0.65]$	$[0.20, 0.30]$	0.098	0.005	0.002	0.0003	0.0065	0.0069
$[0.45, 0.65]$	$[0.30, 0.40]$	0.130	0.020	0.009	0.0212	0.0511	0.0561
$[0.45, 0.65]$	$[0.40, 0.70]$	0.215	0.137	0.062	0.0529	0.0000	0.0812
$[0.65, 0.85]$	$[0.004, 0.006]$	0.000	0.000	0.000	0.0000	0.0000	0.0000
$[0.65, 0.85]$	$[0.006, 0.01]$	0.024	0.002	0.001	0.0033	0.0145	0.0149
$[0.65, 0.85]$	$[0.01, 0.02]$	0.028	0.001	0.000	0.0003	0.0063	0.0063
$[0.65, 0.85]$	$[0.02, 0.03]$	0.030	0.001	0.000	0.0005	0.0035	0.0036
$[0.65, 0.85]$	$[0.03, 0.04]$	0.030	0.001	0.000	0.0001	0.0035	0.0036
$[0.65, 0.85]$	$[0.04, 0.06]$	0.030	0.001	0.000	0.0000	0.0038	0.0038
$[0.65, 0.85]$	$[0.06, 0.10]$	0.031	0.001	0.000	0.0002	0.0061	0.0061
$[0.65, 0.85]$	$[0.10, 0.15]$	0.032	0.001	0.000	0.0000	0.0076	0.0076
$[0.65, 0.85]$	$[0.15, 0.20]$	0.036	0.002	0.001	0.0008	0.0078	0.0079
$[0.65, 0.85]$	$[0.20, 0.30]$	0.033	0.003	0.001	0.0037	0.0120	0.0126
$[0.65, 0.85]$	$[0.30, 0.40]$	0.030	0.008	0.004	0.0002	0.0122	0.0128
$[0.65, 0.85]$	$[0.40, 0.70]$	0.013	0.013	0.006	0.0086	0.0126	0.0164

Table C.3: Positive kaon multiplicities in bins of x and z [39]

z bin	x bin	M^{K^-}	σ_{stat}	σ_{sys}^{COMP}	σ_{sys}^{MC}	σ_{sys}^{RICH}	σ_{sys}^{tot}
[0.20, 0.30]	[0.004, 0.006]	0.266	0.005	0.003	0.0047	0.0011	0.0057
[0.20, 0.30]	[0.006, 0.01]	0.284	0.003	0.002	0.0047	0.0055	0.0075
[0.20, 0.30]	[0.01, 0.02]	0.283	0.002	0.001	0.0038	0.0022	0.0046
[0.20, 0.30]	[0.02, 0.03]	0.280	0.003	0.002	0.0036	0.0018	0.0045
[0.20, 0.30]	[0.03, 0.04]	0.278	0.004	0.003	0.0022	0.0022	0.0041
[0.20, 0.30]	[0.04, 0.06]	0.278	0.004	0.003	0.0005	0.0001	0.0027
[0.20, 0.30]	[0.06, 0.10]	0.266	0.005	0.003	0.0002	0.0021	0.0036
[0.20, 0.30]	[0.10, 0.15]	0.247	0.008	0.005	0.0063	0.0002	0.0079
[0.20, 0.30]	[0.15, 0.20]	0.230	0.014	0.008	0.0134	0.0010	0.0158
[0.20, 0.30]	[0.20, 0.30]	0.233	0.020	0.012	0.0001	0.0046	0.0127
[0.20, 0.30]	[0.30, 0.40]	0.255	0.055	0.033	0.0266	0.0061	0.0427
[0.20, 0.30]	[0.40, 0.70]	0.212	0.167	0.100	0.0511	0.1061	0.1548
[0.30, 0.45]	[0.004, 0.006]	0.124	0.003	0.002	0.0091	0.0572	0.0579
[0.30, 0.45]	[0.006, 0.01]	0.139	0.002	0.001	0.0036	0.0181	0.0185
[0.30, 0.45]	[0.01, 0.02]	0.143	0.001	0.001	0.0020	0.0045	0.0050
[0.30, 0.45]	[0.02, 0.03]	0.140	0.001	0.001	0.0000	0.0009	0.0012
[0.30, 0.45]	[0.03, 0.04]	0.139	0.002	0.001	0.0019	0.0011	0.0025
[0.30, 0.45]	[0.04, 0.06]	0.135	0.002	0.001	0.0007	0.0008	0.0015
[0.30, 0.45]	[0.06, 0.10]	0.132	0.002	0.001	0.0019	0.0031	0.0038
[0.30, 0.45]	[0.10, 0.15]	0.118	0.003	0.002	0.0002	0.0030	0.0035
[0.30, 0.45]	[0.15, 0.20]	0.108	0.005	0.003	0.0010	0.0005	0.0032
[0.30, 0.45]	[0.20, 0.30]	0.101	0.008	0.005	0.0109	0.0025	0.0121
[0.30, 0.45]	[0.30, 0.40]	0.132	0.029	0.018	0.0213	0.0018	0.0277
[0.30, 0.45]	[0.40, 0.70]	0.091	0.069	0.042	0.0118	0.0000	0.0433
[0.45, 0.65]	[0.004, 0.006]	0.060	0.009	0.005	0.0072	0.0462	0.0471
[0.45, 0.65]	[0.006, 0.01]	0.053	0.001	0.001	0.0024	0.0211	0.0212
[0.45, 0.65]	[0.01, 0.02]	0.057	0.001	0.000	0.0002	0.0046	0.0046
[0.45, 0.65]	[0.02, 0.03]	0.055	0.001	0.000	0.0001	0.0013	0.0014
[0.45, 0.65]	[0.03, 0.04]	0.051	0.001	0.001	0.0001	0.0013	0.0014
[0.45, 0.65]	[0.04, 0.06]	0.046	0.001	0.000	0.0004	0.0008	0.0010
[0.45, 0.65]	[0.06, 0.10]	0.042	0.001	0.001	0.0005	0.0001	0.0007
[0.45, 0.65]	[0.10, 0.15]	0.033	0.001	0.001	0.0005	0.0006	0.0010
[0.45, 0.65]	[0.15, 0.20]	0.029	0.002	0.001	0.0017	0.0005	0.0021
[0.45, 0.65]	[0.20, 0.30]	0.025	0.003	0.002	0.0000	0.0002	0.0015
[0.45, 0.65]	[0.30, 0.40]	0.017	0.006	0.004	0.0032	0.0021	0.0053
[0.45, 0.65]	[0.40, 0.70]	0.000	0.000	0.000	0.0000	0.0000	0.0000
[0.65, 0.85]	[0.004, 0.006]	0.000	0.000	0.000	0.0000	0.0000	0.0000
[0.65, 0.85]	[0.006, 0.01]	0.016	0.002	0.001	0.0003	0.0146	0.0146
[0.65, 0.85]	[0.01, 0.02]	0.016	0.000	0.000	0.0000	0.0050	0.0050
[0.65, 0.85]	[0.02, 0.03]	0.014	0.000	0.000	0.0001	0.0019	0.0019
[0.65, 0.85]	[0.03, 0.04]	0.014	0.001	0.000	0.0002	0.0013	0.0013
[0.65, 0.85]	[0.04, 0.06]	0.013	0.000	0.000	0.0001	0.0012	0.0012
[0.65, 0.85]	[0.06, 0.10]	0.011	0.000	0.000	0.0002	0.0004	0.0005
[0.65, 0.85]	[0.10, 0.15]	0.009	0.001	0.000	0.0001	0.0001	0.0004
[0.65, 0.85]	[0.15, 0.20]	0.006	0.001	0.001	0.0001	0.0002	0.0006
[0.65, 0.85]	[0.20, 0.30]	0.004	0.001	0.001	0.0001	0.0002	0.0006
[0.65, 0.85]	[0.30, 0.40]	0.010	0.005	0.003	0.0027	0.0020	0.0046
[0.65, 0.85]	[0.40, 0.70]	0.000	0.000	0.000	0.0000	0.0000	0.0000

Table C.4: Positive kaon multiplicities in bins of x and z [39]

Appendix D

Bibliography

[1] P. Abbon *et al.*, "The COMPASS Experiment at CERN," *Nucl. Instrum. Meth.*, vol. A577, pp. 455–518, 2007.

[2] E. Leader, "The longitudinal spin structure of the nucleon," pp. 263–286, 2007.

[3] J. Levelt, "Deep inelastic semiinclusive processes," 1993.

[4] C. Amsler *et al.*, "Review of Particle Physics," *Phys.Lett.*, vol. B667, pp. 1–1340, 2008.

[5] J. Bjorken, "Asymptotic Sum Rules at Infinite Momentum," *Phys.Rev.*, vol. 179, pp. 1547–1553, 1969.

[6] J. Callan, Curtis G. and D. J. Gross, "High-energy electroproduction and the constitution of the electric current," *Phys.Rev.Lett.*, vol. 22, pp. 156–159, 1969.

[7] J. Bjorken and E. A. Paschos, "Inelastic Electron Proton and gamma Proton Scattering, and the Structure of the Nucleon," *Phys.Rev.*, vol. 185, pp. 1975–1982, 1969.

[8] J. Pretz, *Messung der polarisierten Quarkverteilungen in semi-inklusiver Myon-Nukleon-Streuung.* Dissertation, Johannes-Gutenberg–Universität Mainz, 1997.

[9] J. Binnewies, B. A. Kniehl, and G. Kramer, "Pion and kaon production in e+ e- and e p collisions at next-to-leading order," *Phys.Rev.*, vol. D52, pp. 4947–4960, 1995.

[10] M. Arneodo *et al.*, "Measurements of the u Valence Quark Distribution Function in the Proton and u Quark Fragmentation Functions," *Nucl. Phys.*, vol. B321, p. 541, 1989.

[11] B. Andersson, G. Gustafson, G. Ingelman, and T. Sjostrand, "Parton Fragmentation and String Dynamics," *Phys.Rept.*, vol. 97, pp. 31–145, 1983.

[12] R. Field and R. Feynman, "A Parametrization of the Properties of Quark Jets," *Nucl.Phys.*, vol. B136, p. 1, 1978.

[13] T. Sjostrand, "Pythia 5.7 and jetset 7.4 physics and manual," 1994.

[14] A. Kotzinian, "New quark distributions and semiinclusive electroproduction on the polarized nucleons," *Nucl.Phys.*, vol. B441, pp. 234–248, 1995.

[15] Halzen and A. Martin, *Quarks and Leptons, an introductory course in Modern Particle Physics.* New York: Wiley, 1984.

[16] C. Adloff *et al.*, "Deep inelastic inclusive e p scattering at low x and a determination of alpha(s)," *Eur.Phys.J.*, vol. C21, pp. 33–61, 2001.

[17] G. Altarelli and G. Parisi, "Asymptotic Freedom in Parton Language," *Nucl.Phys.*, vol. B126, p. 298, 1977.

[18] V. Gribov and L. Lipatov, "e+ e- pair annihilation and deep inelastic e p scattering in perturbation theory," *Sov.J.Nucl.Phys.*, vol. 15, pp. 675–684, 1972.

[19] Y. L. Dokshitzer, "Calculation of the Structure Functions for Deep Inelastic Scattering and e+ e- Annihilation by Perturbation Theory in Quantum Chromodynamics.," *Sov.Phys.JETP*, vol. 46, pp. 641–653, 1977.

[20] T. Uematsu, "Q**2 Dependence of Quark and Gluon Fragmentation Functions in a Parton Picture Based on QCD," *Phys.Lett.*, vol. B79, p. 97, 1978.

[21] G. Altarelli, R. K. Ellis, G. Martinelli, and S.-Y. Pi, "Processes Involving Fragmentation Functions Beyond the Leading Order in QCD," *Nucl.Phys.*, vol. B160, p. 301, 1979.

[22] R. Baier and K. Fey, "Finite Corrections to Quark Fragmentation Functions in Pertubative QCD," *Z.Phys.*, vol. C2, pp. 339–349, 1979.

[23] M. Alekseev *et al.*, "Flavour Separation of Helicity Distributions from Deep Inelastic Muon-Deuteron Scattering," *Phys. Lett.*, vol. B680, pp. 217–224, 2009.

[24] A. Airapetian *et al.*, "Quark helicity distributions in the nucleon for up, down, and strange quarks from semi–inclusive deep–inelastic scattering," *Phys. Rev.*, vol. D71, p. 012003, 2005.

[25] A. D. Martin, W. J. Stirling, and R. S. Thorne, "MRST partons generated in a fixed-flavour scheme," *Phys. Lett.*, vol. B636, pp. 259–264, 2006.

[26] D. de Florian, R. Sassot, and M. Stratmann, "Global Analysis of Fragmentation Functions for Pions and Kaons and Their Uncertainties," *Phys. Rev.*, vol. D75, p. 114010, 2007.

[27] D. de Florian, G. A. Navarro, and R. Sassot, "Sea quark and gluon polarization in the nucleon at NLO accuracy," *Phys. Rev.*, vol. D71, p. 094018, 2005.

[28] S. Kretzer, "Fragmentation functions from flavour-inclusive and flavour-tagged e+ e- annihilations," *Phys. Rev.*, vol. D62, p. 054001, 2000.

[29] M. Alekseev *et al.*, "The Polarised Valence Quark Distribution from semi- inclusive DIS," *Phys. Lett.*, vol. B660, pp. 458–465, 2008.

[30] P. Jasinski, 2012. Private communications (2010).

[31] C. Lefevre, "The cern accelerator complex / complexe des acclrateurs du cern, retrieved 2012-06-18 (http://public.web.cern.ch/public/en/research/accelcomplex-en.html)."

[32] J. Pretz, *The Gluon Polarization in the Nucleon.* PhD thesis, Rheinische Friedrich-Wilhelms-Universität Bonn, 2007. Habilitation thesis.

[33] C. Bernet, A. Bravar, J. Hannappel, D. von Harrach, R. Hermann, *et al.*, "The COMPASS trigger system for muon scattering," *Nucl.Instrum.Meth.*, vol. A550, pp. 217–240, 2005.

[34] A. A., 1961. The principles of nuclear magnetism, Clarendon Press.

[35] O. Naehle, "Erprobung von szintillierenden Fasern und iherer Ankopplung an Lichtleiter und Photomultiplier fuer das COMPASS-Experiment," diplomarbeit, Rheinische Friedrich-Wilhelms-Universität Bonn, 1998.

[36] S. Horikawa, I. Daito, N. Doshita, A. Gorin, T. Hasegawa, *et al.*, "A scintillating fiber tracker with high time resolution for high-rate experiments," *IEEE Trans.Nucl.Sci.*, vol. 49, pp. 950–956, 2002.

[37] COMPASS, "Compass rich-1, figures, retrieved 2012-01-12."

[38] E. Albrecht, G. Baum, R. Birsa, M. Bosteels, F. Bradamante, *et al.*, "COMPASS RICH-1," *Nucl.Instrum.Meth.*, vol. A478, pp. 340–343, 2002.

[39] N. Makke, *Mesure de la polarisation des quark tranges dans le nuclon et des fonctions de fragmentation des quarks en hadrons.* Dissertation, Université Paris-Sud XI, 2011.

[40] M. Leberig, *Das COMPASS-Triggersystem zur Messung des Gluonbeitrags Delta G zum Protonspin.* Dissertation, Johannes-Gutenberg–Universität Mainz, 2002.

[41] D. E. Groom, F. James, and R. Cousins, "Probability: in Review of Particle Physics (RPP 2000)," *Eur.Phys.J.*, vol. C15, pp. 191–194, 2000.

[42] W. Lohmann, R. Kopp, and R. Voss, "Energy Loss of Muons in the Energy Range 1 GeV to 10000 GeV," 1985.

[43] R. Brun, "Root Users Guide 5.22, http://root.cern.ch/," 2009.

[44] M. Alekseev *et al.*, "Quark helicity distributions from longitudinal spin asymmetries in muon-proton and muon-deuteron scattering," *Phys.Lett.*, vol. B693, pp. 227–235, 2010.

[45] B. Adeva *et al.*, "Polarized quark distributions in the nucleon from semiinclusive spin asymmetries," *Phys.Lett.*, vol. B420, pp. 180–190, 1998.

[46] M. G. Alekseev *et al.*, "The Spin-dependent Structure Function of the Proton and a Test of the Bjorken Sum Rule," *Phys.Lett.*, vol. B690, pp. 466–472, 2010.

[47] R. Windmolders, "Quark helicity distributions from longitudinal spin asymmetries in muon-proton and muon-deuteron scattering," *J.Phys.Conf.Ser.*, vol. 295, p. 012069, 2011.

[48] D. de Florian, R. Sassot, M. Stratmann, and W. Vogelsang, "Extraction of Spin-Dependent Parton Densities and Their Uncertainties," *Phys.Rev.*, vol. D80, p. 034030, 2009.

[49] A. Airapetian *et al.*, "Precise determination of the spin structure function g(1) of the proton, deuteron and neutron," *Phys.Rev.*, vol. D75, p. 012007, 2007.

[50] E. S. Ageev *et al.*, "Spin Asymmetry A(1)(d) and the Spin-dependent Structure Function g1(d) of the Deuteron at Low Values of x and Q^2," *Phys. Lett.*, vol. B647, pp. 330–340, 2007.

[51] S. D. Bass and A. W. Thomas, "The Nucleon's octet axial-charge g(A)**(8) with chiral corrections," *Phys.Lett.*, vol. B684, pp. 216–220, 2010.

[52] "The Durham HepData Project, retrieved 2012-01-15."

[53] T. Sjostrand, S. Mrenna, and P. Z. Skands, "PYTHIA 6.4 Physics and Manual," *JHEP*, vol. 0605, p. 026, 2006.

[54] J. Pumplin, D. Stump, J. Huston, H. Lai, P. M. Nadolsky, *et al.*, "New generation of parton distributions with uncertainties from global QCD analysis," *JHEP*, vol. 0207, p. 012, 2002.

[55] H. Lai, J. Botts, J. Huston, J. Morfin, J. Owens, *et al.*, "Global QCD analysis and the CTEQ parton distributions," *Phys.Rev.*, vol. D51, pp. 4763–4782, 1995.

[56] P. Amaudruz *et al.*, "Proton and deuteron f2 structure functions in deep inelastic muon scattering," *Phys.Lett.*, vol. B295, pp. 159–168, 1992.

[57] P. Quintas, W. Leung, S. Mishra, F. Sciulli, C. Arroyo, *et al.*, "A Measurement of Lambda (MS) from muon-neutrino - Fe nonsinglet structure functions at the Fermilab tevatron," *Phys.Rev.Lett.*, vol. 71, pp. 1307–1310, 1993.

[58] A. Benvenuti *et al.*, "A High Statistics Measurement of the Deuteron Structure Functions $F_2(x, Q^2)$ and R from Deep Inelastic Muon Scattering at High Q^2," *Phys.Lett.*, vol. B237, p. 592, 1990.

[59] G. Moreno, C. Brown, W. Cooper, D. Finley, Y. Hsiung, *et al.*, "Dimuon production in proton - copper collisions at $\sqrt{s} = 38.8$-GeV," *Phys.Rev.*, vol. D43, pp. 2815–2836, 1991.

[60] A. Baldit *et al.*, "Study of the isospin symmetry breaking the in the light quark sea of the nucleon from the Drell-Yan process," *Phys.Lett.*, vol. B332, pp. 244–250, 1994.

[61] A. Martin, W. Stirling, R. Thorne, and G. Watt, "Parton distributions for the LHC," *Eur.Phys.J.*, vol. C63, pp. 189–285, 2009.

[62] M. Goncharov *et al.*, "Precise measurement of dimuon production cross-sections in muon neutrino Fe and muon anti-neutrino Fe deep inelastic scattering at the Tevatron," *Phys.Rev.*, vol. D64, p. 112006, 2001.

[63] R. Windmolders, "Can we extract fragmentation functions from compass released charged kaon multiplicities?," COMPASS Collaboration Meeting, 2012.

List of Figures

List of Tables

Acknowledgement